

# Remote plasma assisted fabrication of functional organic and hybrid thin films and supported nanostructures



María Alcaire Martín

Supervisors: Ángel Barranco Quero & Ana Isabel Borrás Martos

Instituto de Ciencia de Materiales de Sevilla (US-CSIC)

Universidad de Sevilla

A thesis submitted for the degree of PhD

2015



# INDEX



## **1 INTRODUCTION**

- 1.1 Introduction to plasma 4**
- 1.2 Introduction to Plasma Enhance Chemical Vapour Deposition (PECVD) and Plasma Polymerization 8**
- 1.3 Remote Plasma Assisted Vacuum Deposition (RPAVD) 13**
- 1.4 Fundamentals of 1D organic nanowires 33**
- 1.5 Introduction to the growth and optical properties of ZnO 40**
- 1.6 Objectives 44**
- REFERENCES 47**

## **2 RESUMEN EN ESPAÑOL**

- 2.1 Introduction 58**
- 2.2 Láminas delgadas orgánicas conformales para aplicaciones en electrónica molecular 60**
  - 2.2.1 Experimental 62
  - 2.2.2 Resultados y discusión 62
- 2.3 Mojado y retardo en la congelación de recubrimientos de adamantano: de la estructura en lámina delgada a redes 3D 62**
  - 2.3.1 Experimental 62
  - 2.3.2 Resultados y discusión 62
- 2.4 Emisión multicolor y láser en nanocomposites de DCM y adamantano 62**
  - 2.4.1 Experimental 62
  - 2.4.2 Resultados y discusión 62
- 2.5 Tratamientos con plasma débil de nanohilos orgánicos: una vía para la fabricación de heteroestructuras orgánicas 1D y la síntesis de patrones de diseño de nanoestructuras inorgánicas 1D 62**
  - 2.5.1 Experimental 62
  - 2.5.2 Caracterización de heteroestructuras orgánicas 1D 62
  - 2.5.3 Resultados y discusión 62
- 2.6 Láminas delgadas porosas y estructuras 1D de óxido de cinc mediante procesado por plasma remoto de ftalocianina de cinc 62**
  - 2.6.1 Experimental 62
  - 2.6.2 Resultados 62
- REFERENCIAS 62**

---

### **3 CONFORMAL DIELECTRIC ORGANIC THIN FILMS FOR MOLECULAR ELECTRONICS**

<b>3.1</b>	<b>Introduction</b>	<b>112</b>
<b>3.2</b>	<b>Experimental Setup</b>	<b>113</b>
<b>3.3</b>	<b>Results and discussion</b>	<b>114</b>
<b>3.4</b>	<b>Conclusions</b>	<b>123</b>
	<b>REFERENCES</b>	<b>125</b>
	<b>Supporting Information</b>	<b>128</b>

### **4 WETTING AND ANTI-FREEZING PROPERTIES OF ADAMANTANE COATINGS: FROM THIN FILMS TO 3D NETWORKS**

<b>4.1</b>	<b>Introduction</b>	<b>130</b>
<b>4.2</b>	<b>Experimental Set Up</b>	<b>137</b>
<b>4.3</b>	<b>Results and discussion</b>	<b>139</b>
4.3.1	Temperature effects on wetting	139
4.3.2	Water condensation and freezing on smooth flat adamantane RPAVD	142
4.3.3	Water condensation and freezing on adamantane RPAVD grown on rough surfaces..	153
4.3.4	Water condensation and freezing on adamantane RPAVD grown on highly hydrophobic 1D nanostructures	158
4.3.5	Water condensation and freezing on adamantane RPAVD grown on 3D nanonetworks	163
4.3.6	Condensation and freezing on adamantane RPAVD on metal substrates effects....	170
<b>4.4</b>	<b>Conclusions</b>	<b>172</b>
	<b>REFERENCES</b>	<b>174</b>

### **5 MULTICOLORED EMISSION AND LASING IN DCM-ADAMANTANE PLASMA NANOCOMPOSITES**

<b>5.1</b>	<b>Introduction</b>	<b>180</b>
<b>5.2</b>	<b>Experimental Setup</b>	<b>182</b>
5.2.1	Materials	182
5.2.2	Plasma assisted vacuum deposition procedure	183
5.2.3	Thin film characterization	185
<b>5.3</b>	<b>Results and discussion</b>	<b>189</b>
5.3.1	Thin film composition and microstructure	189
5.3.2	Optical properties	192
5.3.3	Steady state and time resolved luminescence	195
5.3.4	ASE experiments	200
5.3.5	DFB laser experiments	202

**5.4 Conclusions 206**

**REFERENCES 208**

**6 SOFT PLASMA PROCESSING OF ORGANIC NANOWIRES: A ROUTE FOR THE FABRICATION OF 1D ORGANIC HETEROSTRUCTURES AND THE TEMPLATE SYNTHESIS OF INORGANIC 1D NANOSTRUCTURES**

**6.1 Introduction 212**

**6.2 Experimental Setup 213**

6.2.1 Organic Nanowires formation by PVD 214

6.2.2 Soft Plasma treatments 215

6.2.3 Secondary Organic Nanowires formation by PVD 215

6.2.4 Characterization of 1D organic heterostructures 215

**6.3 Results and discussion 216**

6.3.1 Heterostructured hierarchical NWs formed by oxygen plasma 216

6.3.2 Metal-Organic Hybrid NWs formed by SOFT plasma processing 222

6.3.3 From Hybrid to metal and oxide NWs 227

**6.4 Conclusions 229**

**REFERENCES 231**

**7 HIGHLY POROUS ZNO THIN FILMS AND 1D NANOSTRUCTURES BY REMOTE PLASMA PROCESSING OF ZN-PHTHALOCYANINE**

**7.1 Introduction 236**

**7.2 Experimental Setup 237**

7.2.1 Deposition of ZnPc thin films and ONWs 239

7.2.2 Deposition of Au by sputtering 240

7.2.3 Soft etching by ECR-MW oxygen plasma 241

7.2.4 Characterization methods 241

**7.3 Results and discussion 242**

7.3.1 Organic thin films and single crystal nanowires by Physical Vapor Deposition of ZnPc 242

7.3.2 Oxygen plasma etching of ZnPc thin films 245

7.3.3 Oxygen plasma etching of ZnPc thin films 258

**7.4 Conclusions 264**

**REFERENCES 266**

**8 GENERAL CONCLUSIONS 269**

---

**A 1 ADAMANTANE RPAVD: FROM THIN FILMS TO 3D NETWORKS**


<b>A1.1 Introduction</b>	<b>276</b>
<b>A1.2 Experimental Setup</b>	<b>278</b>
<b>A1.3 Results and discussion</b>	<b>281</b>
A1.3.1 Characterization of RPAVD thin films	282
A1.3.2 Adamantane RPAVD in the reactor: effects of pressure, power of MW plasma source and growth rate on	298
A1.3.3 Effect of substrate microstructure on ADAMANTANE RPAVD thin film synthesis	305
<b>A1.4 Conclusions</b>	<b>317</b>
<b>REFERENCES</b>	<b>318</b>

**A2 OXYGEN OPTICAL SENSING WITH NANOSTRUCTURED ZNO THIN FILMS**

<b>A2.1 Introduction</b>	<b>322</b>
<b>A2.2 Experimental Setup</b>	<b>323</b>
<b>A2.3 Results and discussion</b>	<b>325</b>



# 1 Introduction



---


In general, functional materials are categorized as those materials which possess particular native properties and functions of their own. Examples of these properties are: ferroelectricity, piezoelectricity, magnetism, temperature variations, pressure variations and optical functions. There exists an immense range of functional materials. For instance, optical materials, including lasers, Raman scattering, fluorescence and phosphorescence, are functional materials. Moreover, electrical, magnetics and dielectrics materials are also examples of functional materials, such as semiconducting devices and superconductors, piezoelectrics, ferroelectrics, optical fibres and liquid crystals.<sup>1-3</sup> On the other hand, functional materials include ceramics, metals, polymers and organic molecules. In recent years, one of the main goals of materials science is the fabrication of new functional materials because of their applications in electronics, informatics and telecommunications. Its continuous development is based on environmental aspects (energy-efficiency, life-cycle issues, recycling or renewable solutions) and cost reduction aspects (energy saving factors in production).

One of the key requirements to achieve satisfying properties of the materials is controlling the structural and compositional evolution. The work included in this thesis develops around searching new routes to prepare materials and understanding the relationship between their structures and properties.

Currently, organic and inorganic starting precursors and wide range of techniques are used for the fabrication of functional materials. The present thesis is focused on the synthesis of functional materials in the form of thin films by a technique that relies on remote microwaves plasmas in combination with organic precursors and their subsequent processing for targeted applications. This deposition technique is termed Remote Plasma Assisted Vacuum Deposition (RPAVD).<sup>4-11</sup> The work presented here tries to explore about the possibilities of

the technique. For this purpose, the two followed guidelines are the characterization of the films and to achieve the control of their properties.

This thesis is subdivided into eight chapters. At first, Chapter 1 includes the Introduction to the whole work developed throughout the thesis. Chapter 2 gathers an overview of the thesis in Spanish language. Chapters 3-4 (“Conformal dielectric organic thin films for molecular electronics” and “Wetting and anti-freezing properties of adamantane coatings: from thin films to 3D networks”) study the processability and applications of organic thin films as coatings through its functionalities. These films are fabricated from a precursor of adamantane ( $C_{10}H_{16}$ ) by RPAVD technique. Separated Chapters 3-4 provide the analysis of two properties of adamantane RPAVD films: dielectric and anti-freezing properties. Later, Annex 1 (“Adamantane RPAVD: from thin films to 3D networks”) shows a complete characterization of these adamantane films. After that, this section establishes the control of properties of this type of films, as well as the development of the synthesis of this precursor as supported nanostructures. In addition, it also illustrated that some properties of the films founded in this work can be extended to whole RPAVD materials. Chapter 5, “Multicolored emission and lasing in DCM-Adamantane plasma nanocomposites” introduces new RPAVD thin films using the combination of a dye laser (4-(Dicyanomethylene)-2-methyl-6-(4-dimethylaminostyryl)-4H-pyran,  $C_{19}H_{17}N_3O$ ) and adamantane as precursors. These films exhibit different functionalities that are related to optical properties. In the first instance, this Chapter studies the chemical characterization of the films grown by the mixture of the two precursors. Later, its optical properties are adjusted for a final processing. Finally, it is presented the achievements in the integration of one type of these films in a laser device. Chapter 6 (“Soft Plasma processing of Organic Nanowires”) studies a general procedure for the fabrication of hierarchical and hybrid 1D nanostructures from metalloporphyrin,



---

metallophthalocyanine and perylene diimide by plasma processing. The method also provides a template route for the synthesis of supported metal and metal oxide nanostructures by oxygen plasma treatments. In this way, Chapter 7 (“Highly porous ZnO thin films and 1D nanostructures by remote plasma processing of Zn-phthalocyanine”) studies the plasma-assisted oxidation of ZnPc in the form of thin film or nanowires to nanostructured ZnO materials. We analyze the characterization of both thin film and supported nanostructures of these hybrid materials. On the other hand, we also evaluate their applications in connection with Annex 2 where we present ZnO thin films from inorganic precursor ( $\text{ZnEt}_2$ ) discussed as photonic sensor of oxygen. It is worth to notice that the end of Annex 1 introduces some advances in the synthesis method of functional RPAVD materials. We have developed a new RPAVD structure named nanofabric. Nanofabric is the result of a combination of two accomplishments performed in the present work: the synthesis of hierarchical nanostructures described in Chapter 6, and the process of adamantane by RPAVD detailed in Chapters 3-4 and this Annex.

## 1.1 Introduction to plasma

The use of plasma in the manufacturing techniques of functional materials is an essential item in the motivation of this thesis. Therefore, we describe briefly the following general issues in this section:

- a) When first was plasma introduced
- b) What is plasma and what processes are involved in it
- c) How and where is it generated
- d) What are the plasma parameters
- e) Why is plasma used for materials fabrication

Plasma is the most abundant known matter in the universe (99%) as a part of the sun, stars and nebulae. However, on the Earth, lightning and aurora

borealis are the only the most significant natural presence of plasmas.<sup>12</sup> In 1928, Irving Langmuir introduced “plasma” as a region containing balanced charges of ions and electrons of strongly ionized gases at low pressures.<sup>13</sup> A more rigorous designation is “a quasi- neutral gas of charged and neutral particles characterized by a collective behaviour”.<sup>14</sup> In a classical neutral gas, the motion of the molecules is controlled by the collision between them and the walls of the container following a random Brownian motion. A plasma is a ionized gas electrically neutral (with same electron and ion density) that contains free electric charges whose kinetic is given by collective effects. In this connection, a plasma involves processes of charges recombination. Nevertheless, plasma implicates ionization processes that cause free electrons accelerated by external electro-magnetic fields gaining energy. Thus, plasma is a good electrical conductor and internally interactive, and responds to electromagnetic forces, in which its elements affect each other even large separations.<sup>12</sup> Plasmas also emit light whose analysis provides information about the species.

Plasma can be generated and sustained by electrical discharges in low pressure gases.<sup>14</sup> There are diverse energy sources to excite plasma, such as direct current (DC), radiofrequency (RF) or microwave (MW)<sup>14, 15</sup>. The energy of the electric field is accumulated by the electrons between collisions and after is transferred to the heavy particles.<sup>12</sup> The electron collides establishing an electric current while the external energy source is maintained. When it is stopped, the electron and ions will be recombined and plasma will be extinguished.

Plasma is characterized by different parameters being the more significant mentioned below. The parameter that defines the density of the charged particles is the *degree of ionization* (fraction of the particles in the gaseous phase which are ionized).<sup>14</sup> For plasmas sustained in low-pressures discharges, it is typically  $10^{-6}$  to  $10^{-3}$ . *Electron temperature* is another important

parameter of plasmas. Plasma temperature is determined by the average energies of the neutral and charges particles. Thus, plasma exhibits various temperatures. When collisions of the electrons that have received energy from electric field, collide with heavy particles can equilibrating their temperatures, the system is in local thermodynamic equilibrium, and is called “thermal plasma”. On the contrary, in low pressure plasma like those produced by electric discharges excitation, temperatures of heavy particles are insignificant to promote chemical reactions in comparison with *electron temperature*. The low density and heat capacity of the electrons make the heat transference from electrons to gas and the walls to be very small. *Electron temperature* is consequently the most important temperature to describe the distribution of active species. This type of plasmas are not in any local thermodynamic equilibrium and are named “cold plasmas”<sup>14, 15</sup> or “non-thermal plasma”.<sup>12,15</sup> *Debye length* represents the characteristic dimension of regions in which local concentration of charges can produce in the plasma.<sup>14</sup> And last, *plasma sheath* is the term used for the transition zone between the plasma and its boundaries. The boundaries influence the motion of the charged particles in the sheath.<sup>12</sup>

Plasma can produce increases of efficiency and stimulation of chemical reactions yielding deposition processes that are not feasible in conventional chemistry. This intensification of chemical processes is performed through the high concentrations of active species at temperatures as low as room temperature.<sup>12</sup> Processing techniques and synthesis of materials based on plasma technology cover a wide range of industrial applications in different fields, from fabrication in micro-electronics of coatings and thin films to production of ozone to plasma TVs or functionalization of fabrics and polymers.<sup>14, 16, 17</sup> In this thesis, the plasma discharges will be used to produce the deposition of thin films and for the processing of the surfaces of the thin films or nanostructures after deposition.

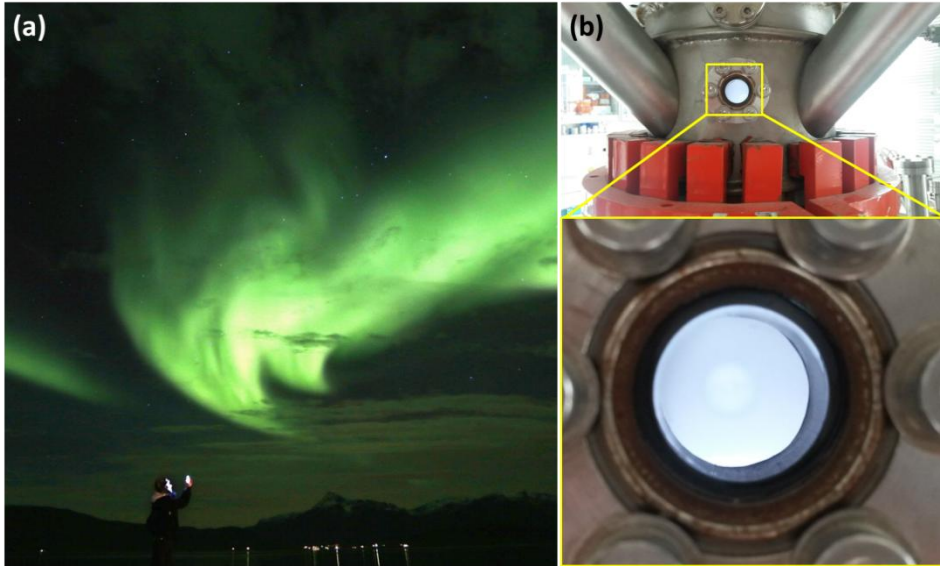


Figure 1.1. Plasma in nature and in the laboratory- (a) Aurora borealis and. Retrieved from [http:// www.huffingtonpost.es /2014/ 10/ 03/ auroras-boreales- noruega\\_n\\_5919052.html](http://www.huffingtonpost.es/2014/10/03/auroras-boreales-noruega_n_5919052.html). (b) O<sub>2</sub> ECR- plasma in a remote plasma assisted vacuum deposition (RPAVD) reactor for the fabrication and treatment of thin films.

### 1.1.1 Microwave (MW) and electron cyclotron (ECR) plasmas

MW plasmas are non-thermal plasmas sustained by power supplies operating at a frequency of 2.45 GHz and about 30 V/cm of electric field strength.<sup>14, 16</sup> Plasma excited by MW introduces some advantages over DC or RF discharges. First, the reactors do not require electrodes to apply the electric field, thus dielectric materials can be deposited avoiding contamination due to electrodes etching processes. Second, the wavelength of the MW electric field is in the same order than the reactor dimensions ( $\lambda = 12.24$  cm) being much smaller than in the case of RF field.<sup>14, 16</sup>

ECR plasma refers to plasma discharge excited and sustained by the combination of an electric and a magnetic field, typically microwave plasmas. By applying a magnetic field to a plasma discharge, free electrons perform orbits around magnetic field lines with an angular frequency called cyclotron frequency. When cyclotron angular frequency is equal to the excitation

frequency of the electromagnetic field, i.e., the gyromotion of the free electrons is in resonance with microwave, the system is in *electron cyclotron resonance condition*. The main advantages of ECR plasma are the low operating pressures and the strong microwave coupling due to the magnetic confinement that generates higher electron temperatures. On the other hand, this magnetic confinement allows the use of ECR plasmas in remote configuration with respect to the reactor for the synthesis of thin films. This avoids the damage induced to sensitive substrates by energy ions characteristics of discharge plasmas.<sup>14, 16</sup> In addition, remote plasma configurations decrease the fragmentation processes (strength discharge decreases as coupling region distances) in the synthesis region as that produced in a plasma enhanced chemical vapour deposition (PECVD) reactor. For this reason, the work developed in the present Thesis has been carried out in a remote plasma reactor (described in the next section). This reactor design is also employed for polymers superficial treatments.<sup>17, 18</sup>

## 1.2 Introduction to Plasma Enhance Chemical Vapour Deposition (PECVD) and Plasma Polymerization

### 1.2.1 Plasma enhance chemical vapour deposition (PECVD)

Chemical vapour deposition (CVD) process is a vacuum technique for the deposition of thin films. It consists of the reaction among one or several gaseous or vaporized compounds to produce a solid product onto the substrates. This solid product is a new material fabricated from the original reagents, as opposed to physical vapour deposition (PVD) process, which a vapour of a previously synthesized material is condensed. The CVD reactions are produced by the activation of the precursor gases in order to raise the reaction rates, given that it is so low under normal conditions (pressure and temperature). The kinetics and reaction mechanisms are difficult to predict because the CVD reactions are highly complex. In view of this, the working procedure involves



previous empirical evidences and analysis to achieve the desired final material. Once it is analysed, the deposition technique facilitates to control the composition from the appropriate proportion of reactives/reagents to the desired specific properties of the resulting final material. The different activation methods of the reaction define the different CVD techniques: thermal activation, plasma or discharge activation, photon activation.<sup>15</sup>

In this thesis, we have developed new materials by plasma-enhance CVD (PECVD). In a PECVD process, an intense electric field produces a discharge that activates the molecules into the reactor, leading them to more reactive states. Consequently, the deposition rate is increased noticeably at given temperature, which enables depositions at lower temperatures than other synthesis procedures. This makes the technique compatible with precursors of low melting point being a property predominantly important for applications. The PECVD technique was initially developed in microelectronics (synthesis of conductors, semiconductors and insulators) and subsequently was spread to other fields, such as optics, ceramics and protective coatings and sensors.<sup>15</sup>

In PECVD, the typical operating pressures are between  $10^{-4}$  and atmospheric pressure. The supply of energy is generally used to generate and maintain the concentration of active species because lifetimes of plasma species are very short.<sup>15</sup> PECVD technique using microwave (MW) power source to excite and sustain plasma involve some advantages over plasmas generated by other kind of discharges (RF or DC). MW plasmas achieve higher ionization degrees, lower and broad range of operating pressures and not require the use of electrodes in the reactor. The discharge is produced by an electromagnetic wave excited at a frequency of 2.45 GHz, which is generated by a MW power source and guided by a waveguide into the reactor.<sup>14, 15</sup>

In spite of its benefits, PECVD shows two main disadvantages, impurities in the end material and damage by plasma radiation. Both, the

impurities in the thin film derived from the decomposition of reactive gases in radicals (-NH,-OH) and plasma radiation contribute to the degradation of the deposited material properties.<sup>15</sup>

### 1.2.2 Plasma polymerization

Plasma polymerization is a well-established technique of synthesis that involves the fabrication of a polymeric material from an electric discharge in an organic gas at atmospheric or low pressure, typically in the form of thin film.<sup>19</sup> In a few cases, inorganic gases and compounds may also form organic *plasma polymers*, reason why the formation of amino acids in the primeval atmosphere of Earth is explained.<sup>20-22</sup> As affirmed by A. Grill, “*Plasma polymerization is essentially a PECVD process resulting in the deposition of an organic polymer*”<sup>14</sup>. Plasma polymers establish a new type of material, different from conventional polymers and inorganic materials. In contrast with conventional polymers, they do not exhibit regularly repeating ensembles. The mechanism of plasma polymerization differs strongly from known conventional chemical polymerization mechanisms. Their monomer chains are shorter and randomly rearranged causing a high degree of crosslinking. Therefore, plasma polymerization is a complex process in which different chemical reactions take place between plasma and surface species, as well as among each one<sup>19</sup> Figure 1.2). Historically, the plasma polymerization process mechanisms has been analysed and modelled<sup>20, 23-30</sup> in many instances depending on the monomers and other parameters of synthesis.<sup>14, 19, 20, 24, 31</sup>

During the process of low-pressure glow discharge plasmas, the following plasma-induced deposition situations can be distinguished:<sup>20</sup>

- Radical and ionic chain growth polymerization mechanism. Plasma-produced radical fragments, radical-sites at solid surfaces or gaseous monomers can initiate a chemical process as

classical chain-growth polymerization by continuous addition of monomers. Similar ionic chain growth mechanism may also occur in the plasma. But low pressure hinders chain propagation.

- Ion-molecule reactions, based on charge transfer between atoms or dissociative charge transfer between molecules.
- Fragmentation-(Poly) Recombination (plasma polymerization). Plasma induces the fragmentation of the original monomers to atoms and small fragments by a steady bombardment of the monomer molecules and the *polymeric* material surface with high-energy particles and UV irradiation. It entails the following mechanisms:
  - Monomer fragmentation-poly recombination
  - Monomer conversion to polymer-forming intermediates partially-defined structural elements
  - Co-monomer fragmentation-recombination
  - Radical chain growth copolymerization
  - Graft copolymers. Chemical grafting onto radical sites or functional groups of plasma polymers or plasma-exposed polymer surfaces

H-abstraction, double bond formation, radical formation, crosslinking or degradation, loss in supramolecular structure and oxidation via peroxide formation are the resulting products in the course of a plasma polymer deposition. The obtained materials present a disordered structure formed by poly-recombination of these fragments (radical) and atoms that depends on the intensity and energy of the species bombarding the growing film.<sup>19, 20, 32</sup> Moreover, the multiple poly-recombination processes produce enthalpy dissipation, which can lead to local thermo-chemical processes contributing to end plasma polymers. Endothermic dehydrogenation of monomers and plasma

polymer is an example of these reactions that lead to the formation of double and triple bonds. On the other hand, radicals trapped in the deposited plasma polymer can react with oxygen when it is exposed to the ambient.<sup>20</sup>

Plasma polymer analyses have proved its structural and compositional irregularity,<sup>33-45</sup> with only a few structural elements derived from the monomer in the end deposited material. In general, aromatics rings are less represented as expected in plasma polymer,<sup>20, 33, 34, 37</sup> while non-aromatic double and triple bonds<sup>33, 34</sup> and high concentrations of CH<sub>3</sub>-groups by hydrogenation of broken chains,<sup>36, 46-49</sup> are observed.<sup>20</sup> Plasma polymers do not manifest a sharp melting point. On the contrary, a broad regime of softening begins to certain temperature. The films sometimes become darker during heating.<sup>20, 40</sup>

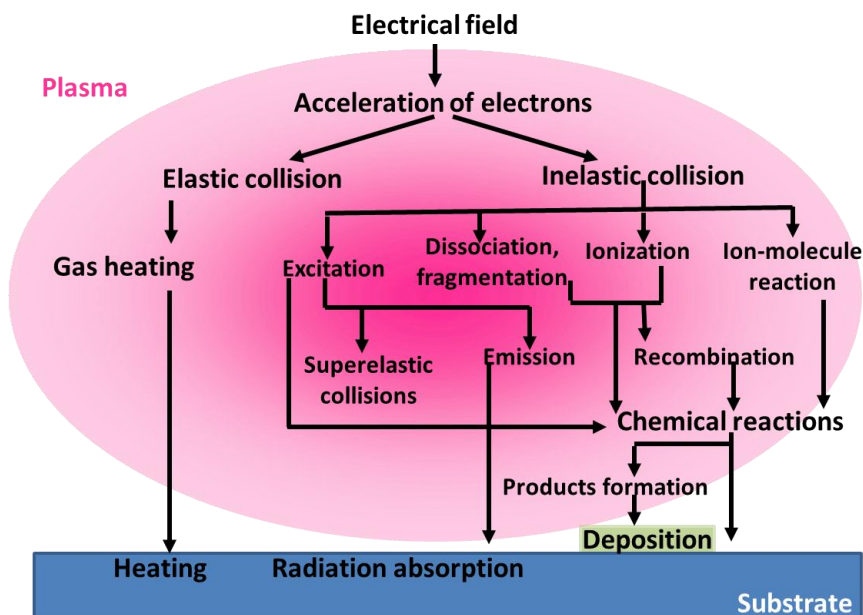


Figure 1.2. Processes involved in plasma polymerization – Scheme of energy distribution to collision and radiation processes during plasma polymerization deposition.<sup>20</sup>

Finally, the relevance of plasma polymers lies in their applications as coatings of solids with corrosion-inhibition, abrasion-resistance, chemical, permeability and optical properties.<sup>19</sup>

### 1.3 Remote Plasma Assisted Vacuum Deposition (RPAVD)

As already mentioned, in a conventional plasma polymerization process, the vapour pressure of an organic precursor is dosed into a plasma discharge for the synthesis of a solid thin film. During this complex process, the breaking of the starting monomer takes place, as well as different chemical reactions between the resulting species (reactive and stable groups), fragmentation and reorganization processes.<sup>14, 16, 19, 50, 51</sup> The resulting materials are highly cross-linked organic films formed by the plasma fragmentation and recombination of the precursor molecules. Generally, crystalline and supramolecular structures are absent in plasma polymers, while the formation of linear molecules and oligomers are most likely<sup>20</sup>. Otherwise, plasma polymers that retain original bond structures or functional groups of starting precursor groups have also aroused interest for researchers since films can present the combination of plasma polymer properties with monomer functionalities. Experimentally, these approaches have consisted in the use of higher operating pressures, the restriction of exposure to the plasma by pulse discharges and other approaches.<sup>11, 20, 52, 53</sup>

In last few years in our laboratory, a synthesis technique called remote plasma assisted vacuum deposition (RPAVD) has been developed for the deposition of functional thin film as dye containing plasma polymers.<sup>4-10, 54</sup> The scheme of the RPAVD reactor is showed in Figure 1.3. The process combines a remote plasma discharge with vacuum deposition of an organic solid monomer on substrates placed in the afterglow, see Figure 1.3. During RPAVD process, a

plasma polymer matrix retaining a substantial amount of whole functional precursor molecules are grown on the substrates. In contrast to conventional plasma polymerization, these precursor molecules have not been completely fragmented by the discharge due to a fine regulation of the interaction between the low power microwave plasma and the precursor molecules sublimated in the afterglow region. This is achieved by the simultaneous adjustment of different deposition parameters, namely MW power, the total pressure, the sublimation rate and the geometrical arrangement used for the deposition. From previous results, the distance between the plasma and the growing film ( $z$  in Figure 1.3) is one of the main operating parameters of RPAVD process, given that it controls the interaction between plasma discharge and precursors molecules.<sup>6-8, 11</sup> This distance, limiting the plasma-precursor interaction, makes largely versatile the deposition process, inasmuch as gradually regulates the film properties. Only modifying it, the method provides a wide range of films, from a highly cross-linked plasma polymer without the retention of original precursor monomers (deposition at the glow discharge), to plasma films containing a controllable amount of active dye molecules (deposition in afterglow).<sup>6-8, 11</sup> Increasing more the distance  $z$ , the films are seemed to those prepared by vacuum deposition (without plasma). Furthermore, the influence of the deposition rate was also investigated.<sup>11</sup> In general, we have founded a relationship among the operating parameters (the distance between the plasma and the growing film, pressure and deposition rate). Thus, increasing the distance is equivalent to reduce the power and to increase the deposition rate.

In brief, the main objective of the use of RPAVD process is to fabricate thin films that provide less cross-linked structures than plasma polymerization technique and more highly functionalized materials for many applications by the incorporation of functional groups of the monomers. Hence, the method has

been used for applications as photonic layers with tailored luminescent and optical properties,<sup>8-10, 54</sup> and photonic gas sensors.<sup>6, 7, 11</sup>

### 1.3.1 Experimental system

The experimental setup used for the deposition has been described repeatedly.<sup>6, 55</sup> A scheme of the system is shown in Figure 1.3. It consists of a chamber with two zones, the plasma zone and the deposition zone. In the plasma zone, a discharge is produced by MW applied to the plasma chamber through a flat Pyrex window, and is sustained under ECR conditions thanks to a set of magnets surrounding the chamber. In the deposition zone, there is a substrate in a remote configuration with respect to the plasma zone and two different Knudsen cells (evaporators) to sublimate the dyes. Additionally, an external and heatable glass ampoule is connected to the deposition chamber in order to supply a regulated vapour pressure of an additional precursor inside the reactor. The system is pumped up to  $10^{-6}$  mbar base pressure before the deposition. The distance between the sample-holder and the plasma zone,  $z$ , (a critical parameter for the control of the process as already mentioned) has been measured according to the Figure 1.3. The pressure of the system was controlled by an automatically regulated pressure controller connected to a capacitance pressure gauge (Baratron). Gases were dosed to the plasma chamber using a calibrated mass flow controller (MKS). The growth rate was controlled by a quartz crystal microbalance located in the same plane than the substrates. The deposition and/or treatment experiments have been carried out by using Ar and O<sub>2</sub> as the plasma gas. The microwave power range was 30-270 W and the gas pressure during the discharge  $10^{-1}$ - $10^{-3}$  mbar. The reflected power measured was less than 10 W. It was minimized by achieving a good coupling between the rectangular and the circular waveguides. This ECR system was characterized previously by two diagnostics methods, a Langmuir probe and an electrostatic energy

analyzer.<sup>56</sup> Later, the plasma characterization by optical emission spectroscopy (OES) showed the fragmentation of the evaporated dye molecules by interaction of the dye molecules with the electrons of the plasma. During the plasma deposition of Rh6G with Ar as the plasma gas, C<sub>2</sub>, CN, and CH<sub>x</sub> species were detected in the plasma. C<sub>2</sub> species can be considered as an intermediate species of the formation and/or etching of carbon materials with plasmas of Ar. The detection of C<sub>2</sub> together with CN and CH<sub>x</sub> indicated that the dye molecules coming from the Knudsen cell are effectively activated and a part of them even fragmented by interaction with the plasma. In general, an increase in the pressure of the plasma gas produces a decrease in the kinetic energy of the plasma electrons.<sup>6</sup>

Measurements of the electron density as a function of pressure showed a maximum in the electron density at approximately  $7 \times 10^{-3}$  Torr. The ion flux was measured as a function of the working pressure in the centre of the chamber. It was higher under low pressures, decreasing rapidly as the pressure or the distance,  $z$ , increased. These measurements also showed that the ion energy distribution function (IEDF) shifts to lower energies for higher pressures.<sup>56</sup> Plasma polymerization occurs while the dye is being sublimated. The deposition process was controlled by a quartz crystal monitor placed besides the substrate in the deposition zone. Typical growing rates between  $\sim 2\text{--}5$  nm min<sup>-1</sup> were achieved by controlling the heating of the Knudsen cells. These relatively low growth rates were selected to efficiently control the deposition of thin films of  $\sim 50\text{--}500$  nm.<sup>6</sup>



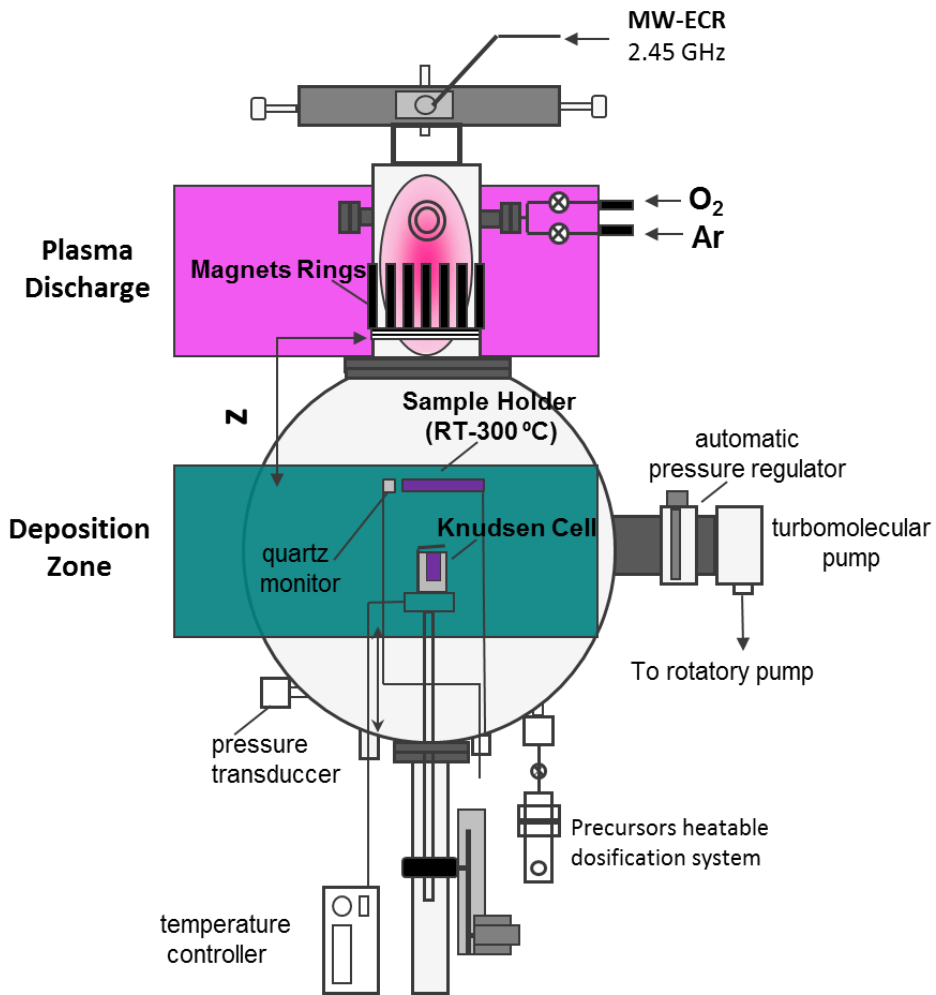


Figure 1.3. RPAVD reactor – Scheme of the main components of a remote plasma assisted vacuum deposition reactor for the fabrication of organic thin films and nanostructures.

### 1.3.2 Thin film characteristics

Up to the present, it has been developed materials by RPAVD from several organic dyes: rhodamine 6G (Rh6G), ethyl red (ER), perylene (PE), 3-hydroxyflavone (3HF) and perylene-diimide (Me-PTCDI) in our research group. A general overview of the remarkable characteristics and achievements in this technique is provided below.

#### 1.3.2.1 Microstructure and surface morphology

The superficial morphology and microstructure of RPAVD films have been studied through scanning electron microscopy (SEM) and atomic force microscopy (AFM). Films grown on silicon (100) and fused silica substrates are smooth, homogeneous and free of cracks and dye micro aggregates,<sup>5, 7</sup> thereby the films do not scatter the light. These properties are indispensable in photonics applications. In Figure 1.4, typical SEM micrograph of a different RPAVD films on silicon (100) are compared with its respective structured material grown from same dye by vacuum deposition (without plasma) for each case. The materials deposited in absent of plasma (on the left in the Figure 1.4) are formed by dye microaggregates, which are responsible of light dispersion. In addition, these composites are weakly adhered to the substrate and are mechanically unstable, and can be removed easily by paper brushing or by immersion in water. Others methods, such as sol-gel,<sup>57-59</sup> try to incorporate dye molecules in a high concentration in solid host materials also present the same problem.<sup>5</sup> RPAVD films (on the right) do not show any observable contrasts regardless of the dye and present good adhesion to the substrates. In spite of some slightly topography differences distinguished by AFM measurements, all the samples deposited from different dye, different polymerization degrees<sup>7, 8</sup> and thickness (50–1000 nm) show low RMS values (<0.5 nm), Figure 1.5.

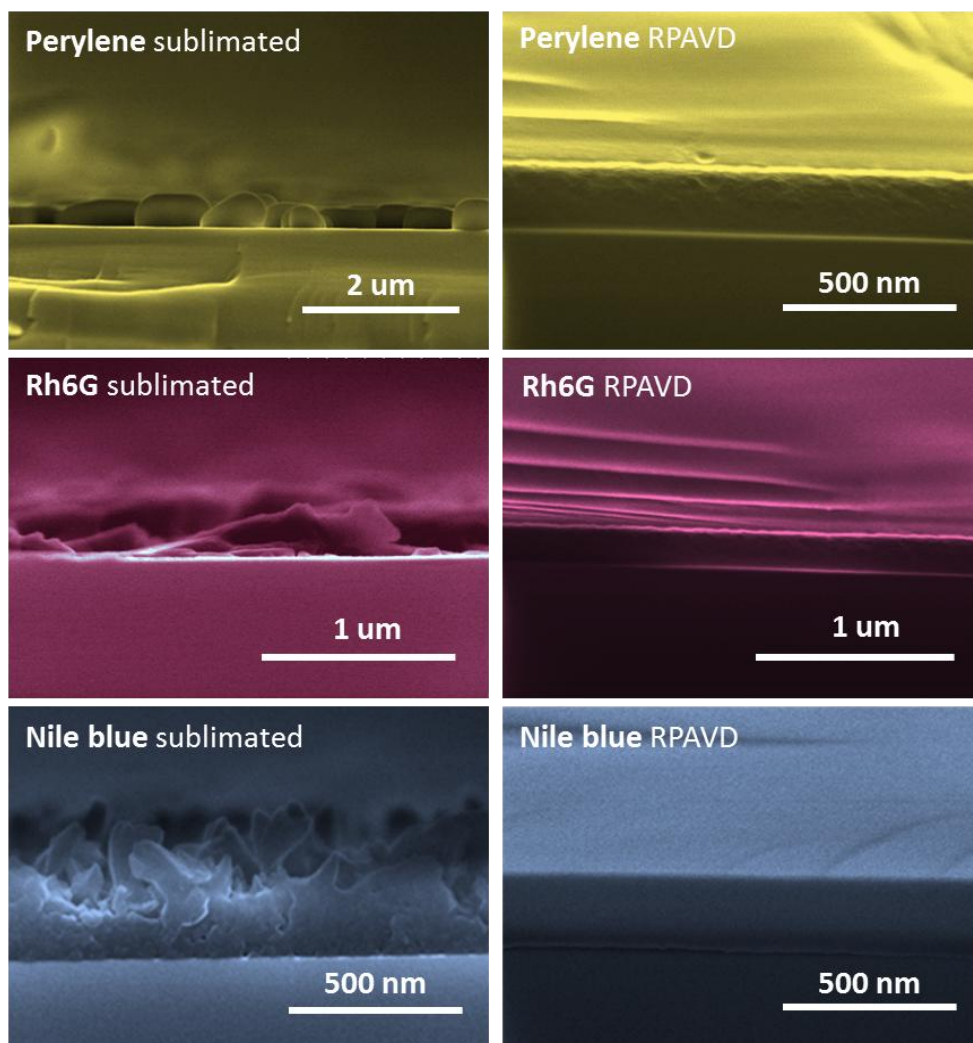


Figure 1.4. Planarity of RPAVD thin films – SEM micrographs comparing three sublimated organic dyes on the left, and RPAVD thin films grown from the same dyes, on the right.

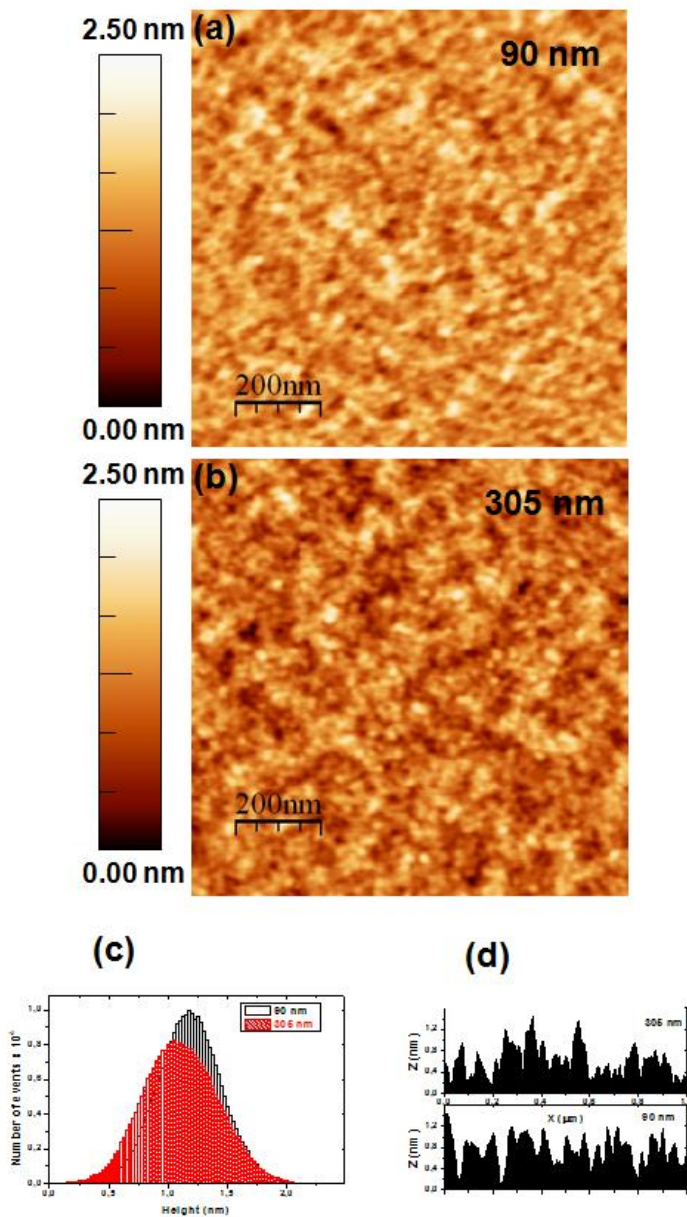


Figure 1.5. Surface morphology of two RPAVD- (a,b) AFM micrographs in tapping mode of thin films of two thickness of 3-hydroxyflavone thin films, (c) height distribution of motives, and (d) line profiles obtained from pictures (a) and (b).<sup>11</sup>

### 1.3.2.2 Composition and structure

The composition of the deposited films from Rh6G<sup>4, 8</sup>, ethyl red<sup>6</sup>, perylene<sup>7, 10</sup> and 3HF<sup>11</sup> dyes was characterized by a X-ray photoelectron spectroscopy (XPS) and Fourier transform infrared (FTIR). The results indicate clearly that the plasma produces partial fragmentation and cross linking of the dye molecules in the films. The main differences between the evaporated and the plasma polymerized thin films in XPS spectra are a relative decrease in the carbon content and oxygen enrichment in the polymeric film.<sup>4</sup> The origin of the oxygen is caused by post-deposition reactions of the samples exposed to the air or from direct incorporation of oxygen from the reactor during the deposition.<sup>24, 31</sup> FTIR of plasma polymerized films shows less intense and broader features than evaporated layers at similar wavelengths.<sup>4, 6-8, 10, 11, 31</sup> An additional wide and intense band due to O-H vibrations (at 3350 cm<sup>-1</sup>) was observed in the plasma films. Furthermore, time of flight secondary ion mass spectrometry (ToF-SIMS) analysis verified the incorporation of integer dye molecules into the polymeric matrix<sup>7, 10, 11</sup>.

Figure 1.6 shows two ToF-SIMS spectra of perylene and 3HF RPAVD films. The peaks at *m/z* values around 252 and 239 in perylene and 3HF spectra respectively are identified with the dyes molecular ion<sup>10, 11</sup>. Thus, these peaks correspond to a certain percentage of intact molecules of the each dye incorporated into each RPAVD film. Nonetheless, a group of peaks at *m/z* < 100 u.m.a., associated to C-H (O) in the polymeric matrix, prevails in the spectra.

Thus, the films are more robust, mechanically stable, and as previously mentioned, show higher adhesion to the substrates than the sublimated layers. In addition, depending on its cross-linking degree, the technique permits to fabricate composites that are insoluble in water and organic solvents.<sup>4-11</sup>

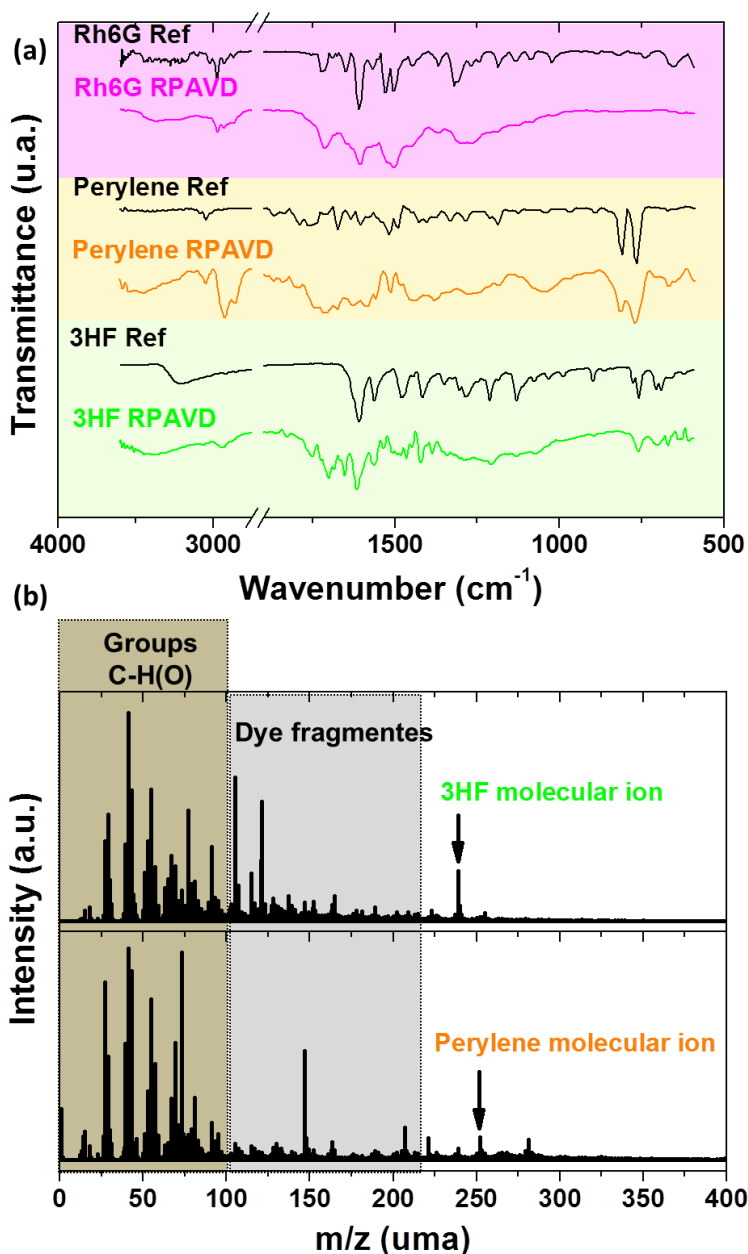


Figure 1.6. Chemical characterization of RPAVD films- (a) FTIR spectra of RPAVD thin films from different dyes (rhodamine 6G, perylene and 3-hydroxyflavone). Spectra of sublimated (withouth plasma) Rh6G, sublimated perylene and a KBr tablet with 3-HF have been included as references. (b) ToF-SIMS spectra of RPAVD thin films from perylene and 3-hydroxyflavone dyes.<sup>60</sup>

### 1.3.2.3 Optical characterization

Optical properties of the RPAVD analyzed by UV-visible and fluorescence spectrometers ratify the existence of intact dye molecules in the films.

Figure 1.7 shows the UV-visible spectra of several types of RPAVD films with different colour absorption. The transmittance spectra show characteristic absorption bands of the dye used as precursor.<sup>4-11</sup>

In last works, it has been reported planar Rh6G RPAVD thin film as a good option for deposition of materials composed by a matrix incorporating integer Rh6G,<sup>4, 5</sup> due to the interest in solid-state lasing, optoelectronics, optical filters applications. The developed procedure yielded light-absorbent and fluorescent thin films. Regardless, it is worth noting that Rh6G RPAVD films showed reduced light absorption compared to the sublimated film. This effect is more noticeable in samples that were grown closer to the plasma.<sup>5, 8</sup>

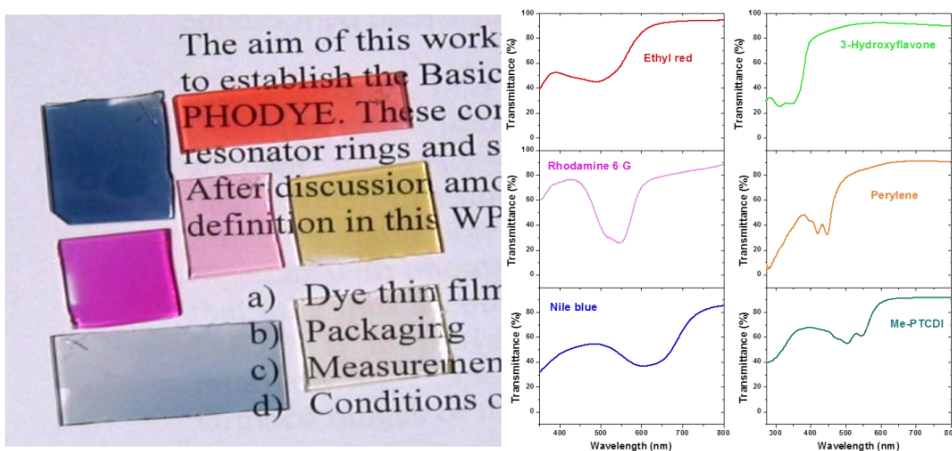


Figure 1.7. Optical properties of RPAVD films – The picture shows a set of RPAVD samples grown from different organic dyes (rhodamine 6G, rhodamine B, perylene, Nile blue and ethyl red). On the right, there are the transmittance spectra of some RPAVD films.<sup>60</sup>

The dye containing thin films were also studied by spectroscopic ellipsometry.<sup>7, 10, 11</sup> The analysis of perylene thin films demonstrated that the refractive index can be adjusted as a function of the plasma conditions using a single dye.<sup>7</sup> In addition, these studies evidence that films are transparent in the region corresponding to the fluorescence emission and at higher wavelengths because the extinction coefficient,  $k$ , decreases for wavelength longer than the value for the maxima absorption. On the other hand, the analysis of copolymerization between two precursors (perylene and adamantane) indicated that the refractive index,  $n$ , of the films can be also adjusted in function of the composition.<sup>10</sup> Figure 1.8 shows the differences among the refractive index measurements for RPAVD films deposited from adamantane, perylene and different concentrations of perylene-adamantane. Later ellipsometry studies with 3HF also suggest that the optical properties can be finely adjusted within a wide range for the suitable integration of the films in photonic structures.<sup>11</sup>

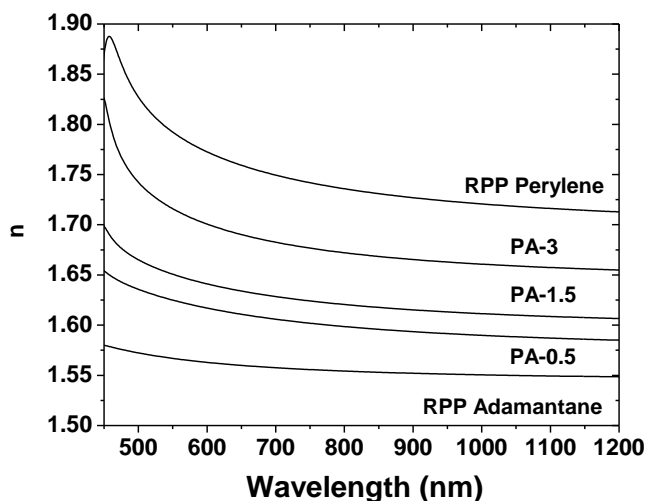


Figure 1.8. Refractive index for a set of perylene–adamantane (PA) – The refractive index have been determined by variable-angle spectroscopic ellipsometer (VASE) remote plasma deposited films prepared from: lowest to highest concentration of perylene-adamantane (PA-0.5, PA-1.5, PA-3), only adamantane (RPD-A) and only perylene (RPD-P).<sup>10</sup>



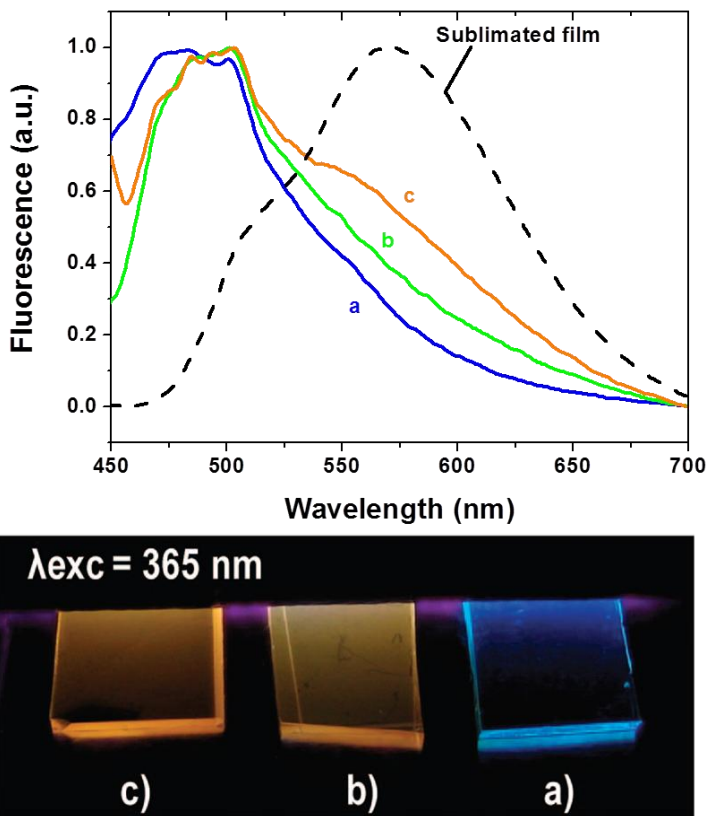


Figure 1.9. Photoluminescence of perylene thin films – On top, the graphic shows normalized photoluminescence spectra of a set of perylene RPAVD thin films grown under different experimental parameters (i.e., distance between sample-holder and the plasma zone, and MW power source). The spectrum of a sublimated sample is included as a reference. An image of these samples illuminated with a UV lamp ( $\lambda=365 \text{ nm}$ ) in a dark room is shown below.<sup>7</sup>

Works using perylene and 3HF dyes as sole organic precursors have confirmed the growth of luminescent polymeric thin films by RPAVD. The control of the interaction between sublimated perylene dye and plasma species during the preparation of the films is possible by varying experimental conditions. Therefore, we can tailor the dispersion degree of the dye in the film matrix selecting the experimental conditions.<sup>7, 11</sup> These distinct types of films presented different properties. As an illustration the thin films containing

dispersed perylene molecules (lower dye-plasma interaction) did not disperse the light and showed blue light luminescent emission (Figure 1.9). While, the luminescent emission shifts to longer wavelengths, i.e., orange luminescent emission of light, as the percentage of nanoaggregates increases<sup>7</sup> (greater dye-plasma interaction).

#### 1.3.2.4 Sensor response

Immediate applications of the perylene dye containing thin films are the use of them as nanometric long pass optical filters, due to the complete light absorption at wavelengths lower than 470 nm (Figure 1.7).<sup>7</sup> Moreover, thin films with a high concentration of perylene molecules within the matrix formed a by molecular fragments of the dye were proposed for optical nitrogen dioxide sensing because of the changes in colour and fluorescence emission observed when they are exposed to NO<sub>2</sub>. These films depicts a good choice for the development of integrated photonic NO<sub>2</sub> gas sensors such as optical dosimeter for the remote monitoring of the degradation of high explosive materials<sup>7, 10, 61</sup>. Some limits were found in the detection sensitivity (<15 min of exposure to a NO<sub>2</sub>/air flow of 0.5 ppm). The aforementioned modification of the perylene RPAVD method by adding adamantane molecule during the process also brought improvements in the sensitivity of the films. Plasma polymerized adamantane films are transparent in the visible range and NO<sub>2</sub>-permeable. For this reason, adamantane molecules were selected as precursor of the polymeric matrix for this sensing function. Thus, a set of photonic sensors films with different sensitivities were fabricated by adjusting the optically active molecule of perylene concentration within the transparent polymeric adamantane matrix films.<sup>10</sup> These materials provide the possibility to adapt the sensitivity to required environmental necessities. Figure 1.10 shows the complete process from the sensing film deposition at wafer scale to the real implementation of

these thin films in a photonic sensor prototype for measuring the pollution in a traffic tunnel.

Recently, a new kind of photonic organic thin film was synthesized from a flavonoid compound, 3-hydroxyflavone (3HF), by RPAVD technique. These films were implemented as active components in photonic structures used for the fabrication of devices such as UV sensors, UV-to-visible wavelength shifters and UV.<sup>9</sup>

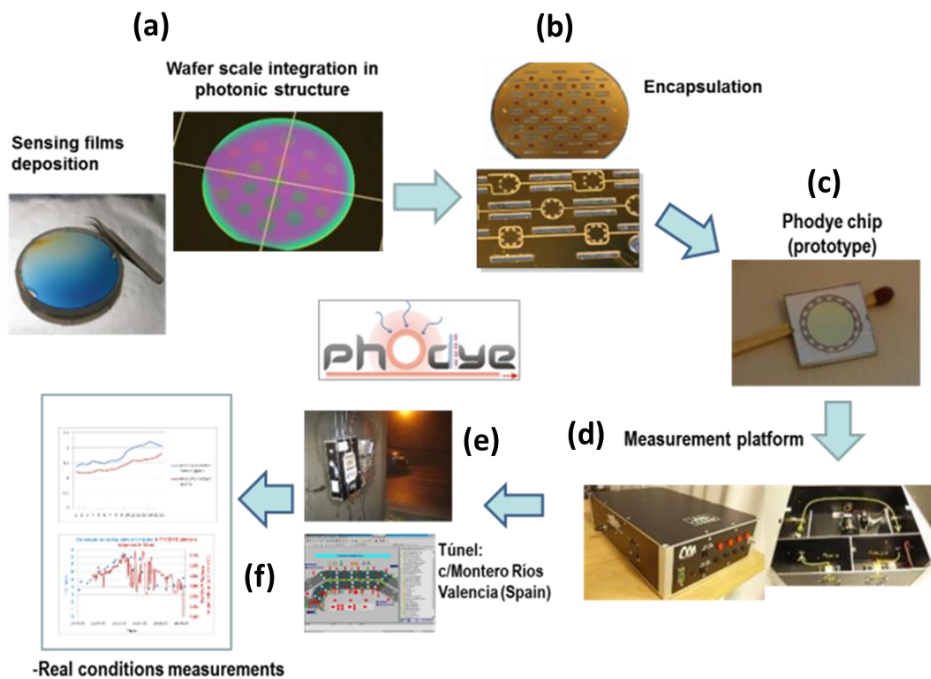


Figure 1.10. Process for the fabrication and implementation of a photonic system on a chip based on perylene dye for sensor application – The picture gathers step by step the process from de fabrication of the sensor to its implementation in real conditions measurements: (a) wafer scale synthesis of sensing photonics chips from RPVD technique, (b) chips encapsulation at wafer scale, (c) prototype chip, (d) integration of the chip in in  $\text{NO}_2$  detection platform, (e-f) the system installed in a real scenario (urban tunnel).<sup>60</sup>

Polymeric thin films from 3HF by RPAVD have resulted transparent in the visible range (at wavelengths higher than 390 nm), absorbent in the UV and shown an emission at the visible range (green emitter).<sup>11</sup> Figure 1.11 shows a 3HF RPAVD film and quartz substrate without (a) and under (b) UV illumination. 3HF molecules in solution and under UV illumination show two types of fluorescence emission, blue and green emissions. The blue emission was assigned to the normal form of 3HF. Large Stoke shifted emission in the green was associated to the tautomer generated through an excited state intermolecular proton transfer mechanism (ESIPT), in which, when the molecules are in the excited state, one hydroxyl proton is transferred to a neighbouring carbonyl group. It is a very efficient and non-radiative energy dissipating mechanism<sup>9, 11, 62-65</sup> and substantially sensitive to the chemical environment surrounding the 3-HF molecules, particularly to the formation probability of H bonds with nearby molecules or groups. Therefore, the relative intensity of the blue and green emission bands can be controlled by the hydrogen bond donor ability of the environment.<sup>62, 64</sup> Fluorescence time resolved analyses of RPAVD films indicated that 3HF molecules were trapped in indifferent chemical environments. In some cases, green emission was partially quenched. This also modifies the efficiency of the ESIPT process. These two factors affect the quantum yield of the trapped dye molecules. According to this interpretation, the fluorescence efficiency of the films could be further enhanced by the fine adjustment of the chemical structures forming the plasma polymer host matrix. Moreover, the emission is noticeable even under ambient light conditions due to the high light absorption of these nanometric films and the large Stokes shift (i.e., absence of reabsorption).<sup>11</sup> The large Stokes shift (180 nm) of the green emission of the samples illuminated in the UV region (350 nm) and the lack of fluorescence under visible irradiation made these films good candidates as wavelength shifters and UV photodetectors. This application has been

successfully proved in films that remain stable the fluorescence under UV irradiation of  $156 \mu\text{Wcm}^{-2}$  after pre-irradiation treatment, and were capable to detect very low UV light intensities below  $10 \mu\text{Wcm}^{-2}$  (close to the detection limits of some commercial detectors), see Figure 1.11.

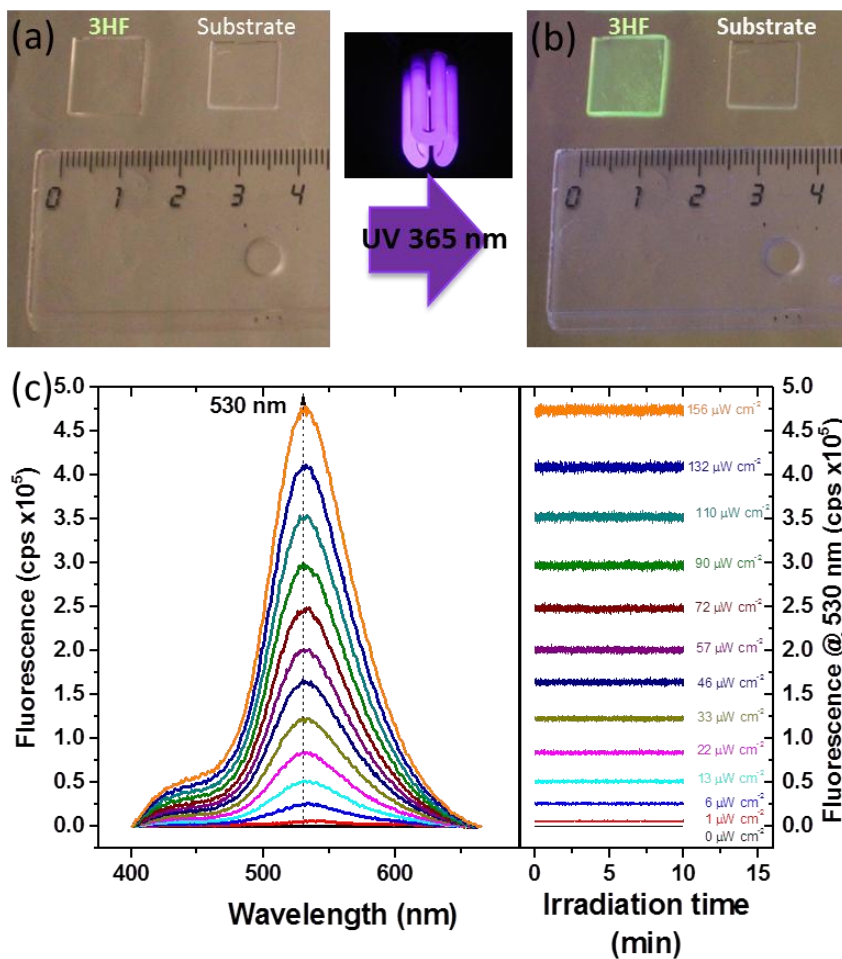


Figure 1.11. Photoluminescence under UV illumination of 3HF thin films- (a,b) Images of both 3HF RPAVD thin film and the substrate used in the deposition (as reference) before and after illuminating with a UV lamp ( $\lambda=365 \text{ nm}$ ). (c) Emission spectra as a function of the UV irradiance. The graphic on the right shows the stability of the emission intensity at 530 nm for the samples when they are illuminated during 10 min with different UV intensities.<sup>11</sup>

### 1.3.2.5 Lithographic processing

Additionally, separated studies demonstrate the possibility of processing plasma polymeric films using shadow masks, either during the deposition process or in an after-etching process.<sup>7</sup> In this perspective, the method enables the selective deposition of the surfaces accordingly the implementation in photonics devices<sup>9</sup> and encryption applications for labelling. Figure 1.12 (b, c) shows the direct observation of the fluorescence light paths in two photonic structures incorporating the 3HF films: a Fabry–Perot resonator (b) and a ring resonator (c).<sup>9</sup>

The Fabry–Perot structure is based on a silicon nitride multimode strip waveguide with a width of 10  $\mu\text{m}$  and a height of 300 nm. The lower cladding is a 5  $\mu\text{m}$ -thick  $\text{SiO}_2$  layer grown on Si. The planar F–P resonator consists of  $\text{Si}_3\text{N}_4$ /air pairs separated 90 nm with a cavity height of 140 nm. The dye layer was selectively deposited through a mask, only onto the resonant microcavities. The waveguide and resonator structure are designed to transmit the 3HF emission up to the output, even if there are several transmission modes. Figure 1.12 (b) shows a fluorescence microscopy image of the 3HF active area covering the resonator structure. The fluorescence light is selectively transmitted through the waveguide and the transmission modes of the fluorescence emission are modulated by the F–P resonant cavity at the edge of the output waveguide.

The second photonic structure consists of a disk resonator and a  $\text{Si}_3\text{N}_4$  strip forming a high refractive index waveguide and a  $\text{Si}_3\text{N}_4$  strip forming a high refractive index waveguide. The waveguide cross section was 600 nm and its height was  $\approx 80$  nm, a topology that only permits the propagation of the fundamental transverse electric (TE) mode. The lower cladding was a layer of  $\text{SiO}_2$  with a thickness of 5  $\mu\text{m}$  on a Si substrate. The upper cladding was also  $\text{SiO}_2$ . A window through this  $\text{SiO}_2$  upper cladding was open over the resonant disk and nearby waveguide to enable that the active 3HF film is selectively

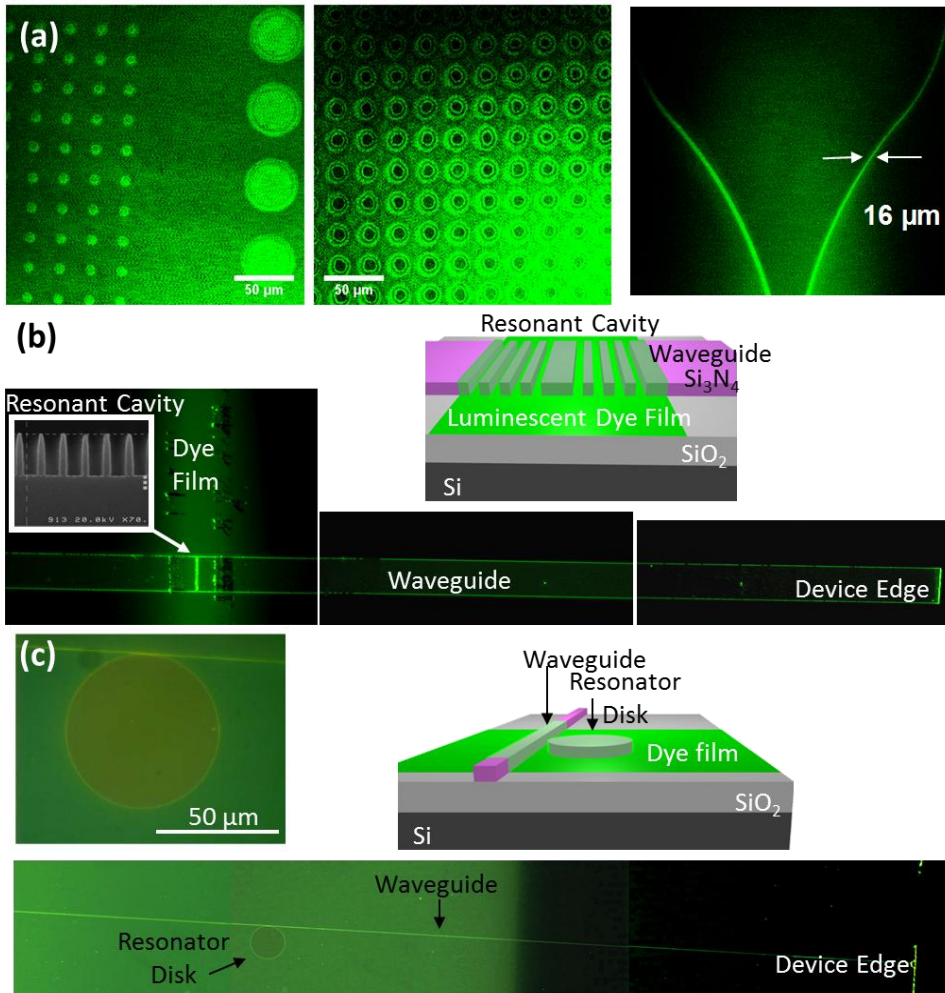


Figure 1.12. Processing and photonics implementation of RPAVD films –Fluorescence microscopy images taken of: (a) 3HF films deposited and exposed to oxygen plasma (sample at the centre) through masks designing a squared pattern and two lines of a waveguide structure, (b) surface view of a Fabry - Perot resonator coated with 3HF RPAVD film. (c) surface view of a resonator disc of 120  $\mu\text{m}$  diameter coated with 3HF RPAVD film. It is remarkable the possibility of observing the emission at the device edges which were not coated

deposited onto this zone. The design and dimension of this photonic structure is such that the waveguide can couple the green fluorescence emitted by the active 3HF film. The green light is collected and transmitted up to the waveguide output in the chip edge. This preferential distribution of the fluorescence light supports the conclusion that the field intensity is higher in the disk and is transmitted through the waveguide out of the 3HF-coated region up to the border of the structure, as shown in Figure 1.12 (c).

#### 1.3.2.6 Wafer scale and sensitive substrates

Other relevant achievements have emerged in the development of RPAVD technique. The process enables wafer-scale fabrication for industrial application such as microelectronics and optoelectronics<sup>10</sup> (Figure 1.13). An example of the application of RPAVD films at wafer scale has been introduced in previously section. Perylene-adamantane RPAVD thin films have been implemented in a sensor photonic system of NO<sub>2</sub>. Finally, the deposition of these films on sensitive substrates by RPAVD<sup>9</sup> has yielded an improvement in plasma deposition process. This technique avoids the common UV irradiation and ion bombardment damages of the surfaces produces by plasma processes that involve a disadvantage for these applications<sup>11</sup>. Figure 1.13 shows some examples of the luminescent RPAVD films coating sensitive substrates such as paper, polycarbonate and adhesive tape. Thus, the process involves soft plasmas providing the opportunity to use a wide range of substrates which are not available in other plasma techniques of deposition.



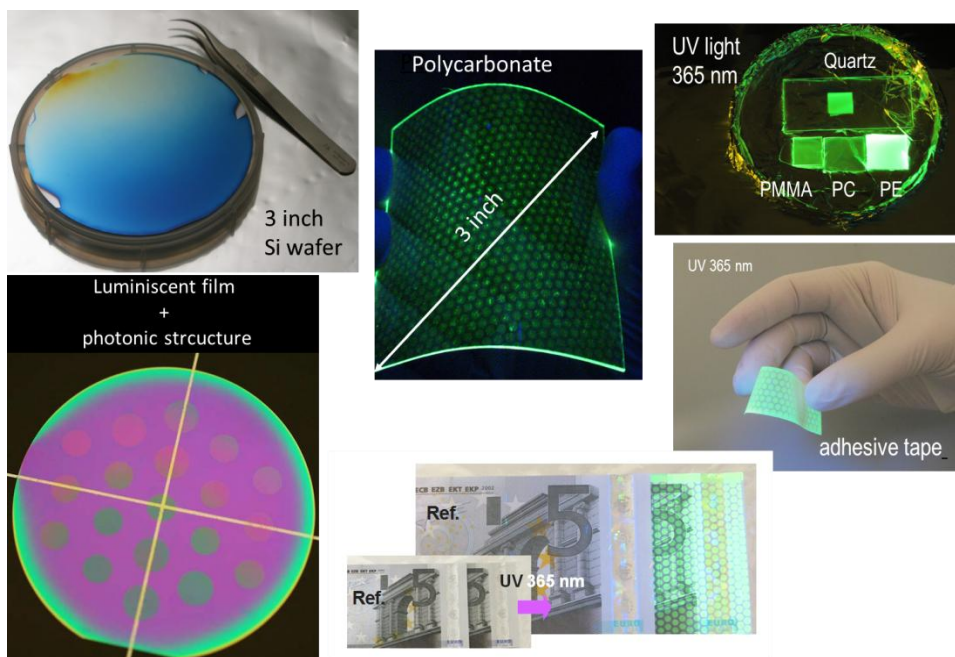


Figure 1.13. Wafer scale and sensitive substrates in RPAVD films – Images of perylene RPAVD films at wafer scale and 3HF RPAVD films coating several sensitive substrates, such as polycarbonate, PMMA, adhesive tape or a five euro bill.

## 1.4 Fundamentals of 1D organic nanowires

One-dimensional (1D) nanomaterials of  $\pi$  conjugated organic molecules in electronic and optoelectronic devices at nanoscale become of great interest in nanoscience and nanotechnology. 1D nanostructures from inorganic materials have much thoroughly studied on inorganic materials. However, organic materials, less researched up today, show many advantages such as unlimited choices of molecular structures for property optimization, or high flexibility and low cost of materials fabrication, or high photoconductivity, or nonlinear optical effects. In fact, these materials have already used in the form of thin film as field-effect transistor (FETs), light-emitting diodes (LEDs) and photovoltaic

cells applications due to its peculiar electronic and optical properties<sup>66-68</sup>.

The relevance of organic  $\pi$  conjugated molecules lies in  $\pi$  electronic delocalisation, resulting from the intramolecular delocalised  $\pi$  electron cloud with its high polarisation<sup>68</sup>. Thus, the overlap between the electronic wave functions of neighbouring molecules, with its consequent increase in bandwidth, result in a face-to-face ( $\pi$ -stack) stacking, which are related to electrical conductivity in the coherent transport regime, providing an high charge-carrier mobility along the  $\pi$ - $\pi$  stacking direction<sup>67, 69, 70</sup>. In particular, one-dimensional structures by self-assembly via strong  $\pi$ - $\pi$  interactions from molecules with two-dimensional extended aromatic system, such as nanowires and nanoribbons/nanobelts, from perylene tetracarboxyl diimide (PTCDI) derivatives<sup>71</sup>, metal phthalocyanines and porphyrins<sup>72</sup>, and several other examples<sup>67</sup> has been reported. Figure 1.14 presents two examples of these types of nanostructures.

Overall, there are three prevalent strategies for the growth of organic nanowires<sup>72</sup> (ONWs): self-assembly via solution deposition<sup>67, 68, 73-80</sup>, template methods<sup>81-84</sup>, and vapour transport process<sup>72, 85-96</sup>. Due to the drawbacks during the use of the techniques based on solution processes and template method, the vapour transport method has been chosen as one of the most straightforward routes for organic nanowires and nanotubes fabrication. The solution processes pose shortcomings, such as the difficulties to control the size, morphology, or phase of the nanowires and to produce high-density arrays and pattern, which are not in solid vapour growth. Besides, single-crystal nanowires can be directly grown onto prefabricated devices by this technique. This fact avoids the requirement of elimination of template material (therefore the possibility of contamination) which is necessary in the fabrication of nanowires by template method<sup>72</sup>.

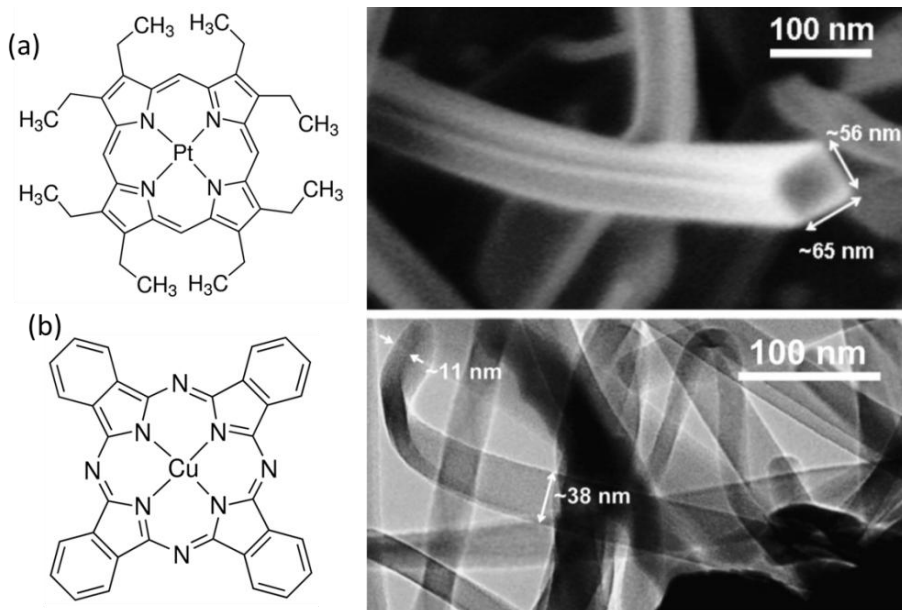


Figure 1.14. Supported single crystal organic nanostructures – Two examples of crystalline structures by  $\pi$ -stacking: (a) PtOEP molecule and high-magnification SEM image of a squared PtOEP nanowire. (b) TEM micrograph of a CuPc nanobelt.<sup>93</sup>

In last years, a vacuum deposition (PVD) of the molecule species for the fabrication of 1D-nanostructures from  $\pi$ -conjugated molecules procedure was developed. The sublimation of the molecules for the nanowires deposition on the substrates is carry out in a Knudsen cell at controlled growth rate and substrate temperature into a vacuum chamber. The evaporation cell and the substrates are spaced about 8 cm. During the experiments, argon was dosed using a calibrated mass flow controller and the pressure is fixed at 0.02 mbar. The growth rate is controlled by a quartz crystal microbalance in the same plane as the substrates. It is around  $0.4 \text{ \AA s}^{-1}$  considering a density in the balance of  $0.5 \text{ cm}^{-3}$ . The deposition takes place in the same reactor described in the previous section, but in this case without plasma assistance. The different factors, shape, length and thickness, controlling the formation of a high density of

nanostructures have been studied.<sup>72, 93</sup> Here the most significant factors are described briefly.

The control of the substrate temperatures during the deposition has led to different morphologies of nanowires: cylindrical nano rods, hexagonal nanowires, squared nanowires or nanobelts. Thus, the nanowire growth is a temperature-activated process, in which the substrates are heated to certain temperature related with sublimation temperature of each type of molecules<sup>72</sup>. Other key parameter for the synthesis of these nanowires is the presence of imperfections on the flat substrates<sup>93</sup>. The origin of the formation of organic nanowires is highly dependent on the substrate morphology and roughness which they will be supported, and independent of its chemical composition. The study of the deposition process has been extended on metallic and nonmetallic substrates<sup>72</sup>. The used substrates to confirm the generalization of the method were, on the one hand, oxidized silver/ Si(100)<sup>93</sup> grown by DC sputtering technique and later plasma oxidized<sup>91, 96-99</sup>, as well as gold/ Si(100)<sup>72</sup>, and on the other hand, oxide columnar and porous thin films (TiO<sub>2</sub>, ZnO, SiO<sub>2</sub> and Ta<sub>2</sub>O<sub>5</sub>) prepared by different techniques<sup>72</sup>. As an example, in the Figure 1.15, it shows that the growth on gold thin films result in the formation of large nanobelts with a lamellar microstructure, meanwhile, on substrates decorated with gold nanoparticles the nanowires development into nanobelts or squared nanofibers are similar to those on silver nanoparticles<sup>72</sup>. From this work, it follows that metallic particles and the oxide grains play the role of nucleation sites for the formation of the single crystal nanowires. The number and the size of the features on the substrate influence the formation of a high density of ONWs directly<sup>72</sup>.

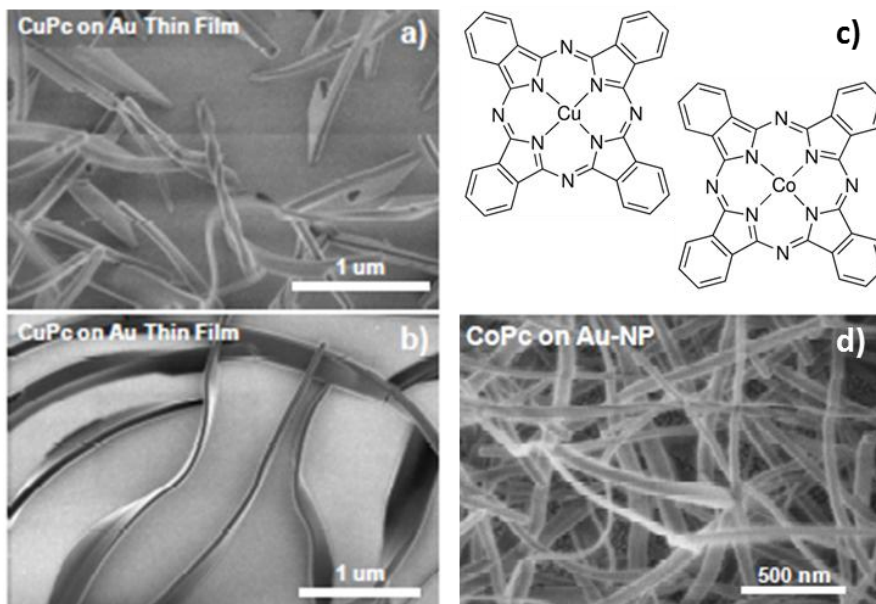


Figure 1.15. 1D nanostructures from  $\pi$ -conjugated molecules on Au substrates – (a) SEM micrographs of CuPc nanostructures grown on Au thin films. (b) SEM micrograph of CoPc nanowires grown on Au nanoparticles<sup>72</sup>.

A model of the growth and development of the crystal has been proposed<sup>72</sup>. It follows different stages, as schematized in Figure 1.16. The features on the substrates act as nucleation sites for the nanowire growth, as shown in Figure 1.16 (i). The method starts from the assumption of a high mobility of molecules. It is achieved by controlling the temperature of the substrates and its defects or impurities, and therefore, the number of molecules impacting the substrates. The molecules are subjected to adsorption and desorption cycles and move over the surface until forming the crystal nucleus on the nucleation sites provided by the substrate grains, Figure 1.16 (ii). In Figure 1.16 (iii-iv), is shown the growth of 1-D nanostructures by the mechanism of directional self-assembly via  $\pi$ - $\pi$  interactions. The formation of squared and belt nanofibers might depend either on the crystal habit or on the nucleus form and size<sup>72</sup>.

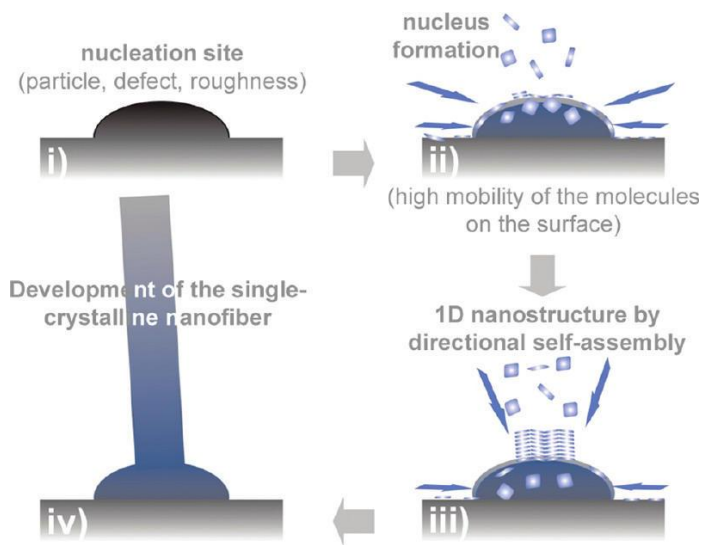


Figure 1.16. Scheme of the growth mechanism of 1D nanostructure- (i) Metallic particles, rough surfaces, or defects acting as nucleation sites. (ii) Formation of the crystal nuclei by the arrival of a high flux of molecules from the substrate at the nucleation site. (iii) Crystal formation by self-assembly of the molecules. (iv) Development of the single-crystalline 1D nanostructure<sup>72</sup>.

The generalization of this methodology to planar aromatic molecules that exhibit face-to-face ( $\pi$ -stack) stacking, such as Perylene, Porphyrins and Phtalocyanines, has been accomplished<sup>72, 91-93</sup>. In Figure 1.14, two examples can be seen.

Besides the advantages of simplicity, mild conditions, relative low substrate temperature, and high crystallinity and homogeneity of the obtained nanowires, this one step method also provided the possibility to grow simultaneously nanowires formed by different molecules, forming an open core@shell heterostructure. This type of 1D-dimensional coaxial organic heterostructure has been performed from two immiscible molecules, palladium octaethyl porphyrins (PtOEP) and copper phthalocyanine (CuPc), and analysed, by Ana Borrás et al.<sup>93</sup>

A subsequent work introduced a new methodology to fabricate connecting organic nanowires and nanosheets formed by  $\pi$ -conjugated

molecules via silver particles. The metal particles were deposited along previously primary nanowires by simple DC sputtering at room temperature without modifying the nanowire structures, with the purpose of acting as nucleation sites for the new organic nanowires. The silver nanoparticles served as electrodes connecting the nanowires. This opened new possibilities for the integration of the semiconducting organic nanowires into dense arrays for electronic, sensing, and catalytic applications<sup>96</sup>.

Applications based on the formation of high-density ONW film as superhydrophobic coloured surfaces have been reported<sup>100</sup>. Its implementation in microfluidics, decorative or optical devices, is of significant interest. In this work, the dependence of water contact angle (WCA) of ONW films formed, connecting ONW films and open core@shell ONWs films, by different metalloporphyrins and metallophthalocyanines, have been studied. Additionally, WCA dependence on the density of organic nanowires and UV and visible irradiation were characterized. Water contact angles higher than 150° were measured on the fabricated films whose surfaces were air-stable, chemically inert, and very robust to visible and UV light irradiation.

Recently, it has been shown the formation of supported hybrid core@shell NWs consisting in a single crystalline organic core grown by PVD and a conformal inorganic oxide shell (ZnO, TiO<sub>2</sub> and SiO<sub>2</sub>) grown by PECVD. This process provided the fabrication of wide band gap inorganic without damaging the ONWs. An application of these hybrid nanostructures as wide guided systems at the nanoscale was examined, founding that the fluorescence light produced by the organic inner core was effectively guided by the semiconducting shell towards the NWs tips<sup>101</sup>. It is illustrated in Figure 1.17.

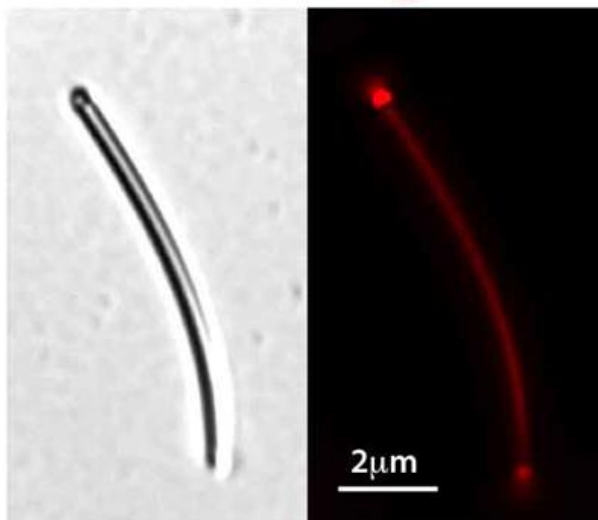


Figure 1.17. Fluorescence microscopy of hybrid core@shell NWs – MePTCDI@ZnO system micrograph recorded by using an excitation wavelength of 550 nm.<sup>102</sup>

In this thesis, the use of organic nanowires is addressed in different ways. On the one hand, from organic a metallorganic nanowires, the synthesis and characterization of hierarchical (branched) and hybrid Metal-NPs/organic supported NWs by plasma processing is developed (Chapters 7, 8 and annex 1). And, on the other hand, in order to take a step from the film to the nanowire and due to their interesting properties, nanowires are also used as degradable scaffolds or templates for the fabrication of RPAVD supported nanostructured materials. The combination of *plasma polymers* grown by RPAVD and these organic nanotemplates are presented in chapters 3, 4, 5 and 8.

## 1.5 Introduction to the growth and optical properties of ZnO

ZnO shows an ultraviolet luminescence band due to a wide band gap ( $\sim 3.37$  eV at room temperature) and high exciton energy (60meV)<sup>103</sup>. For these optical properties, it is used in the realization of electroluminescent diodes or room temperature UV lasers<sup>104</sup>. Besides the UV emission, the



photoluminescence spectra at room temperature of ZnO present other visible bands due to intrinsic and extrinsic defects<sup>105</sup>. These surface defects of ZnO are chemically sensitive to several gases, making it suitable for sensing applications<sup>103, 106</sup>. In this connection, nanostructured materials (two examples are included in Figure 1.18(a)) introduce a higher surface-to-volume exposition, thus greater chemical sensitivity in ZnO nanostructures is expected<sup>104</sup>. Indeed, the fabrication and structural characterization of different ZnO nanostructures (nanoparticles, nanoribbons, nanowires, nanorods) by several fabrication methods have been extensively studied up to now<sup>103, 104</sup>.

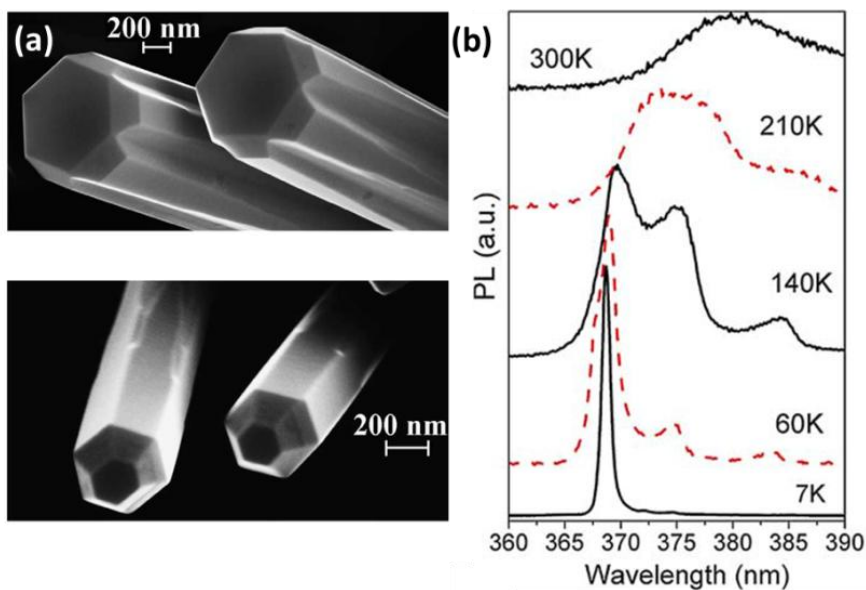


Figure 1.18. ZnO rods and photoluminescence spectra at different temperatures- (a) Representative scanning electron microscopy images of ZnO nanorods. (b) PL spectra at 7, 60, 140, 210 and 300 K as a function of the wavelength of ZnO nanorods<sup>107</sup>.

Variable-temperature photoluminescence measurements can provide information about the structural and optical properties of ZnO. On the one hand, the number of observed bound-exciton peaks in ZnO single crystal is higher than ZnO nanostructures. Moreover, low-temperature (4-10 K) photoluminescence measurements of different structures exhibit several bound peaks, donor-acceptor pair transitions and longitudinal optical phonon replicas, whereas in all ZnO samples (single crystals, films and nanostructures) if the temperature is increased to room temperature, only free-exciton emission is observed<sup>103</sup>. In Figure 1.19, an example of photoluminescence spectra at different temperatures of ZnO faceted rods is shown. In addition, as aforementioned, room temperature photoluminescence spectra reveal different peaks in the visible spectral region which have been attributed to the defect emission. Blue-green, green, yellow and orange-red defect emissions in ZnO structures have been reported. The origin of these defects are have been tried to identify by the combination of photoluminescence with other techniques, such as electron paramagnetic resonance (EPR) spectroscopy, positron annihilation spectroscopy (PAS) or X-ray photoelectron spectroscopy (XPS), but it remains unresolved. For instance, the identification of green emission, which is the most common, is not completely clear, it could stem from oxygen or Zn vacancy or interstitials and antisite oxygen, but it has been evidenced experimentally that the defect responsible are located at the surface. While, the yellow emission is ascribed to transitions involving interstitial oxygen and the responsible defect are not located at the surface. And the orange-red emissions were assigned to oxygen interstitial or oxygen-rich samples for different nanostructured analysed. However, in general, all of the defects emissions have been founded for both nanostructures and thin films<sup>103</sup>.

The two main strategies for the fabrication of ZnO nanostructures are: spontaneous growth and template based synthesis. In the case of the method

without templates, such as thermal evaporation, metal-organic vapour phase epitaxy, laser ablation, hydrothermal synthesis, metal catalysts like gold are often used for a aligned growth on a selective area<sup>103, 108</sup>. These seed layers used as substrates in the fabrication of ZnO influence in its structure. ZnO nanostructures grown by vapour deposition method depends basically on the temperatures of the source and the substrates, the distance between both, the heating rate the gas flow rate and the starting precursor<sup>109</sup>. Therefore, the growth parameters during the deposition related to crystalline quality affect the optical properties of nanostructured ZnO materials. Thus, the defects can be deleted by varying the fabrication conditions<sup>104</sup> or by post-fabrication treatment<sup>110</sup>. As examples, hydrogen plasma enhancing UV-to-defect emission intensity ratio for ZnO nanorods,<sup>109, 111</sup> and reduced defect yellow emission by annealing in hydrogen/argon mixture<sup>112</sup> has been reported. In Figure 1.19, the photoluminescence spectra obtained for columnar ZnO films grown by O<sub>2</sub> plasma deposition at different substrate temperatures. The position of peak at 378 nm, which was attributed to the recombination of free excitons and the others to phonon replicas, and the visible emissions vary with the experimental conditions during the deposition.

The fabrication of ZnO from an organic compound, zinc phthalocyanine (ZnPc), is addressed in the present thesis, as well as their optical properties and sensing applications.

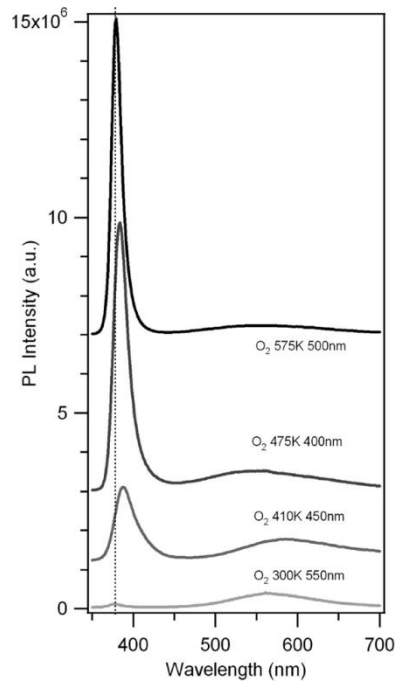


Figure 1.19. ZnO columnar films grown by PECVD at different temperatures photoluminescence spectra at room temperature - Films present two photoluminescence bands, a narrow one in the UV range (around 380 nm) and a broad one in the visible range (500-700 nm range).<sup>102, 104</sup>

## 1.6 Objectives

The main objective of this thesis is the development of novel multifunctional thin films and supported nanostructures by using remote plasma processes. Accordingly the project will address the following specific Scientific Objectives:

- To develop the synthetic methodology for the deposition of multifunctional thin films by plasma assisted vacuum deposition of solids precursors. The properties of the films will be determined by the nature of the precursor molecules and by the interaction of them with a remote plasma discharge during the deposition.

- To optimize the conformality of the remote plasma deposited thin films. The conformal deposition is a requisite for the application of the films in optical and electrical devices. For this, the deposition on different type of nanostructured substrates will be studied.

- To develop and optimize optical thin films by the remote plasma assisted deposition of adamantane. For this it will be critical to study the experimental parameters that determine the optical properties as UV-Vis transparency and the control of the refractive index.

- To study the wetting properties of the organic thin films surfaces as a function of the temperature.

- To study the deposition of thin films by combining the adamantane synthesis with a second precursor consisting in a highly luminescent dye. For this it will be necessary to control the refractive index of the composite films and the optimization of their luminescent properties.

- To study the amplified spontaneous emission properties of the luminescent films in order to select the best candidates for lasing emission. For this type of application it will be necessary to adjust very precisely the optical and luminescent properties of the films.

- To fabricate a 1D distributed feedback laser incorporating the optimized luminescent thin films and characterization of the lasing emission.

- To study the dielectrical properties of remote plasma deposited adamantane functional films and the optimization of their dielectric breakdown field. The films will be studied in humid and saline environments to obtain films compatible with the operation in such conditions.

- To study the electrical properties of remote plasma polymerized adamantane films coating graphene, supported organic nanowires and bridge structures formed by organic nanowires connecting metallic microelectrodes.

- To develop of a general template for the synthesis of supported metal and metal oxide nanowires by remote plasma processing of 1D supported nanowires.

- To fabrication ZnO supported nanostructured surfaces by remote plasma deposition and by remote plasma processing of 1D organic nanofibers and study their optical, luminescent and sensing properties.

## REFERENCES

1. Atkinson, H. V., Structural and Functional Materials. *Material Science and Engineering* **2002**, *II*.
2. Banerjee, S. T. A. K., *Functional materials preparation, processing and applications*. Elsevier: Amsterdam; Boston; Paris, 2012.
3. Zhong Lin Wang, Z. C. K., *Functional and Smart Materials Structural Evolution and Structure Analysis*. Plenum Publishing Corp: New York, 1998.
4. Barranco, A.; Biemann, M.; Widmer, R.; Groening, P., Plasma polymerization of rhodamine 6G thin films. *Advanced Engineering Materials* **2005**, *7*, 396-400.
5. Barranco, A.; Groening, P., Fluorescent plasma nanocomposite thin films containing nonaggregated rhodamine 6G laser dye molecules. *Langmuir* **2006**, *22*, 6719-6722.
6. Barranco, A.; Aparicio, F.; Yanguas-Gil, A.; Groening, P.; Cotrino, J.; Gonzalez-Elipse, A. R., Optically active thin films deposited by plasma polymerization of dye molecules. *Chemical Vapor Deposition* **2007**, *13*, 319-325.
7. Blaszczyk-Lezak, I.; Aparicio, F. J.; Borrás, A.; Barranco, A.; Alvarez-Herrero, A.; Fernandez-Rodriguez, M.; Gonzalez-Elipse, A. R., Optically Active Luminescent Perylene Thin Films Deposited by Plasma Polymerization. *Journal of Physical Chemistry C* **2009**, *113*, 431-438.
8. Aparicio, F. J.; Borrás, A.; Blaszczyk-Lezak, I.; Groning, P.; Alvarez-Herrero, A.; Fernandez-Rodriguez, M.; Gonzalez-Elipse, A. R.; Barranco, A., Luminescent and Optical Properties of Nanocomposite Thin Films Deposited by Remote Plasma Polymerization of Rhodamine 6G. *Plasma Processes and Polymers* **2009**, *6*, 17-26.
9. Aparicio, F. J.; Holgado, M.; Borrás, A.; Blaszczyk-Lezak, I.; Griol, A.; Barrios, C. A.; Casquel, R.; Sanza, F. J.; Sohlstrom, H.; Antelius, M.; Gonzalez-Elipse, A. R.; Barranco, A., Transparent Nanometric Organic Luminescent Films as UV-Active Components in Photonic Structures. *Advanced Materials* **2011**, *23*, 761-765.
10. Aparicio, F. J.; Blaszczyk-Lezak, I.; Sanchez-Valencia, J. R.; Alcaire, M.; Gonzalez, J. C.; Serra, C.; Gonzalez-Elipse, A. R.; Barranco, A., Plasma Deposition of Perylene-Adamantane Nanocomposite Thin Films for NO<sub>2</sub> Room-Temperature Optical Sensing. *Journal of Physical Chemistry C* **2012**, *116*, 8731-8740.
11. Aparicio, F. J.; Alcaire, M.; Borrás, A.; Gonzalez, J. C.; Lopez-Arbeloa, F.; Blaszczyk-Lezak, I.; Gonzalez-Elipse, A. R.; Barranco, A., Luminescent 3-hydroxyflavone nanocomposites with a tuneable refractive index for photonics

- and UV detection by plasma assisted vacuum deposition. *Journal of Materials Chemistry C* **2014**, *2*, 6561-6573.
12. Fridman, A., *Plasma Chemistry*. Cambridge University Press: New York, 2012.
  13. Langmuir, I., Oscillations in ionized gases. *Proceedings of the National Academy of Sciences of the United States of America* **1928**, *14*, 627-637.
  14. Grill, A., *Cold Plasma Materials Fabrication: From Fundamentals to Applications*. IEEE Press: Piscataway, 1993.
  15. Albella Martín, J. M., *Láminas delgadas y recubrimientos. Preparación, propiedades y aplicaciones*. Consejo Superior de Investigaciones Científicas Madrid, 2003.
  16. Denes, F. S.; Manolache, S., Macromolecular plasma-chemistry: an emerging field of polymer science. *Progress in Polymer Science* **2004**, *29*, 815-885.
  17. Foerch, R.; McIntyre, N. S.; Hunter, D. H., Modification of polymer surfaces by 2-step plasma sensitized reactions. *Journal of Polymer Science Part a-Polymer Chemistry* **1990**, *28*, 803-809.
  18. Foerch, R.; Hunter, D. H., Remote nitrogen plasma treatment of polymers-polyethylene, nylon 6,6, poly(ethylene vinyl alcohol), and poly(ethylene-terephthalate). *Journal of Polymer Science Part a-Polymer Chemistry* **1992**, *30*, 279-286.
  19. Biederman, H., *Plasma polymer films*. Imperial College Press: London, 2004.
  20. Friedrich, J., Mechanisms of Plasma Polymerization - Reviewed from a Chemical Point of View. *Plasma Processes and Polymers* **2011**, *8*, 783-802.
  21. Miller, S. L., A production of amino acids under possible primitive Earth conditions *Science* **1953**, *117*, 528-529.
  22. Miller, S. L.; Urey, H. C., Organic compound synthesis on the primitive Earth. *Science* **1959**, *130*, 245-251.
  23. Neiswend, D. D., Polymerization of Benzene in a Radiofrequency Discharge. *Advances in Chemistry Series* **1969**, 338.
  24. Yasuda, H., *Plasma polymerization*. Academic Press: Orlando, 1985.
  25. Yasuda, H., Glow-Discharge Polymerization. *Macromolecular Reviews Part D-Journal of Polymer Science* **1981**, *16*, 199-293.
  26. Westwood, A. R., Glow discharge polymerization. I. Rates and Mechanisms of polymer formation. *European Polymer Journal* **1971**, *7*, 363-&.
  27. Kobayash.H; Bell, A. T.; Shen, M., Foramation of an amorphous podwer during polymerization of ethylene in a radio-frequency discharge. *Journal of Applied Polymer Science* **1973**, *17*, 885-892.
  28. Kobayash.H; Bell, A. T.; Shen, M., Plasma polymerization of saturated and unsaturated-hydrocarbons. *Macromolecules* **1974**, *7*, 277-283.



29. Tibbitt, J. M.; Jensen, R.; Bell, A. T.; Shen, M., Model for kinetics of plasma polymerization. *Macromolecules* **1977**, *10*, 647-653.
30. Tibbitt, J. M.; Shen, M.; Bell, A. T., Structural characterization of plasma-polymerized hydrocarbons. *Journal of Macromolecular Science-Chemistry* **1976**, *A 10*, 1623-1648.
31. R. d'Agostino, P. F., F. Fracassi, *Plasma Processing of Polymers* Kluwer Academic: Dordrecht, 1996.
32. Hudis, M., Surface crosslinking of polyethylene using a hydrogen glow-discharge. *Journal of Applied Polymer Science* **1972**, *16*, 2397-&.
33. Jesch, K., Bloor, J. E. Kronick, P.L, Structure and physical properties of glow discharge polymers.I. Polymers from hydrocarbons. *Journal of Polymer Science Part a-1-Polymer Chemistry* **1966**, *4*, 1487-&.
34. Kronick, P. L. J., K. F.Bloor, J.E., Spectra of glow-discharge polymers from aromatic compounds. *Journal of Polymer Science Part a-1-Polymer Chemistry* **1969**, *7*, 767.
35. M.Tibbitt, J. M. B., A. T.Shen, Dielectric relaxations in plasma-polymerized hydrocarbons and fluorocarbons. *Journal of Macromolecular Science-Chemistry* **1976**, *A 10*, 519-533.
36. Friedrich, J.; Kuhn, G.; Mix, R.; Fritz, A.; Schonhals, A., Polymer surface modification with monofunctional groups of variable types and densities. *Journal of Adhesion Science and Technology* **2003**, *17*, 1591-1617.
37. J.Fredrich, G. K., R.Mix , I.Retzko, V.Gerstung, St.Weidner, R.D.Schulze,W.Unger In *Polyimides and other high temperature polymers:Synthesis, characterization, and applications*, Polyimides and other high temperature polymers:Synthesis, characterization, and applications, Utrech, 2003; K.L.Mittal, Ed. VSP: Utrech; pp 359-388.
38. Chowdhury, F. U. Z.; Bhuiyan, A. H., Dielectric properties of plasma-polymerized diphenyl thin films. *Thin Solid Films* **2000**, *370*, 78-84.
39. Stundzia, V.; Biederman, H.; Slavinska, D.; Nedbal, J.; Hlidek, P.; Poskus, A.; Mackus, P. K.; Howson, R. P., Dielectric relaxation in hard, plasma-polymerized C : H films. *Journal of Physics D-Applied Physics* **2000**, *33*, 719-724.
40. K. G.Thompson, L. F. M., Plasma polymerization of vinyl monomers.1. design,construction and operatin of indcutively coupled plasma generator and preliminary studies with 9 monomers. *Journal of Applied Polymer Science* **1972**, *16*, 2291-&.
41. Haupt, M.; Barz, J.; Oehr, C., Creation and recombination of free radicals in fluorocarbon plasma polymers: An electron spin resonance study. *Plasma Processes and Polymers* **2008**, *5*, 33-43.
42. Wrobel, A. M. K., J.Grebowicz, J.Kryszewski, M., Thermal-decomposition of plasma-polymerized organo-silicon thin-films. *Journal of Macromolecular Science-Chemistry* **1982**, *A17*, 433-452.

43. Kruger, S.; Schulze, R. D.; Brademann-Jock, K.; Swaraj, S.; Friedrich, J., Characterisation of plasma polymers by thermoluminescence. *Surface & Coatings Technology* **2006**, *201*, 543-552.
44. A.Dilks, A. K., S.Vanlaeken, A C-13-NMR investigation of plasma polymerized ethane, ethylene and acetylene. *Journal of Polymer Science Part a-Polymer Chemistry* **1981**, *19*, 2987-2996.
45. A.Kaplan, S. D., The structure of plasma-polymerized toluene-A solid-state C-13-NMR study of isotopically labeled polymers. *Journal of Polymer Science Part a-Polymer Chemistry* **1983**, *21*, 1819-1829.
46. J. Friedrich, I. R., G. Kuhn, W. Unger, A. Lippitz In *Metallized Plastics 7: Fundamentals and Applied Aspects*, Utrecht2001; Mittal, K. L., Ed. VSP: Utrecht.
47. Retzko, I.; Friedrich, J. F.; Lippitz, A.; Unger, W. E. S., Chemical analysis of plasma-polymerized films: The application of X-ray photoelectron spectroscopy (XPS), X-ray absorption spectroscopy (NEXAFS) and fourier transform infrared spectroscopy (FTIR). *Journal of Electron Spectroscopy and Related Phenomena* **2001**, *121*, 111-129.
48. Kuhn, G.; Retzko, I.; Lippitz, A.; Unger, W.; Friedrich, J., Homofunctionalized polymer surfaces formed by selective plasma processes. *Surface & Coatings Technology* **2001**, *142*, 494-500.
49. Hollahan, J. R., Rare-gas plasma polymerization of benzene at -196 degrees C. *Makromolekulare Chemie* **1972**, *154*, 303-&.
50. d'Agostino, R., *Plasma Deposition, Treatment, and Etching of Polymers*. Academic Press Inc.: San Diego (US), 1990.
51. Ostrikov, K. N., E. C.Meyyappan, M., Plasma nanoscience: from nano-solids in plasmas to nano-plasmas in solids. *Advances in Physics* **2013**, *62*, 113-224.
52. Wells, G. P.; Estrada-Raygoza, I. C.; Thamban, P. L. S.; Nelson, C. T.; Chung, C. W.; Overzet, L. J.; Goeckner, M. J., Understanding the Synthesis of Ethylene Glycol Pulsed Plasma Discharges. *Plasma Processes and Polymers* **2013**, *10*, 119-135.
53. Boscher, N. D.; Duday, D.; Heier, P.; Heinze, K.; Hilt, F.; Choquet, P., Atmospheric pressure plasma polymerisation of metalloporphyrins containing mesoporous membranes for gas sensing applications. *Surface & Coatings Technology* **2013**, *234*, 48-52.
54. Aparicio, F. J. L., G.Blaszczyk-Lezak, I.Barranco, A.Miguez, H., Conformal Growth of Organic Luminescent Planar Defects within Artificial Opals. *Chemistry of Materials* **2010**, *22*, 379-385.
55. Alcaire, M.; Sanchez-Valencia, J. R.; Aparicio, F. J.; Saghi, Z.; Gonzalez-Gonzalez, J. C.; Barranco, A.; Zian, Y. O.; Gonzalez-Eliphe, A. R.; Midgley, P.; Espinos, J. P.; Groening, P.; Borrás, A., Soft plasma processing of organic nanowires: a route for the fabrication of 1D organic heterostructures and

the template synthesis of inorganic 1D nanostructures. *Nanoscale* **2011**, *3*, 4554-4559.

56. Nowak, S.; Gröning, P.; Küttel, O. M.; Collaud, M.; Dietler, G., Electron cyclotron resonance plasma experiment for in situ surface modification, deposition, and analysis. *Journal of Vacuum Science & Technology A* **1992**, *10*, 3419-3425.

57. Yang, P. D.; Wirnsberger, G.; Huang, H. C.; Cordero, S. R.; McGehee, M. D.; Scott, B.; Deng, T.; Whitesides, G. M.; Chmelka, B. F.; Buratto, S. K.; Stucky, G. D., Mirrorless lasing from mesostructured waveguides patterned by soft lithography. *Science* **2000**, *287*, 465-467.

58. Vogel, R.; Meredith, P.; Kartini, I.; Harvey, M.; Riches, J. D.; Bishop, A.; Heckenberg, N.; Trau, M.; Rubinsztein-Dunlop, H., Mesostructured dye-doped titanium dioxide for micro-optoelectronic applications. *Chemphyschem* **2003**, *4*, 595-603.

59. del Monte, F.; Mackenzie, J. D.; Levy, D., Rhodamine fluorescent dimers adsorbed on the porous surface of silica gels. *Langmuir* **2000**, *16*, 7377-7382.

60. Aparicio Rebollo, F. J. Desarrollo de láminas luminiscentes por tecnología de plasma para su integración en sensores fotónicos. University of Seville, Seville, 2011.

61. Sasaki, D. Y.; Singh, S.; Cox, J. D.; Pohl, P. I., Fluorescence detection of nitrogen dioxide with perylene/PMMA thin films. *Sensors and Actuators B-Chemical* **2001**, *72*, 51-55.

62. Sengupta, P. K. K., M., Excited-state proton-transfer spectroscopy of 3-hydroxyflavone and quercetin. *Chemical Physics Letters* **1979**, *68*, 382-385.

63. Chou, P. M., D.Aartsma, T. J.Kasha, M., The proton transference laser-gain spectrum and amplification of spontaneous emission of 3-hydroxyflavone. *Journal of Physical Chemistry* **1984**, *88*, 4596-4599.

64. Strandjord, A. J. G. B., P. F., Proton-transfer kinetics of 3-hydroxyflavone-solvent effects. *Journal of Physical Chemistry* **1985**, *89*, 2355-2361.

65. Zayat, M.; Parejo, P. G.; Levy, D., Preventing UV-light damage of light sensitive materials using a highly protective UV-absorbing coating. *Chemical Society Reviews* **2007**, *36*, 1270-1281.

66. Zang, L.; Che, Y.; Moore, J. S., One-Dimensional Self-Assembly of Planar  $\pi$ -Conjugated Molecules: Adaptable Building Blocks for Organic Nanodevices. *Accounts of Chemical Research* **2008**, *41*, 1596-1608.

67. Briseno, A. L.; Mannsfeld, S. C. B.; Jenekhe, S. A.; Bao, Z.; Xia, Y. N., Introducing organic nanowire transistors. *Materials Today* **2008**, *11*, 38-47.

68. Liu, H. B.; Li, Y. L.; Zhu, D. B., Synthesis and properties of pi conjugated organic molecular one-dimensional nanomaterials. *International Journal of Nanotechnology* **2007**, *4*, 197-213.

69. Curtis, M. D.; Cao, J.; Kampf, J. W., Solid-state packing of conjugated oligomers: from pi-stacks to the herringbone structure. *Journal of the American Chemical Society* **2004**, *126*, 4318-4328.
70. Cornil, J.; Beljonne, D.; Calbert, J. P.; Bredas, J. L., Interchain interactions in organic pi-conjugated materials: Impact on electronic structure, optical response, and charge transport. *Advanced Materials* **2001**, *13*, 1053-1067.
71. Briseno, A. L.; Mannsfeld, S. C. B.; Reese, C.; Hancock, J. M.; Xiong, Y.; Jenekhe, S. A.; Bao, Z.; Xia, Y., Perylenediimide Nanowires and Their Use in Fabricating Field-Effect Transistors and Complementary Inverters. *Nano Letters* **2007**, *7*, 2847-2853.
72. Borrás, A.; Groning, O.; Aguirre, M.; Gramm, F.; Groning, P., One-Step Dry Method for the Synthesis of Supported Single-Crystalline Organic Nanowires Formed by pi-Conjugated Molecules. *Langmuir* **2010**, *26*, 5763-5771.
73. Wang, Z. C.; Medforth, C. J.; Shelnutt, J. A., Porphyrin nanotubes by ionic self-assembly. *Journal of the American Chemical Society* **2004**, *126*, 15954-15955.
74. Schwab, A. D.; Smith, D. E.; Rich, C. S.; Young, E. R.; Smith, W. F.; de Paula, J. C., Porphyrin nanorods. *Journal of Physical Chemistry B* **2003**, *107*, 11339-11345.
75. Sostaric, J. Z.; Pandian, R. P.; Weavers, L. K.; Kuppasamy, P., Formation of lithium phthalocyanine nanotubes by size reduction using low- and high-frequency ultrasound. *Chemistry of Materials* **2006**, *18*, 4183-4189.
76. Kojima, T.; Harada, R.; Nakanishi, T.; Kaneko, K.; Fukuzumi, S., Porphyrin nanotubes based on self-assembly of Mo(V)-dodecaphenylporphyrin complexes and inclusion of Mo-oxo clusters: Synthesis and characterization by X-ray crystallography and transmission electron microscopy. *Chemistry of Materials* **2007**, *19*, 51-58.
77. Karthaus, O.; Nagata, S.; Nishide, J.; Sasabe, H., Control of crystal morphology of aromatic electron donors and acceptors for organic electronics. *Japanese Journal of Applied Physics* **2008**, *47*, 1245-1250.
78. Zhang, X. P.; Sun, B. Q., Organic crystal fibers aligned into oriented bundles with polarized emission. *Journal of Physical Chemistry B* **2007**, *111*, 10881-10885.
79. Yan, P.; Chowdhury, A.; Holman, M. W.; Adams, D. M., Self-organized perylene diimide nanofibers. *Journal of Physical Chemistry B* **2005**, *109*, 724-730.
80. Su, W.; Zhang, Y. X.; Zhao, C. T.; Li, X. Y.; Jiang, J. Z., Self-assembled organic nanostructures: Effect of substituents on the morphology. *Chemphyschem* **2007**, *8*, 1857-1862.

81. Zhao, L.; Yang, W.; Ma, Y.; Yao, J.; Li, Y.; Liu, H., Perylene nanotubes fabricated by the template method. *Chemical Communications* **2003**, 2442-2443.
82. Bai, R.; Ouyang, M.; Zhou, R. J.; Shi, M. M.; Wang, M.; Chen, H. Z., Well-defined nanoarrays from an n-type organic perylene-diimide derivative for photoconductive devices. *Nanotechnology* **2008**, *19*, 6.
83. Kriha, O.; Gring, P.; Milbradt, M.; Azgarwal, S.; Steinhart, M.; Wehrspohn, R.; Wendorff, J. H.; Greiner, A., Polymer tubes with longitudinal composition gradient by face-to-face wetting. *Chemistry of Materials* **2008**, *20*, 1076-1081.
84. Cho, S. I.; Lee, S. B., Fast Electrochemistry of Conductive Polymer Nanotubes: Synthesis, Mechanism, and Application. *Accounts of Chemical Research* **2008**, *41*, 699-707.
85. Tang, Q.; Li, H.; Liu, Y.; Hu, W., High-Performance Air-Stable n-Type Transistors with an Asymmetrical Device Configuration Based on Organic Single-Crystalline Submicrometer/Nanometer Ribbons. *Journal of the American Chemical Society* **2006**, *128*, 14634-14639.
86. Rakow, N. A.; Suslick, K. S., A colorimetric sensor array for odour visualization. *Nature* **2000**, *406*, 710-713.
87. Tang, Q.; Li, H.; Song, Y.; Xu, W.; Hu, W.; Jiang, L.; Liu, Y.; Wang, X.; Zhu, D., In Situ Patterning of Organic Single-Crystalline Nanoribbons on a SiO<sub>2</sub> Surface for the Fabrication of Various Architectures and High-Quality Transistors. *Advanced Materials* **2006**, *18*, 3010-3014.
88. Tong, W. Y.; Djurišić, A. B.; Xie, M. H.; Ng, A. C. M.; Cheung, K. Y.; Chan, W. K.; Leung, Y. H.; Lin, H. W.; Gwo, S., Metal Phthalocyanine Nanoribbons and Nanowires. *The Journal of Physical Chemistry B* **2006**, *110*, 17406-17413.
89. Xiao, K.; Tao, J.; Pan, Z.; Poretzky, A. A.; Ivanov, I. N.; Pennycook, S. J.; Geohegan, D. B., Single-Crystal Organic Nanowires of Copper-Tetracyanoquinodimethane: Synthesis, Patterning, Characterization, and Device Applications. *Angewandte Chemie* **2007**, *119*, 2704-2708.
90. Fan, Z. Y.; Mo, X. L.; Chen, G. R.; Lu, J. G., Synthesis, morphology and electrical characterization of Ag-TCNQ-from thin film to nanowire. *Reviews on Advanced Materials Science* **2003**, *5*, 72-75.
91. Mbenkum, B. N.; Barrena, E.; Kelsch, M.; Dosch, H., Selective Growth of Organic 1-D Structures on Au Nanoparticle Arrays. *Nano Letters* **2006**, *6*, 2852-2855.
92. Barrena, E.; Zhang, X. N.; Mbenkum, B. N.; Lohmueller, T.; Krauss, T. N.; Kelsch, M.; van Aken, P. A.; Spatz, J. P.; Dosch, H., Self-Assembly of Phthalocyanine Nanotubes by Vapor-Phase Transport. *Chemphyschem* **2008**, *9*, 1114-1116.

93. Borrás, A.; Aguirre, M.; Groening, O.; Lopez-Cartes, C.; Groening, P., Synthesis of Supported Single-Crystalline Organic Nanowires by Physical Vapor Deposition. *Chemistry of Materials* **2008**, *20*, 7371-7373.
94. Borrás, A.; Gröning, O.; Köble, J.; Gröning, P., Connecting Organic Nanowires. *Advanced Materials* **2009**, *21*, 4816-4819.
95. Ng, A. M.-C.; Djurišić, A. B.; Tam, K.-H.; Kwok, W.-M.; Chan, W.-K.; Tam, W. Y.; Phillips, D. L.; Cheah, K.-W., Organic Nanoclusters on Inorganic Nanostructures for Tailoring the Emission Properties of Organic Materials. *Advanced Functional Materials* **2008**, *18*, 566-574.
96. Borrás, A.; Gröning, O.; Köble, J.; Gröning, P., Connecting Organic Nanowires. *Advanced Materials* **2009**, *21*, 4816-+.
97. Biemann, M.; Schwaller, P.; Ruffieux, P.; Gröning, O.; Schlapbach, L.; Gröning, P., AgO investigated by photoelectron spectroscopy: Evidence for mixed valence. *Physical Review B* **2002**, *65*, 235431.
98. Borrás, A.; Barranco, A.; Espinos, J. P.; Cotrino, J.; Holgado, J. P.; Gonzalez-Elipe, A. R., Factors that contribute to the growth of Ag@TiO<sub>2</sub> nanofibers by plasma deposition. *Plasma Processes and Polymers* **2007**, *4*, 515-527.
99. Borrás, A.; Barranco, A.; Yubero, F.; Gonzalez-Elipe, A. R., Supported Ag-TiO<sub>2</sub> core-shell nanofibres formed at low temperature by plasma deposition. *Nanotechnology* **2006**, *17*, 3518-3522.
100. Borrás, A.; Gröning, P.; Sanchez-Valencia, J. R.; Barranco, A.; Espinos, J. P.; Gonzalez-Elipe, A. R., Air- and Light-Stable Superhydrophobic Colored Surfaces Based on Supported Organic Nanowires. *Langmuir* **2010**, *26*, 1487-1492.
101. Macias-Montero, M.; Filippin, A. N.; Saggi, Z.; Aparicio, F. J.; Barranco, A.; Espinos, J. P.; Frutos, F.; Gonzalez-Elipe, A. R.; Borrás, A., Vertically Aligned Hybrid Core/Shell Semiconductor Nanowires for Photonics Applications. *Advanced Functional Materials* **2013**, *23*, 5981-5989.
102. Macias Montero, M. J. New plasma-based synthesis procedures and applications of 1D-nanostructures. University of Seville, Seville, 2013.
103. Djurisić, A. B.; Leung, Y. H., Optical properties of ZnO nanostructures. *Small* **2006**, *2*, 944-961.
104. Romero-Gómez, P.; Toudert, J.; Sánchez-Valencia, J. R.; Borrás, A.; Barranco, A.; Gonzalez-Elipe, A. n. R., Tunable Nanostructure and Photoluminescence of Columnar ZnO Films Grown by Plasma Deposition. *The Journal of Physical Chemistry C* **2010**, *114*, 20932-20940.
105. Djurisić, A. B.; Leung, Y. H.; Tam, K. H.; Ding, L.; Ge, W. K.; Chen, H. Y.; Gwo, S., Green, yellow, and orange defect emission from ZnO nanostructures: Influence of excitation wavelength. *Applied Physics Letters* **2006**, *88*, 3.

106. Ahn, M.-W.; Park, K.-S.; Heo, J.-H.; Park, J.-G.; Kim, D.-W.; Choi, K. J.; Lee, J.-H.; Hong, S.-H., Gas sensing properties of defect-controlled ZnO-nanowire gas sensor. *Applied Physics Letters* **2008**, *93*, -.
107. Kwok, W. M.; Djurišić, A. B.; Leung, Y. H.; Chan, W. K.; Phillips, D. L.; Chen, H. Y.; Wu, C. L.; Gwo, S.; Xie, M. H., Study of excitonic emission in highly faceted ZnO rods. *Chemical Physics Letters* **2005**, *412*, 141-144.
108. Huang, M. H.; Mao, S.; Feick, H.; Yan, H. Q.; Wu, Y. Y.; Kind, H.; Weber, E.; Russo, R.; Yang, P. D., Room-temperature ultraviolet nanowire nanolasers. *Science* **2001**, *292*, 1897-1899.
109. Ye, C.; Fang, X.; Hao, Y.; Teng, X.; Zhang, L., Zinc Oxide Nanostructures: Morphology Derivation and Evolution. *The Journal of Physical Chemistry B* **2005**, *109*, 19758-19765.
110. Djurišić, A. B.; Choy, W. C. H.; Roy, V. A. L.; Leung, Y. H.; Kwong, C. Y.; Cheah, K. W.; Gundu Rao, T. K.; Chan, W. K.; Fei Lui, H.; Surya, C., Photoluminescence and Electron Paramagnetic Resonance of ZnO Tetrapod Structures. *Advanced Functional Materials* **2004**, *14*, 856-864.
111. Lin, C.-C.; Chen, H.-P.; Liao, H.-C.; Chen, S.-Y., Enhanced luminescent and electrical properties of hydrogen-plasma ZnO nanorods grown on wafer-scale flexible substrates. *Applied Physics Letters* **2005**, *86*, -.
112. Greene, L. E.; Law, M.; Goldberger, J.; Kim, F.; Johnson, J. C.; Zhang, Y.; Saykally, R. J.; Yang, P., Low-Temperature Wafer-Scale Production of ZnO Nanowire Arrays. *Angewandte Chemie International Edition* **2003**, *42*, 3031-3034.







## **2** Resumen en español

## 2.1 Introduction

La presente tesis se ha desarrollado en el grupo de investigación Nanotecnología de Superficies del Instituto de Ciencia de Materiales de Sevilla. En ella se estudian nuevos materiales obtenidos mediante una técnica de síntesis de láminas delgadas orgánicas funcionales basada en el empleo de plasmas remotos de microondas, se desarrollan nuevos métodos de nanoestructuración de estos materiales.

Los materiales estudiados en esta tesis presentan diversas propiedades. Así, a lo largo de la memoria se presentan láminas transparentes, dieléctricas, con propiedades particulares de mojado y retardadoras en la congelación, luminiscentes, con emisión láser y sensoras a gases, entre otras propiedades.

Empleando esta técnica desarrollada en nuestro laboratorio en los últimos años, se han fabricado nuevas láminas orgánicas, constituidas por una matriz polimérica de alto grado de entrecruzamiento, que incorpora de forma controlada una determinada cantidad de moléculas de colorante embebidas en la matriz. El proceso combina una descarga de plasma con la deposición en vacío de monómeros de sólidos orgánicos sobre sustratos situados en configuración remota respecto del plasma. La Figura 2.1 muestra un esquema del reactor de síntesis. La descarga de plasma fragmenta las moléculas precursoras. De manera controlada mediante el ajuste simultáneo y controlado de diferentes parámetros de deposición, es decir, MW de potencia, la presión total, la velocidad de sublimación y la disposición geométrica utilizada para la deposición se obtiene una fragmentación parcial de dichas moléculas. La distancia entre el plasma y la película en crecimiento ( $z$  en la Figura 2.1) es uno de los principales parámetros experimentales ajustables del proceso.<sup>1-4</sup> Esta distancia limita la interacción plasma-precursor y ofrece versatilidad al proceso de deposición puesto que regula gradualmente las propiedades de la película. El método de síntesis

proporciona un a amplia gama de películas sólo modificando la distancia  $z$ , desde polímeros de plasma con un alto grado de entrecruzamiento sin la retención del monómero original (deposición en la descarga de plasma) hasta laminas que contienen una cantidad de moléculas activas controlable (deposición en remoto). En el límite, si la distancia  $z$  es lo suficientemente grande, el proceso de síntesis se asemeja a una deposición en vacío sin plasma. El control de otros parámetros experimentales como la tasa de crecimiento, la presión o la potencia de la fuente de plasma microondas influyen de forma equivalente a la distancia sobre el método en algunos casos.

Además del método de deposición asistido por plasma mencionado, en esta tesis se explora el uso de tratamientos con plasma controlados de baja intensidad se ha aplicado también a la fabricación de nanoestructuras orgánicas híbridas. Se ha establecido este protocolo de síntesis como obtención de sustratos soporte nanoestructurados para el crecimiento de materiales nanoestructurados orgánicos mediante la técnica de deposición por plasma remoto. La nanoestructuración de materiales es un tema de actualidad debido a las nuevas propiedades que adquieren los materiales al confinar sus dimensiones en la nanoescala. Dentro de la amplia variedad de nanoestructuras, se presenta la síntesis de materiales 1D, es decir los que presentan solo una de sus dimensiones por encima de 100 nm.

Por último, se ha aplicado también el uso de postratamientos de plasma a láminas delgadas y nanoestructuras 1D orgánicas por el método de deposición de vacío (PVD) que modifican la estructura en la nanoescala y la química del material mediante el mismo montaje experimental.

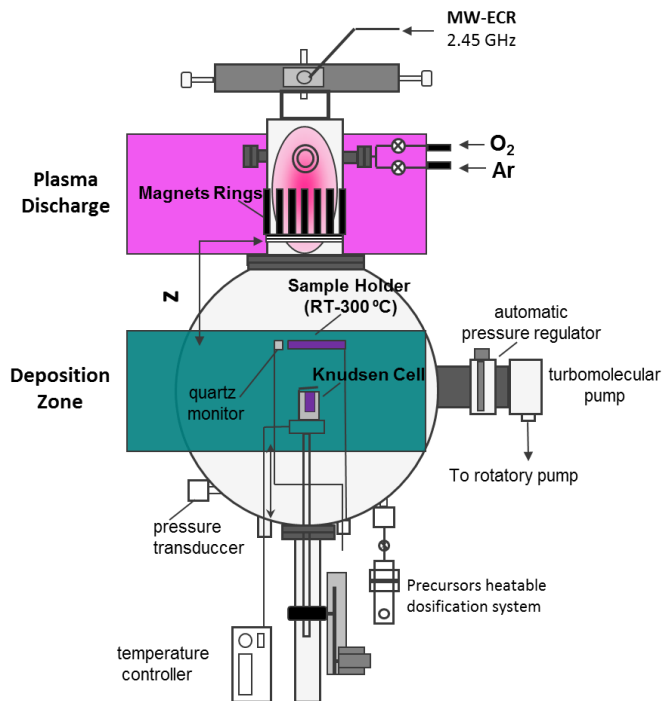


Figura 2.1. Reactor de preparación de muestras por deposición de vapor a vacío asistida por plasma (RPAVD) – Esquema de los principales componentes del reactor RPAVD utilizado en esta tesis para la fabricación de láminas delgadas orgánicas y nanoestructuras.

## 2.2 Láminas delgadas orgánicas conformales para aplicaciones en electrónica molecular

Los nanomateriales basados en grafeno y la electrónica molecular son temas de extrema importancia en la nanotecnología actual debido a las posibilidades que ofrecen en el desarrollo de nanodispositivos. Para alcanzar los objetivos de esta revolución tecnológica, estas nuevas nanoestructuras conductoras y semiconductoras tienen que combinarse con elementos dieléctricos mediante técnicas de última generación con el fin de producir

## **2.5 Tratamientos con plasma débil de nanohilos orgánicos: una vía para la fabricación de heteroestructuras orgánicas 1D y la síntesis de patrones de diseño de nanoestructuras inorgánicas 1D**

El estudio de nanoestructuras 1D fabricadas a partir de pequeñas moléculas orgánicas ha despertado un gran interés durante los últimos años debido a su aplicación en fotónica, fotovoltaica, fotocatalisis, microelectrónica y nanosensores. Este campo emergente de nanohilos orgánicos (ONWs) se ha ido estableciendo gracias al esfuerzo realizado durante los últimos años tanto en la fabricación como en el análisis de sus propiedades.<sup>28-38</sup> En paralelo con su homólogo inorgánico, la fabricación de nanocables orgánicos heteroestructurados está ganando cada vez más atractivo debido a su uso en los ámbitos de las aplicaciones mencionadas anteriormente, así como en el estudio de sistemas modelo para heterouniones n-p 1D.<sup>39</sup>

Este trabajo presenta una ruta sin precedentes para la síntesis de nanohilos orgánicos heteroestructurados. El método consiste en la combinación de dos procesos de vacío establecidos: la síntesis de nanohilos orgánicos monocristalinos (ONWs) por deposición física de vapor (PVD)<sup>5-7, 40, 41</sup> y el desbastado mediante por plasma de oxígeno.<sup>42, 43</sup> Dos ejemplos que demuestran las posibilidades de esta metodología se presentan en este apartado. Por un lado, se presenta la fabricación de dos tipos diferentes de nanoestructuras orgánicas mediante el control de la intensidad del tratamiento de plasma: heterostructured nanohilos (NWs) jerárquicos y nanohilos (NWs) híbridos metal-orgánicos. Por otra parte, atendiendo a los estudios previos mediante plasma débil de aire sobre el procesado de nanocristales coloidales para la eliminación de los ligandos orgánicos conservando las propiedades dependientes del tamaño de nanocristal,<sup>44</sup> exponemos en este trabajo la descripción de los primeros resultados de un método modelo para la síntesis de nanoestructuras 1D

inorgánicos mediante el procesamiento de nanohilos orgánicos.

### 2.5.1 Experimental

El método de síntesis de heteroestructuras orgánicas hace utiliza un reactor de plasma frío cuyo diseño ha sido descrito en la Sección Introducción, concretamente un plasma remoto de microondas (MW) de resonancia ciclotrónica (ECR) que permite tratamientos de las nanoestructuras orgánicas a potencias más bajas y el control sobre los parámetros experimentales críticos del proceso (distancia a la descarga de plasma, presión del gas, aplicación de voltaje al portamuestras, etc.).

La fabricación de loss diferentes tipos de nanoestructuras orgánicas, heteroestructuras NWs jerárquicas y NWs híbridos metal-orgánicos, y los tratamientos de plasma débil se producen en el mismo reactor remoto de deposición al vacío asistido por plasma (RPAVD). El proceso de fabricación en todos los casos se realiza en tres etapas (Figura 2.12): i) la síntesis de NWs orgánicos o metal-orgánicos por PVD, ii) formación de nuevos centros de nucleación mediante tratamientos de plasma de baja intensidad, iii) la síntesis de NWs secundarias a partir de estos nuevos núcleos.

#### 2.5.1.1 Formación de nanohilos orgánicos mediante PVD

Los precursores orgánicos utilizados en la fabricación de hetroestructuras han sido: perileno-diimida (2,9-dimetil-anthra [2,1-def: 6,5,10-d'e'f ']) diisoquinoline 1,3, 8,10-tetrona (Me-PTCDI de Sensient Imaging Technologies.), octaethyl porfirina de paladio (PdOEP de Frontier Sci.), y ftalocianina de cobalto (CoPc de Aldrich).

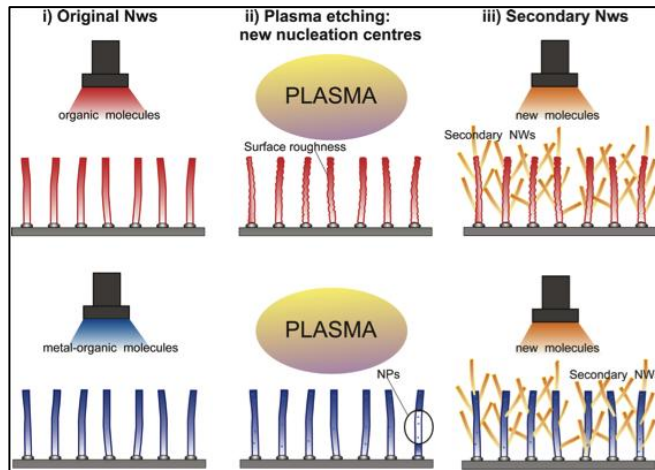


Figura 2.12. Mecanismo de formación heteroestructuras orgánicas 1D – Diferentes etapas del método de fabricación de dos tipos de nanoestructuras orgánicas heteroestructuradas desarrollado a partir de la combinación de los procesos de PVD y de tratamientos con plasma de oxígeno. Los modelos de crecimiento de NWs jerárquicas (a) y metal-orgánicas (b) se representan en esta imagen mediante tres etapas de formación.

La sublimación de las moléculas para la deposición de los nanohilos se realizó mediante una celda de  $10 \text{ cm}^3$  OLED Knudsen (Lesker) colocada en la cámara de alto vacío (sin plasma). El sistema se bombeó hasta la presión base de  $5 \cdot 10^{-6}$  mbar antes de la deposición. La distancia entre el sustrato y la fuente de sublimación fue de 8 cm. Durante los experimentos, el argón se dosificó usando un controlador de flujo de masa calibrado. La presión en el sistema durante la deposición se fijó en 0.020 mbar. La tasa de crecimiento fue controlada por una microbalanza de cristal de cuarzo situada en el mismo plano que los sustratos. El crecimiento de los nanohilos heteroestructurados se ejecutó combinando dos células Knudsen diferentes. Las tasas de deposición fueron entre  $0.30$  y  $0.50 \text{ \AA} \cdot \text{s}^{-1}$  considerando una densidad en la balanza de  $0.5 \text{ g} \cdot \text{cm}^{-3}$ . Las ONWs se fabricaron simultáneamente en diferentes sustratos: ITO, Si (100), sílice fundida y rejillas TEM de oro previamente recubiertas con nanopartículas de plata por



pulverización catódica (DC-sputtering) y películas delgadas  $\text{TiO}_2$  depositadas mediante técnicas de vacío. La temperatura de los sustratos temperatura (TS) para la formación ONWs depende de la molécula orgánica: a) para el Me-PTCDI la temperatura del sustrato óptima TS fue de  $175 \pm 5^\circ \text{C}$ ; b) para el TS PdOEP fue  $140 \pm 5^\circ \text{C}$  y c) para el TS COPC fue de  $260 \pm 5^\circ \text{C}$ .

### 2.5.1.2 Pos-tratamientos con plasma de baja intensidad

El reactor de deposición está equipado con un sistema de microondas a distancia de plasma (2,45 GHz) que permite el procesamiento de plasma de baja intensidad in situ. Todos los experimentos recogidos en este trabajo se realizaron in situ bajo las siguientes condiciones: 150 W en la fuente de microondas, la composición del gas de plasma fue de 80% de oxígeno - 20% de argón, la presión total en la cámara de 0,020 mbar, y la configuración remota, es decir, sustratos se situaron alejados del plasma, concretamente a los 5 cm.

### 2.5.1.3 Nanohilos orgánicos secundarios fabricados por PVD

Los tratamientos de plasma inducen cambios en la rugosidad de la superficie de ONWs a lo largo de su estructura, incluso agregación de átomos de metal para las ONWs crecidas a partir de moléculas que contienen metales. Dichas modificaciones de la superficie a su vez forman nuevos centros de nucleación a lo largo de la estructura de las NWs. Por tanto, las nanoestructuras secundarias 1D fabricadas mediante PVD crecen a partir de estos centros de nucleación, siguiendo el mismo procedimiento que las ONWs primarias.

## 2.5.2 Caracterización de heteroestructuras orgánicas 1D

La caracterización SEM se realizó en un Hitachi S-4800 mientras que la caracterización TEM y tomografía de electrones HAADF-STEM se realizó en un microscopio electrónico de transmisión de campo de emisión FEI Tecnai F20 operando a 200 kV. Los datos se recopilaron inclinando la muestra sobre un solo

eje de  $-64^\circ$  a  $+62^\circ$  con un incremento de  $2^\circ$ , utilizando un soporte de tomografía Fischione de ultra alta inclinación, y la adquisición de las imágenes con el paquete de software FEI Xplore3D. A continuación, la serie de inclinación se exportó al FEI software Inspect3D para el alineamiento de correlación cruzada y la reconstrucción tomográfica utilizando la rutina iterativa SIRT. Posteriormente se obtuvo una vista de una sección utilizando software Amira. Las ONWs fueron analizadas por TEM directamente crecidas en las rejillas de TEM o tras haberse retirado de los sustratos mediante el raspado, dispersión en etanol y posterior "pesca" en una rejilla de carbono *holy*. Las imágenes de microscopía de fluorescencia se obtuvieron con un microscopio de fluorescencia Olympus BX51. Los espectros de fluorescencia se registraron en un espectrofluorómetro Jobin Yvon Fluorolog3 utilizando la configuración de la *frot face* y rapertura de 4 y 2 nm para los monocromadores de excitación y emisión, respectivamente.

### 2.5.3 Resultados y discusión

#### 2.5.3.1 Heteroestructuras jerárquicas por plasma de oxígeno

En previas publicaciones se ha reportado un método general para el crecimiento de ONWs y *nanobelts* cuadrados a partir de la sublimación controlada de  $\pi$ -moléculas sobre sustratos con una determinada morfología.<sup>5-7, 40</sup>  
<sup>41</sup> Este método proporciona una ruta directa para la fabricación de alta densidad de nanohilos orgánicos de monocristales de metalo-porfirinas (M-OEP), ftalocianinas (MPC) y perilenos (MePTCDI) soportado sobre sustratos tales como  $\text{TiO}_2$ ,  $\text{ZnO}$ , ITO y  $\text{SiO}_2$ , nanopartículas metálicas, películas delgadas metálicas, etc.

La innovación en la fabricación de las nuevas heteroestructuras es el post-tratamiento por plasma de microondas remoto de oxígeno de los nanohilos monocristalinos crecidos previamente. El efecto de la oxidación controlada de

los nanocables depende de: i) la composición del gas de plasma y los parámetros del plasma; ii) la estructura química de las moléculas ya sea que contiene un átomo de metal (por ejemplo, CoPC, PdOEP) o es puramente orgánico (por ejemplo, OEP, Pc o perileno); iii) la temperatura durante el tratamiento y su duración.

La Figura 2.13 muestra los cambios inducidos por un plasma microondas de oxígeno en NWs de perileno después de un tratamiento de 30 minutos a 110 °C. El desbastado inducido por el plasma en las NWs produce un incremento importante en la rugosidad de la superficie y una disminución de su espesor. La superficie original cuadrada (imagen no mostrada) aparece ahora muy desigual con rasgos triangulares perpendiculares a la dirección de crecimiento del NW.

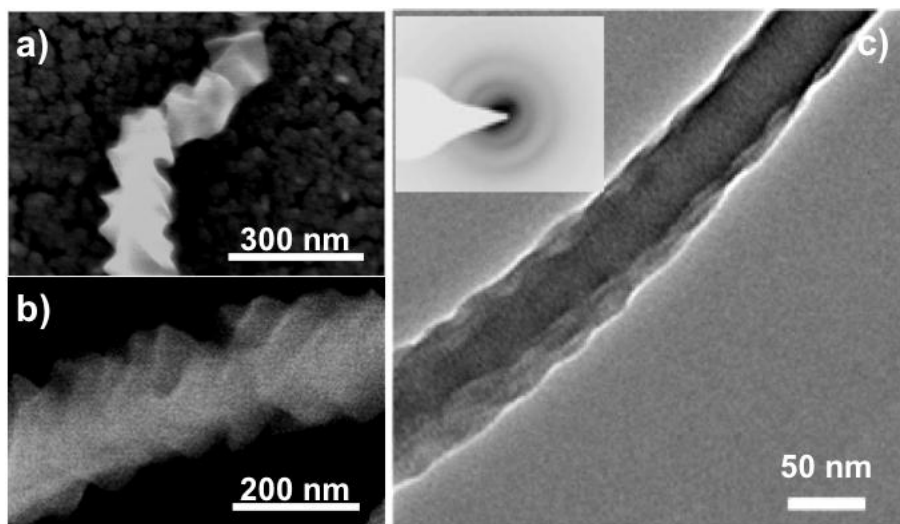


Figura 2.13. NWs tratadas con plasma a temperaturas superiores a RT – Micrografías SEM (a-b) and TEM (c) de nanohilos individuales de of iMePTCDI después de un tratamiento de plasm a 110°C during 30 minutos. El cuadro en (c) muestra el SAED de la NW.

Aunque la inestabilidad de las nanoestructuras orgánicas bajo el haz de electrones dificulta su plena caracterización por difracción de electrones mediante área seleccionada (SAED), el recuadro en la Figura 2.13 puede indicar que las NWs mantienen la estructura cristalina original.<sup>5-7, 40</sup> La formación de la superficie triangular se mejora imponiendo temperaturas a la muestraa cercanas a la temperatura de sublimación de las moléculas. Para temperaturas inferiores, los cambios en la rugosidad de la superficie son visibles únicamente tras tratamientos muy prolongados (hasta 60 minutos). Esta rugosidad controlada de las superficies de las NWs puede ser muy ventajosa en diferentes aplicaciones. Por ejemplo, un incremento de la superficie de la ONWs puede afectar positivamente a sus propiedades sensoras properties.<sup>45</sup>

Por otra parte, el desbastado mediante plasma controlado de las ONWs induce la formación de nuevos centros de nucleación a lo largo de su estructura que permite el crecimiento de estructuras secundarias 1D. De hecho, nuestros resultados anteriores sobre la formación de ONWs por deposición física de vapor demostraron que estas estructuras siempre se desarrollan a partir de centros de nucleación bien definidas, como por ejemplo la superficie de NPs de metal, granos de óxido de bien definidas, etc.<sup>30</sup> La Figura 2.14 muestra el crecimiento de ONWs secundarias y *nanobelts* de diferentes moléculas que ramifican de NWs de perileno primarios con su superficie ligeramente modificada por plasma de oxígeno a temperatura ambiente. Por lo tanto, nanoestructuras jerárquicas como perileno-perileno (Figura 2.14 (a)) o OEP-OEP NWs conexiones pueden ser fácilmente fabricados a partir de tratamientos de plasma durante varios segundos para inducir la formación de algunos núcleos y luego seguir la sublimación moléculas. Del mismo modo, heteroestructuras 1D basadas en perileno-PdOEP NWs pueden ser sintetizados mediante la aplicación de un plasma débil sobre las NWS fabricadas inicialmente de perileno, seguido por la sublimación de PdOEP (Figura 2.14 (b) - (d)).

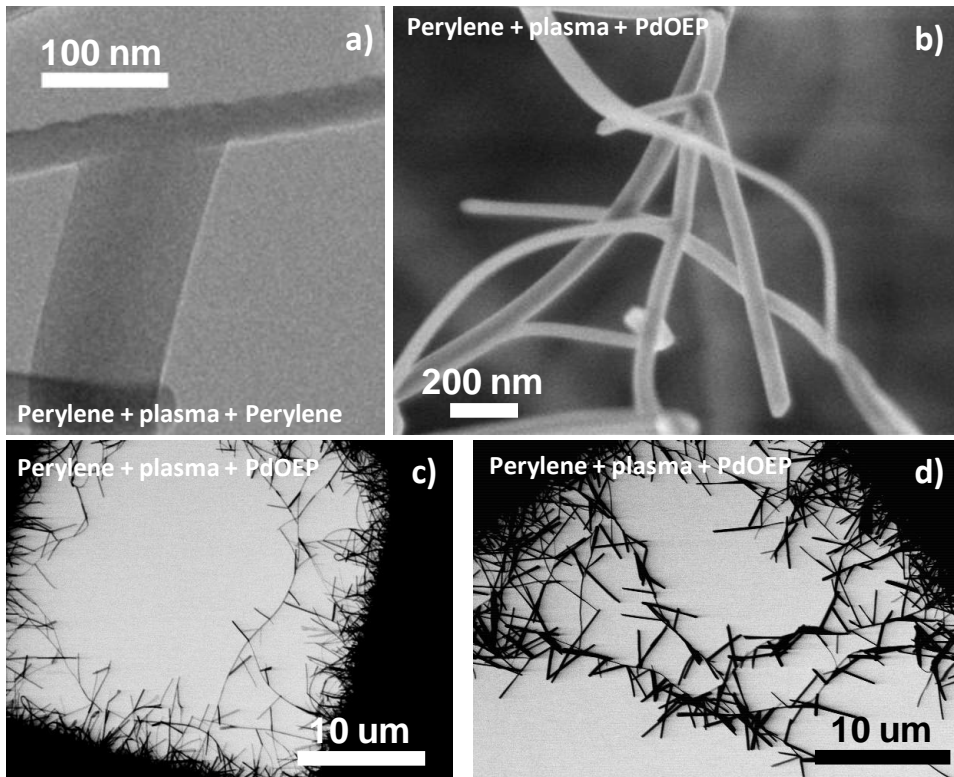


Figura 2.14. Nanoestructuras jerárquicas – (a) Micrografía TEM de una *nanobelt* de perileno creciendo a partir de un nanohilo de perileno. Micrografías SEM de alta magnificación (b) y (c-d) STEM baja magnificación presentan el crecimiento jerárquico de PdOEP-NWs / perileno-NWs.

En ambos casos, el número de NWs secundarias está relacionado con la rugosidad inducida que depende de la duración y la temperatura durante el tratamiento con plasma. La fabricación de alta densidad de este tipo de heteroestructuras soportadas en sustratos presumimos que ocasionará importantes implicaciones en aplicaciones de recolección de luz y nanosensores (por ejemplo, para obtener un rendimiento multisensorial combinando diferentes moléculas en la formación de las NWs jerárquicas). Por último, señalar que las propiedades ópticas de las NWs primarias de perileno,

Pc o OEP no se alteran por los tratamientos con plasma de baja intensidad y a bajas temperaturas. Se ha estudiado un sistema formado por NWs de perileno/PdOEP mediante microscopía de fluorescencia y espectros de emisión bajo diferentes longitudes de onda de excitación que demuestran la afirmación. Los espectros confirman que los dos componentes, porfirina de paladio y perileno, emiten independientemente cuando son excitados a las longitudes de onda de 350 nm y 490 nm respectivamente. Este resultado sostiene que para componentes sensibles a distintos gases (p.ej., perileno a el NO<sub>2</sub> y porfirina al oxígeno)<sup>2, 45, 46</sup> el sistema actuaría como un multisensor óptico siguiendo los correspondientes aumento / disminución de intensidades de las diferentes emisiones de luz.

### **2.5.3.2 NWs híbridas metal-orgánicas formadas por plasma débil**

Otra posibilidad que plantea esta metodología es la formación de nanohilos de metal-orgánicos híbridos. El origen del material inorgánico es la formación de nanopartículas de metales mediante la agregación de los átomos de metal resultantes de la descomposición debida al plasma de las capas externas de la estructura molecular metal-orgánica primaria. Durante el tratamiento con plasma de oxígeno, la parte orgánica de las moléculas reacciona con las especies excitadas del oxígeno. Los fragmentos y productos volátiles son evacuados por el sistema de vacío.<sup>42, 43</sup> Como consecuencia, los átomos de metal permanecen en las NWs formando nanopartículas cuyo tamaño y densidad depende de las condiciones experimentales y de los átomos metálicos. Los puntos brillantes en las micrografías SEM de la Figura 2.15 confirman la formación de nanopartículas de metal en la superficie de las ONWs tratadas con un plasma de oxígeno a temperatura ambiente.

Por otra parte, la reconstrucción 3D a partir de electrones dispersados a alto ángulo en un detector anular de campo oscuro a alto ángulo (HAADF-

STEM)<sup>47-49</sup> nos ha permitido describir completamente la microestructura interna de estas nanoestructuras híbridas. En las imágenes de la Figura 2.16 (c)-(e) se observan las NPs de Pd formadas en la superficie de la ONW (Figura 2.16 (c) y (e)), mientras que la estructura ONW interior permanece intacto (Figura 2.16 (d)). Este análisis también demuestra que cuanto mayor sea la duración del tratamiento de plasma, mayor será el número de nanopartículas (comparar Figura 2.15 (b) correspondiente a tratamiento de plasma de 1 minuto y (c) como resultado de un tratamiento de plasma de 5 minutos).

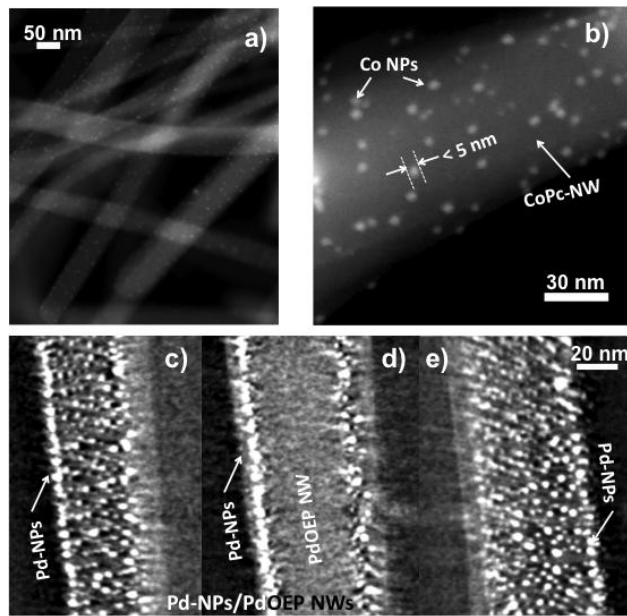


Figura 2.15. Formación de nanopartículas de metal en ONWs mediante tratamiento con plasma de oxígeno a temperatura ambiente - (a,b) Micrografías STEM a diferentes aumentos de NWs híbridas Co-NP / CoPc-NWs formadas mediante un tratamiento con plasma de oxígeno a temperatura ambiente de NWs de CoPc. Co NPs muestran un diámetro cercano a 2 nm. (e-e) Reconstrucción 3D de tomografía HAADF-STEM de una Pd-NPs/PdOEP-NWs. Las micrografías muestran los ortho-secciones verticales a través de la reconstrucción en 3D en la superficie ((c) y (e)) y el interior del nanohilo (d).

A diferencia del procesado de NWs por plasma a temperatura ambiente, el tratamiento a temperaturas más altas modifica dramáticamente la microestructura de las ONWs. En la figura 2.16 se comprueba cómo después del tratamiento con plasma a 150° C las nanopartículas de diámetro medio disminuyen mientras que su número aumenta bruscamente. Este resultado se puede interpretar suponiendo que el efecto combinado de plasma y la temperatura aumenta la movilidad de las moléculas que producen una nanoestructura 1D altamente porosa. Además, la superficie de los nanohilos presenta una rugosidad pronunciada y pequeños canales que comunican con sus núcleos. El elevado número de nanopartículas en la superficie de las NWs verificaría la hipótesis de una cierta difusión de moléculas hacia la superficie.

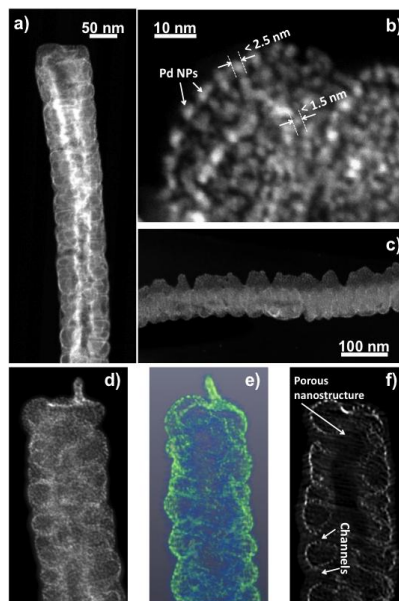


Figura 2.16. Formación de nanopartículas de metal en ONWs por tratamiento con plasma de oxígeno a temperaturas superiores a la temperatura ambiente - (a,d) Micrografías STEM a diferentes aumentos de NWs híbridas Pd-PN / PdOEP-NWs formadas mediante un tratamiento con plasma de oxígeno a 150 °C de temperatura de PdOEP NWs. (e) Vista de proyección Voxel y (f) ortho-sección vertical de la NW. (d) (diámetro de ~ 90 nm) que muestra la nanoestructura altamente porosa.



De una manera similar que para la formación de NWs jerárquicas partiendo de la superficie modificada de las NWs primarias mediante tratamientos de plasma de oxígeno, las nanopartículas situados en la superficie de las ONWs también pueden actuar como centros de nucleación para el crecimiento de ONWs secundarias siguiendo el procedimiento descrito previamente.

### 2.5.3.3 De NWs híbridas a NWs metálicas y de óxidos

En último lugar, la metodología de plasma desarrollada en este trabajo nos ofrece el uso de estas estructuras como un modelo para la fabricación de nanoestructuras 1D metálicas y de óxido soportadas en distintos sustratos. La figura 2.17 muestra un ejemplo. La nanoestructura 1D de la figura es el resultado de un tratamiento de 10 minutos de plasma sobre PdOEP NWs a 150 °C de temperatura. Los espectros XPS (no mostrados) ratifican que después de este tratamiento los componentes orgánicos se eliminan por completo y que nanopartículas de paladio parcialmente oxidadas se han aglomerado en forma de una nanoestructura inorgánica altamente porosa manteniendo la memoria de la ONW original. Es interesante destacar la homogeneidad del procesamiento de plasma de las nanoestructuras 1D a lo largo de toda su longitud. La aplicación de este procedimiento a otras moléculas orgánicas de metal abre claramente una nueva ruta para la formación de nanoestructuras 1D inorgánicas altamente porosas, como se discutirá en el próximo apartado.

El método presenta varias ventajas. Una de ellas consiste en la posibilidad de combinar las diferentes moléculas metal orgánicas en el mismo nanohilo para obtener heteroestructuras inorgánicas 1D de dos elementos diferentes, gran área de deposición y bajo consumo de energía. Por otra parte, los dos procesos involucrados en la metodología propuesta, PVD para el crecimiento ONWs y el tratamiento con plasma, se realizan en vacío que es

totalmente compatible con la fabricación de dispositivos fotónicos y microelectrónicos.<sup>1, 50</sup>

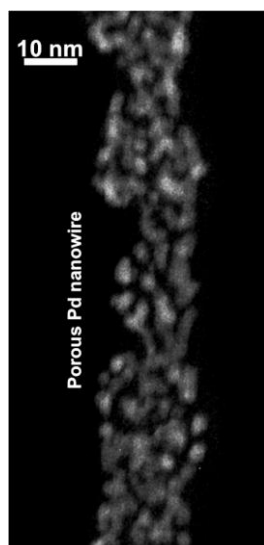
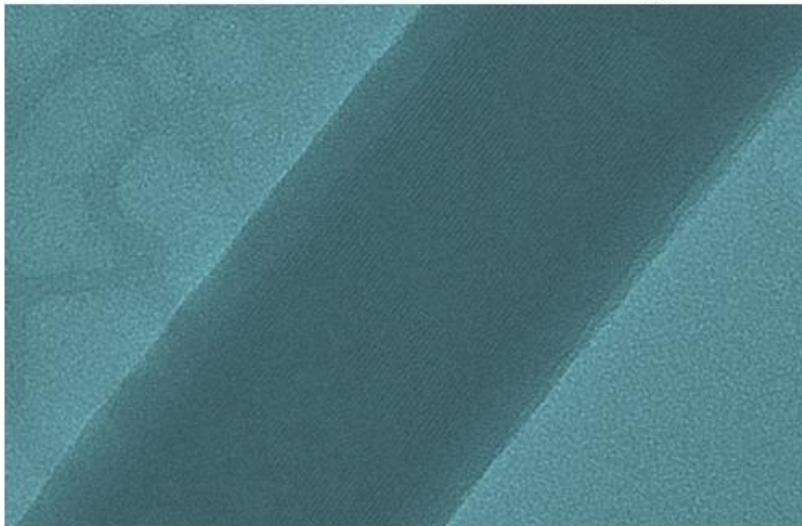
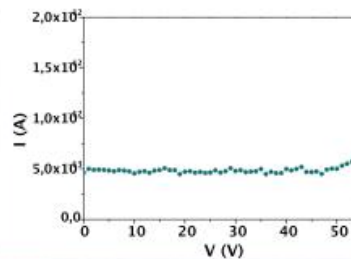


Figura 2.17. Nanohilo de óxido metálico soportado – Micrografía STEM de un nanohilo de paladio obtenido tras el tratamiento de plasma prolongado (unos 8 minutos) a temperatura suave (150°C).

## 2.6 Láminas delgadas porosas y estructuras 1D de óxido de cinc mediante procesado por plasma remoto de ftalocianina de cinc

En este apartado se presenta la fabricación de láminas de alta porosidad de ZnO y nanoestructuras 1D mediante un protocolo combinado de vacío y desbastado de plasma inspirado en la metodología desarrollada en la sección anterior. Como precursor sólido se utiliza ftalocianina de cinc (ZnPc) para formar un óxido de cinc (ZnO). En primer lugar, la ZnPc se sublima a baja presión de argón, y dependiendo de la temperatura del sustrato y la microestructura, crecen películas policristalinas o nanohilos monocristalinos de ZnO. Estos materiales de partida se someten entonces a un tratamiento oxidante

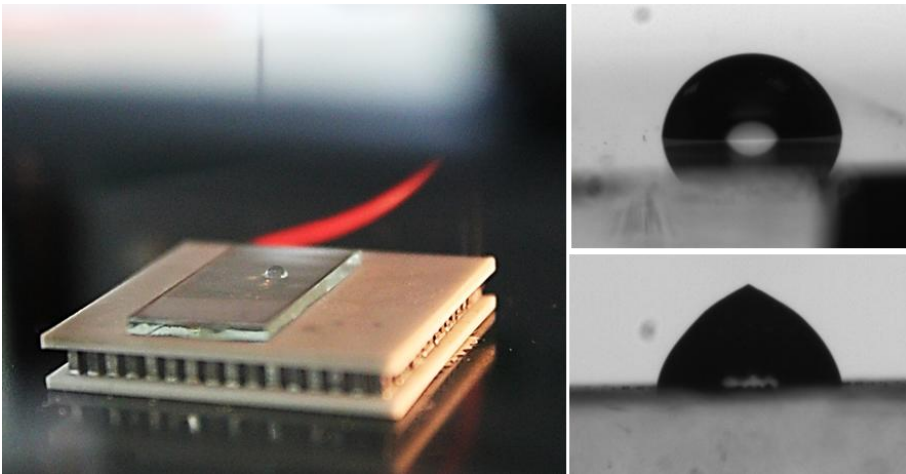
### 3 Conformal dielectric organic thin films for molecular electronics



#### ABSTRACT

Graphene based nanomaterials and molecular electronics are the paramount topics of the present nanotechnology due to the extraordinary possibilities that open for the development of nanodevices. To achieve the promises of these technological revolutions these novels conducting and semiconducting nanostructures have to be combined with state-of-the-art dielectric elements in order to produce complex architectures. Advanced dielectric materials are essential to encapsulate nanodevices for protection and packaging. Herein, we present a technique to produce transparent and robust dielectric organic thin films that can be directly deposited in delicate organic structures as organic nanowires or graphene. The films are completely conformal at the nanometer scale even on high aspect-ratio nano-objects. Besides the films are homogeneous, crack-free and stable to the atmosphere and their dielectrics properties are unaffected by corrosive saline environments.

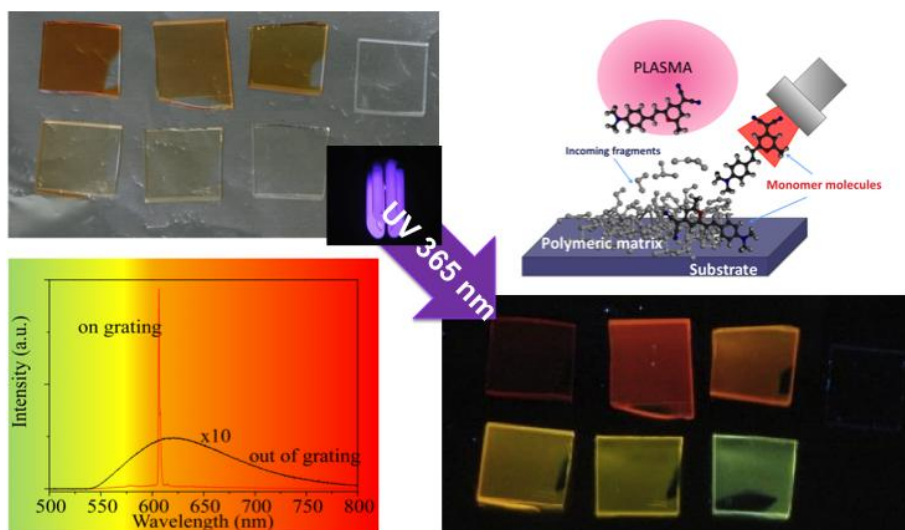
## 4 Wetting and anti-freezing properties of adamantane coatings: from thin films to 3D networks



### ABSTRACT

Here we first analyze the water wetting properties of adamantane RPAVD thin films and 1D nanostructures from room temperature to  $-10\text{ }^{\circ}\text{C}$  in the micro and macroscale. During this study, significant freezing delays times are detected for RPAVD coatings respect to the substrates. We attempt to explain this phenomenon from the study of experimental variables such as the size of water droplet and the thickness of RPAVD film. The property of conformality in RPAVD composites enables the fabrication of adamantane RPAVD films with different roughness. The roughness of the adamantane RPAVD coatings shows different behaviour on the wetting properties and the freezing delay times. We present a deep study by SEM, ESEM and WCA measures on the flat, rough and nanostructured adamantane RPAVD thin films.

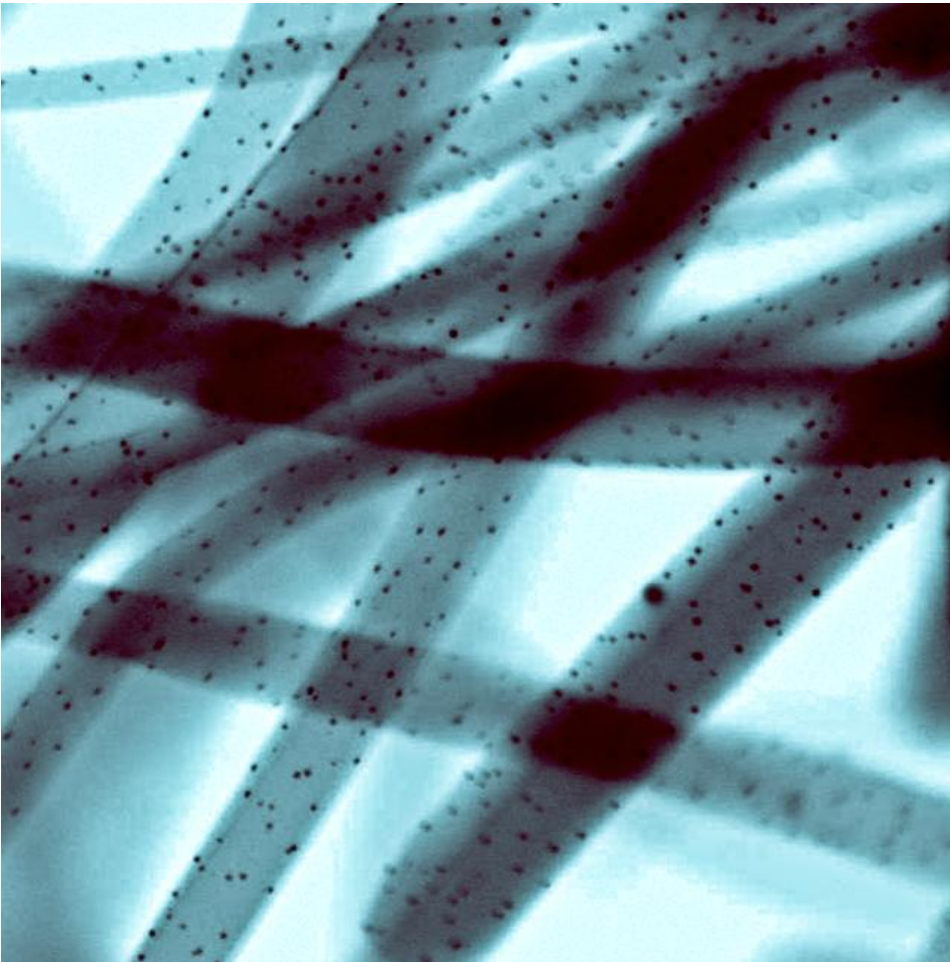
## 5 Multicolored emission and lasing in DCM-Adamantane plasma nanocomposites



### ABSTRACT

We study the synthesis of DCM laser dye containing luminescent nanocomposites in combination with adamantane. These films will be fabricated by plasma assisted vacuum deposition. The experimental parameter that determined the concentration of DCM in the films and their optical properties will be evaluated. The objective is to control the films refractive indexes and their luminescent emission in order to prepare active layers for laser devices. We will demonstrate that in this system the thin film deposition by remote plasma polymerization technique can yield optical gain materials. The ASE experiments in DCM dye/Adamantane nanocomposite waveguides will show the improvement of the nanocomposites properties as compared to the neat DCM films fabricated by the same technique. Moreover, 1D DFB laser emission will be probed and characterized in some of the nanocomposites films studied, opening up the use of remote plasma polymerization deposition technique for integrated photonics and optoelectronics.

## 6 Soft Plasma processing of Organic Nanowires: a route for the fabrication of 1D organic heterostructures and the template synthesis of inorganic 1D nanostructures



### ABSTRACT

Hierarchical (branched) and hybrid Metal-NPs/organic supported NWs are fabricated through controlled plasma processing of metalloporphyrin, metallophthalocyanine and perylene nanowires. The procedure is also applied for the development of a general template route for the synthesis of supported metal and metal oxide nanowires.

## 6.1 Introduction

The emerging field of organic nanowires (ONWs) is settling down thanks to the effort carried out during the last years in both the fabrication and the study of their properties.<sup>1-11</sup> The outstanding performance of 1D organic nanostructures based on small molecules has been proved in photonics, photovoltaic, photocatalysis, microelectronic and nanosensing applications.<sup>1-11</sup> Parallel with the inorganic counterpart, the fabrication of heterostructured organic nanowires is increasingly gaining interest because of their use in the aforementioned fields of applications as well as in the study of model systems for 1D n-p heterojunctions.<sup>12</sup> Within this framework in this work we report about an unprecedented route for the synthesis of heterostructured organic nanowires which consist of the combination of two well established vacuum processes, namely the synthesis of single crystal supported organic nanowires by physical vapour deposition<sup>13-16</sup> and oxygen plasma etching.<sup>17, 18</sup> The possibilities of this methodology are illustrated with the fabrication of two different types of organic nanostructures: heterostructured hierarchical NWs and metal-organic hybrid NWs. Ozin et al.<sup>19</sup> have previously reported on the mild air plasma processing of colloidal nanocrystals aiming at removing the organic ligands while preserving the size-dependent properties of the nanocrystals. In the present chapter we go a step forward in the use of plasmas by describing the first results of an original template method for the synthesis of inorganic 1D nanostructures by processing organic nanowires.

We also demonstrate that by controlling the intensity of the plasma treatment, the method can be used to fabricate hierarchical 1D organic heterostructures formed by two or more interconnected ONWs. This has been possible by using a cold plasma reactor, concretely a remote electron cyclotron resonance (ECR) microwave plasma that permits treatments of the organic

nanostructures at lower powers and a much better control over critical experimental parameters of the process (distance to the plasma discharge, pressure of gas, bias application on the sample holder, etc.).<sup>20, 21</sup>

## 6.2 Experimental Setup

Both different types of organic nanostructures, heterostructured hierarchical NWs and metal-organic hybrid NWs, have been grown in a remote plasma assisted vacuum deposition reactor (see Chapter 1). The fabrication process in every case is performed in three stages (Figure 6.1): i) synthesis of organic or metal-organic NWs by PVD (developed in Chapter 1), ii) formation of new nucleation centres by soft plasma processing, iii) synthesis of secondary NWs from new nuclei.

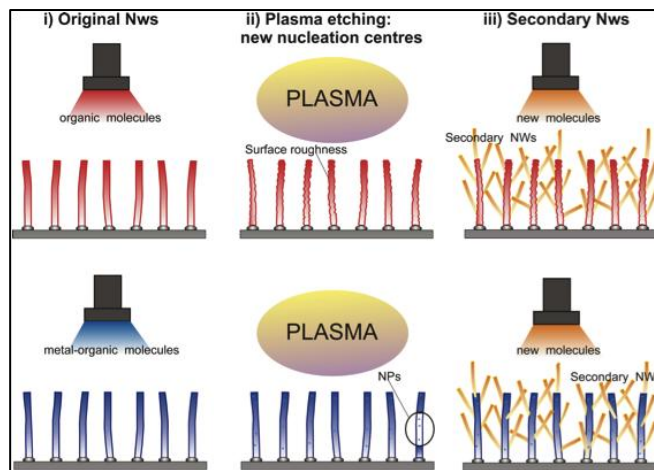


Figure 6.1. Mechanism of 1D organic heterostructures formation - Different types of organic heterostructured nanostructures stages developed combining PVD and oxygen plasma etching process. Hierarchical (a) and Metal-organic (b) NWs growth model are represented in the image by their three stages of formation.



### 6.2.1 Organic Nanowires formation by PVD

The procedure development has been fully described in previous references.<sup>13, 14</sup> Perylene-diimide (2,9-dimethyl-anthra[2,1-def:6,5,10-d'e'f']diisoquinoline 1,3,8,10-tetrone (Me-PTCDI) from Sensient Imaging Technologies.), Pd Octaethyl porphyrin (PdOEP from Frontier Sci.), and Co phthalocyanine (CoPc from Aldrich) were used as purchased (See Figure 6.2 (a) for their molecular structures).

The sublimation of the molecules for the nanowires deposition was carried out using a 10 cm<sup>3</sup> OLED Knudsen cell (Lesker) placed in the high-vacuum chamber (without plasma). The deposition system is shown in chapter 1. The system was pumped up to  $5 \cdot 10^{-6}$  mbar base pressure before the deposition. The distance between the substrate and the sublimation source was 8 cm. During the experiments argon was dosed using a calibrated mass flow controller. The pressure in the system during deposition was fixed at 0.020 mbar by a VAT controller. The growth rate was controlled by a quartz crystal microbalance located in the same plane as the substrates. The growth of the heterostructured nanowires was carried out combining two different Knudsen cells. The deposition rates were between 0.30 and 0.50 Å·s<sup>-1</sup> considering a density in the balance of 0.5 g·cm<sup>-3</sup>. ONWs were grown simultaneously on different substrates: ITO, Si(100), fused silica and Au TEM grids previously coated with silver nanoparticles by dc-sputtering and TiO<sub>2</sub> thin films deposited by vacuum methodologies. Substrates temperature (TS) for the ONWs formation depended on the organic molecule: a) for the Me-PTCDI the optima substrate temperature TS was  $175 \pm 5^\circ\text{C}$ ; b) for the PdOEP TS was  $140 \pm 5^\circ\text{C}$  and c) for the CoPc TS was  $260 \pm 5^\circ\text{C}$ .

### 6.2.2 Soft Plasma treatments

The deposition reactor is equipped with a microwave remote plasma system (2.45 GHz) allowing soft plasma processing in situ. All the experiments gathered at this work were carried out in situ under the following conditions: 150 W for the MW source, plasma gas composition 80% Oxygen – 20% Argon, total pressure at the chamber 0.020 mbar and downstream configuration, i.e. substrates emplaced out the plasma discharge, concretely at 5 cm.

### 6.2.3 Secondary Organic Nanowires formation by PVD

Plasma treatments induce changes in surface roughness of ONWs and metal atoms aggregation for ONWs grown with metal-organic molecules along their structure. Such surface modifications in turn form new nucleation centres along the NWs structure. Secondary 1D nanostructures by PVD grow on these centres as the same procedure as primary ONWs.

### 6.2.4 Characterization of 1D organic heterostructures

SEM characterization was carried in Hitachi S-4800; TEM and HAADF-STEM electron tomography was performed on a FEI Tecnai F20 field-emission gun transmission electron microscope operated at 200 kV. Data collection was carried out by tilting the specimen about a single axis from  $-64^\circ$  to  $+62^\circ$  with a  $2^\circ$  increment, using a Fischione ultrahigh-tilt tomography holder, and acquiring the images with the FEI software package Xplore3D. The tilt series was then exported to the FEI software Inspect3D for the cross-correlation alignment and the tomographic reconstruction using the iterative routine SIRT. Slice viewing after a global thresholding was undertaken using Amira software. ONWs were analyzed by TEM directly grown of the TEM grids or after removed from the substrates by scratching and dispersion in ethanol and then “fished” in a holy

carbon grid. Fluorescence microscopy images were obtained with a Olympus BX51 fluorescence microscope. Fluorescence spectra were recorded in a Jobin Yvon Fluorolog3 spectrofluorometer using the front face configuration and grids of 4 and 2 nm for the excitation and emission monochromators, respectively.

## 6.3 Results and discussion

### 6.3.1 Heterostructured hierarchical NWs formed by oxygen plasma

In previous publications<sup>13-16</sup>, we have presented a general method for the growth of squared ONWs and nanobelts through the controlled sublimation of  $\pi$ -molecules on substrates with a tailored morphology. This method provides a straightforward route for the high density fabrication of single crystal organic nanowires of metallo-porphyrins (M-OEP), phthalocyanines (MPc) and perylenes (MePTCBI) (see Figure 6.2 (a) for molecular structure) supported on substrates such as TiO<sub>2</sub>, ZnO, ITO and SiO<sub>2</sub>, metal nanoparticles, metal thin films, etc.<sup>13-16</sup>

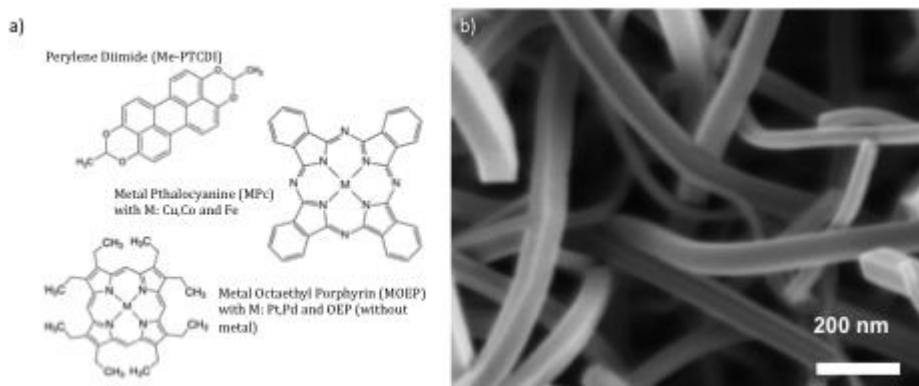


Figure 6.2. Single Crystal Organic Nanowires by PVD – (a) Chemical structure of M-OEP, M-Pc and perylene as labelled. (b) Normal view SEM micrograph of CoPc NWs deposited on an ITO substrate. Mostly squared NWs appear in the image.

Figure 6.2 (b) shows a characteristic SEM micrograph of squared NWs comprised of Co-phthalocyanine (CoPc) fabricated on ITO. The novelty in the fabrication of the new heterostructures is the post-treatment of the as grown single crystal nanowires by remote microwave oxygen plasma. The effect of the controlled oxidation on the nanowires depends on: i) plasma gas composition and plasma parameters; ii) the chemical structure of the molecules either containing a metal atom (i.e. CoPc, PdOEP, PtOEP) or being purely organic (OEP, Pc or perylene); iii) temperature during the plasma processing and treatment duration.

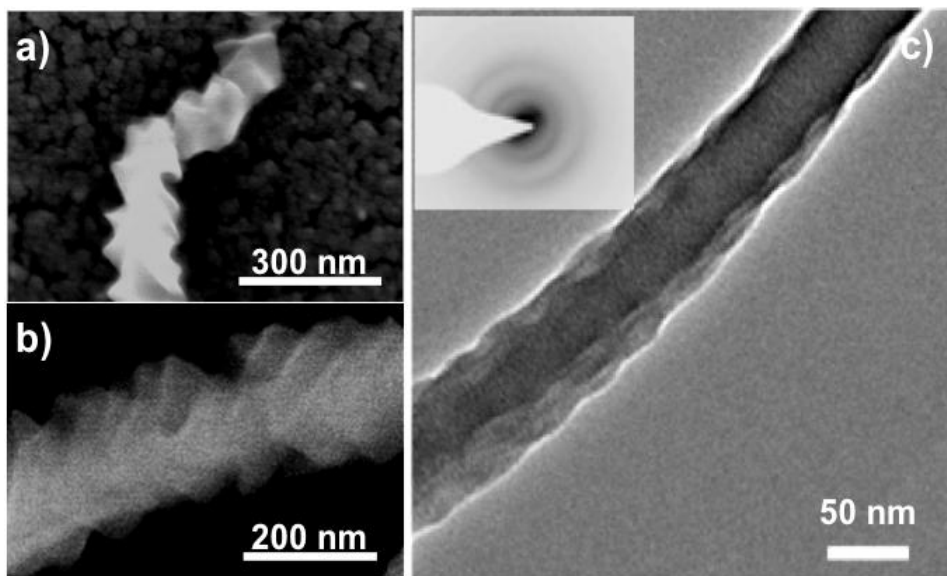


Figure 6.3. Plasma treated NWs at temperature above RT – SEM (a-b) and TEM (c) micrographs of individual MePTCDI nanowires after plasma treatment at 110°C during 30 minutes. The inset in (c) shows the SAED of the NW in the image.

The first series of results gathered herein to illustrate the possibilities of the proposed methodology show the effect of a MW oxygen plasma on the ONWs located in a downstream configuration with respect to the plasma source (i.e. out of glow discharge) for a nominal power of 150 W and a pressure in the plasma reactor of  $2 \times 10^{-2}$  mbar, as noted in the previous section. Figure 6.3 shows the changes induced by this plasma on perylene NWs after a 30 minutes treatment at 110 °C. The etching induced by the plasma on the NWs produces an important increment in their surface roughness and a decrease in their thickness. The original squared and pristine surface (Figure 6.2) appears now highly rough with triangular features perpendicular to the NW growth direction. Although the instability of the organic nanostructures under the electron beam hinders their full characterization by selected area electron diffraction (SAED), the inset in Figure 6.3 might indicate that the NWs keep the original crystal structure<sup>13-16</sup>. The formation of the triangular surface is enhanced at temperatures close to the sublimation temperature of the molecules. For lower temperatures the changes in the surface roughness are only visible after very prolonged treatments (up to 60 minutes). This controlled roughening of the NWs surfaces can be quite advantageous for different applications. For example an increment of the surface area of the ONWs may positively affect to their sensor properties<sup>22</sup>.

Additionally, the controlled plasma etching of the ONWs induces the formation of new nucleation centres along their structure allowing the growth of new (secondary) 1D nanostructures. Indeed, our previous results on the ONWs formation by physical vapour deposition demonstrated that these structures always develop from well-defined nucleation centres, as for example the surface of metal NPs, well defined oxide grains, etc<sup>3</sup>. Figure 6.4 shows the growth of secondary ONWs and nanobelts of different molecules emerging from primary perylene NWs with their surface slightly modified by oxygen plasma at room temperature. Thus, hierarchical nanostructures such as perylene-perylene

(Figure 6.4 (a)) or OEP-OEP NWs branched connections can be easily fabricated by switching on the plasma during several seconds to induce the formation of some nuclei and then pursuing the molecules sublimation. Similarly, 1D heterostructures based on perylene-PdOEP NWs can be synthesized by applying a soft plasma to the initially formed perylene NWs followed by the sublimation of PdOEP (Figure 6.4 (b)-(d)).

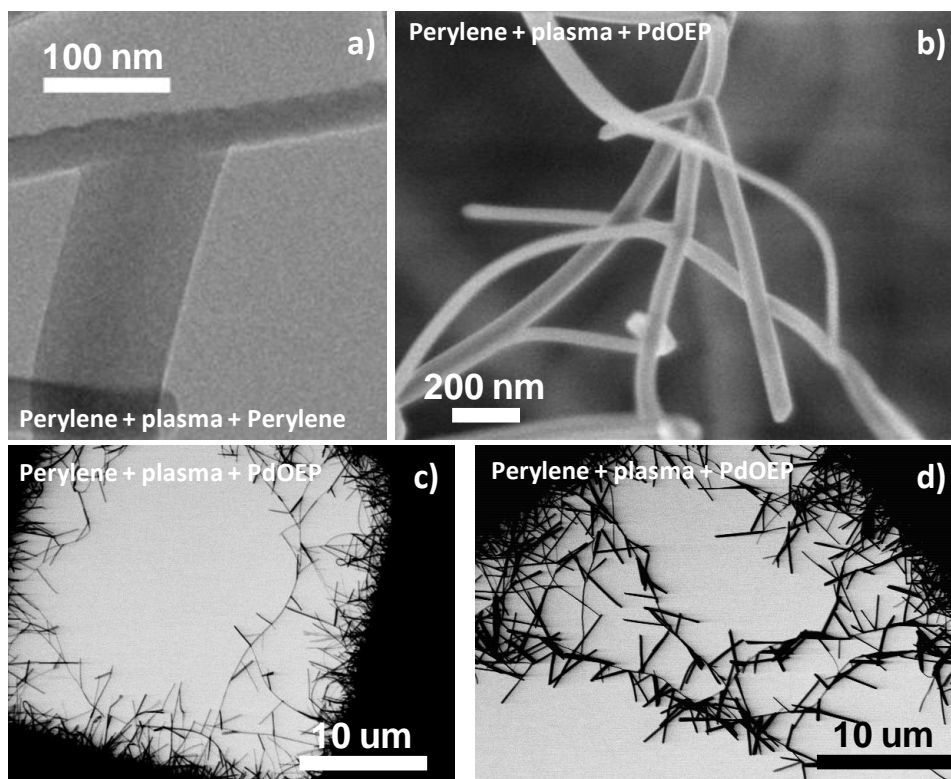


Figure 6.4. Hierarchical nanostructures – (a) TEM micrograph of a perylene nanobelt growing from a perylene nanowire. High magnification SEM (b) and low magnification (c-d) STEM micrographs showing the hierarchical growth of PdOEP-NWs / perylene-NWs.

In the two cases, the number of secondary NWs is related with the induced roughness (compare Figure 6.4 (c) plasma processing of the perylene NWs during 5 minutes and (d) 15 minutes), i.e. it depends on the duration and the temperature during the plasma treatment. We foresee that the direct fabrication of these heterostructures in a high density supported on substrates (Figure 6.5) will have important implications for light harvesting and nanosensor applications (e.g., to get multisensory performance combining different molecules for the formation of the hierarchical NWs).

It is worth noting that the optical properties of the perylene, Pc or OEP NWs working as primary NWs are not influenced by a mild plasma treatment at low temperatures. Thus, Figure 6.6 shows the fluorescence microscopy images and emission spectra of a system formed by perylene/PdOEP NWs under different excitation wavelengths.

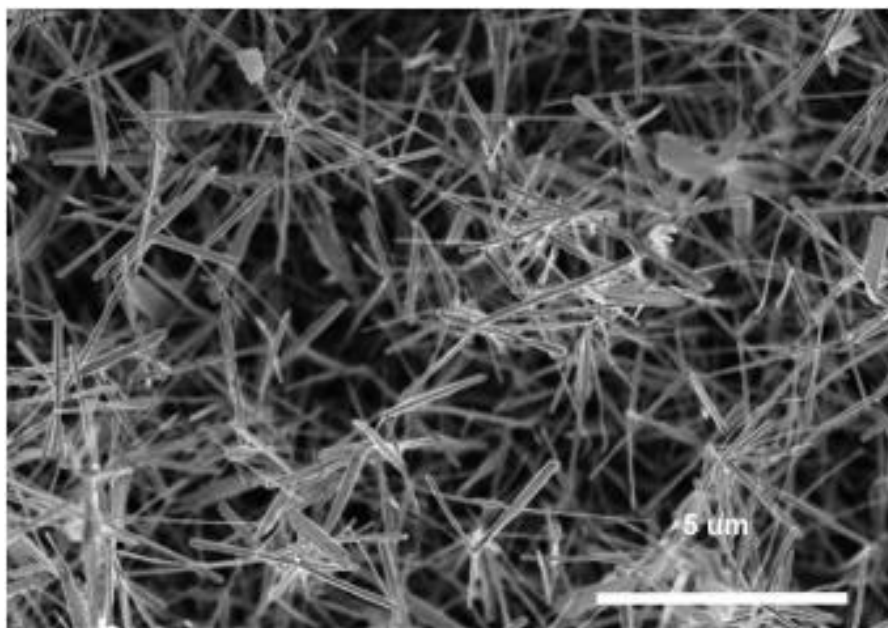


Figure 6.5. High density of hierarchical NWs – Low magnification SEM micrograph of hierarchical perylene/PdOEP-NWs.

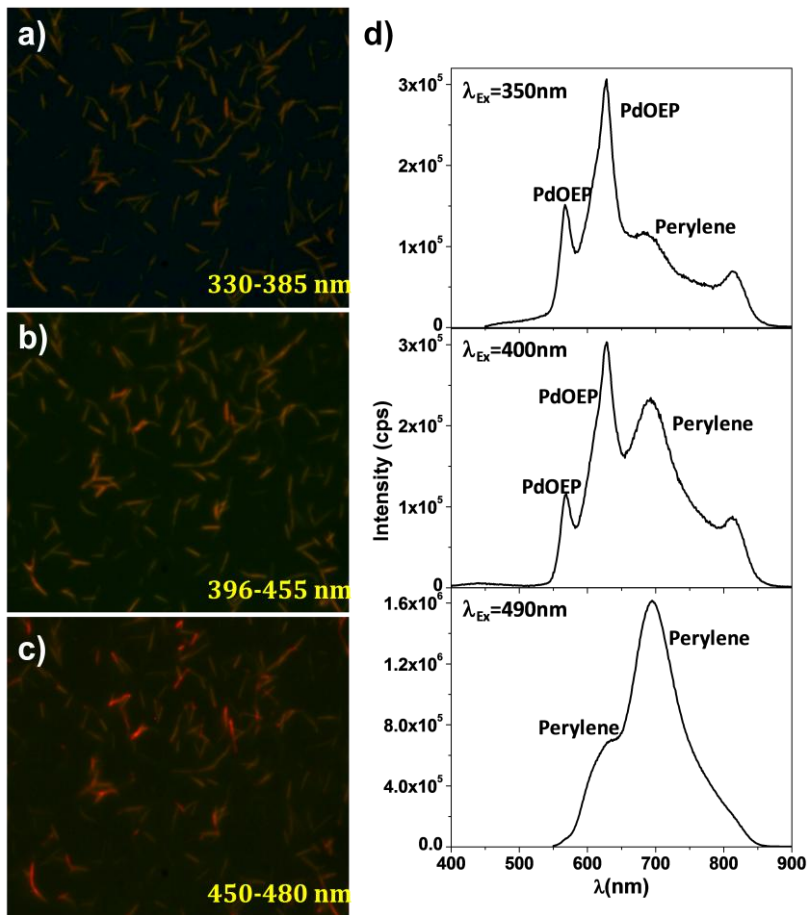


Figure 6.6. Fluorescence images and emission spectra of hierarchical structures – (a) Fluorescence microscope images (a-c) and emission (d) of perylene/PdOEP NWs recorded at different excitation wavelengths as labelled. The emission peaks or bands for each component are marked.

The spectra show that the two component materials, Pd porphyrin and perylene (MePTCDI), emit independently when excited at  $\lambda = 350\text{ nm}$  and  $\lambda = 490\text{ nm}$  correspondingly. The obtained spectra show that the contribution of the perylene emission grows as the excitation wavelength increases while that of the Pd porphyrin decreases, in agreement with the fact that the excitation of this latter vanishes at the longest wavelengths. This result supports that for



components sensitive to different gases or agents (e.g. perylene for NO<sub>2</sub> and porphyrin for oxygen)<sup>22-24</sup> the system would act as an optical multisensor by following the corresponding enhancement/quenching of the different light emissions.

### 6.3.2 Metal-Organic Hybrid NWs formed by SOFT plasma processing

Another possibility of this methodology is the formation of hybrid metal-organic nanowires. The origin of the inorganic material is the formation of metal nanoparticles by aggregation of the metal atoms resulting from the plasma decomposition of the outerlayers of the primary metal organic molecular structure.

During the oxygen plasma treatment, the organic part of the molecules becomes etched by reacting with the excited species of oxygen and the volatile fragments and products evacuated by the vacuum system<sup>17, 18</sup>. As a consequence, metal atoms remain at the NW forming nanoparticles whose size and density depend on the experimental conditions and metal atom within the molecule. The examples gathered in Figure 6.7 and Figure 6.9 refer to plasma treated PdOEP and CoPc NWs at different temperatures conditions. They illustrate the possibilities of the method by showing Co-NPs/CoPc NW and Pd-NPs/PdOEP NWs with different NPs size distributions.

#### 6.3.2.1 Nps formed by treatments at RT on NWs surfaces

The bright spots in the STEM micrographs in Figure 6.7 clearly shows the formation of metal NPs at the surface of the ONWs treated with an oxygen plasma at room temperature.

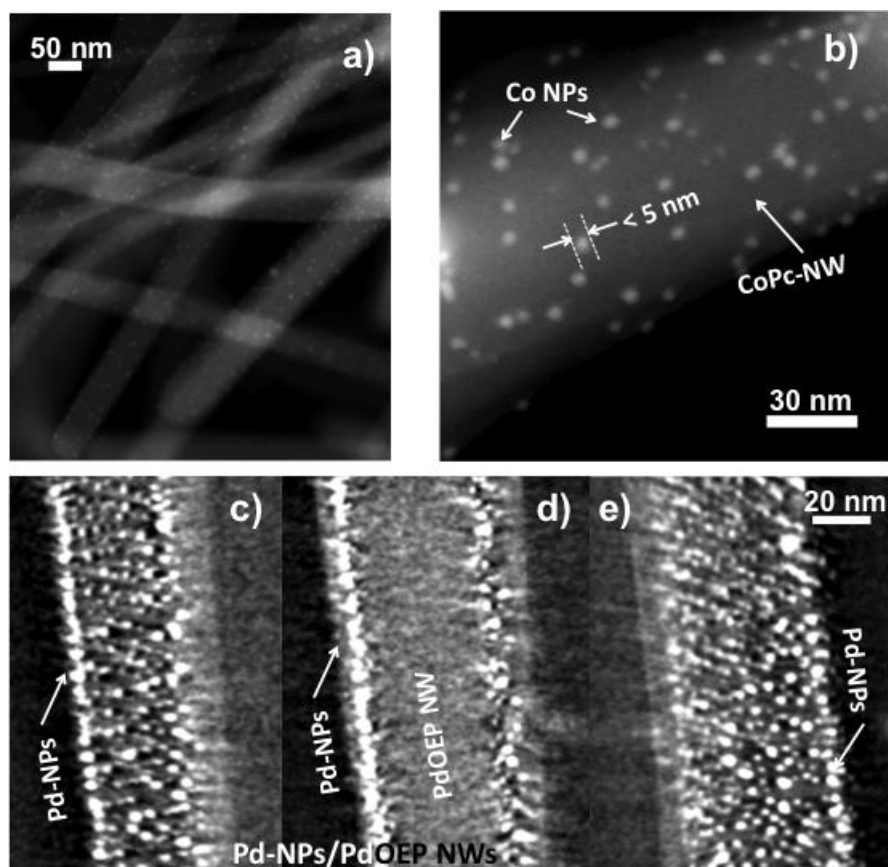


Figure 6.7. Formation of metal NPs on ONWs by oxygen plasma treatment at RT – (a-b) STEM micrographs at different magnifications of hybrid Co-NPs/CoPc-NWs formed by oxygen plasma treatment at room temperature of CoPc NWs. Co NPs mean diameter ca. 2 nm (c-e) 3D HAADF-STEM tomography reconstruction of a single Pd-NPs/PdOEP-NW. The micrographs show the vertical orthoslices through the 3D reconstruction at the surface ((c) and (e)) and the interior of the wire.

A close inspection of the NWs in Figure 6.7 (a) indicates that the formation of the NPs occurs all along the NWs length. Figure 6.8 shows the NPs size histograms for different molecule composition and plasma treatments. The NPs size has been estimated from a statistical analysis of SEM micrographs. NPs mean diameter as low as 1.6 nm can be achieved by these treatment.

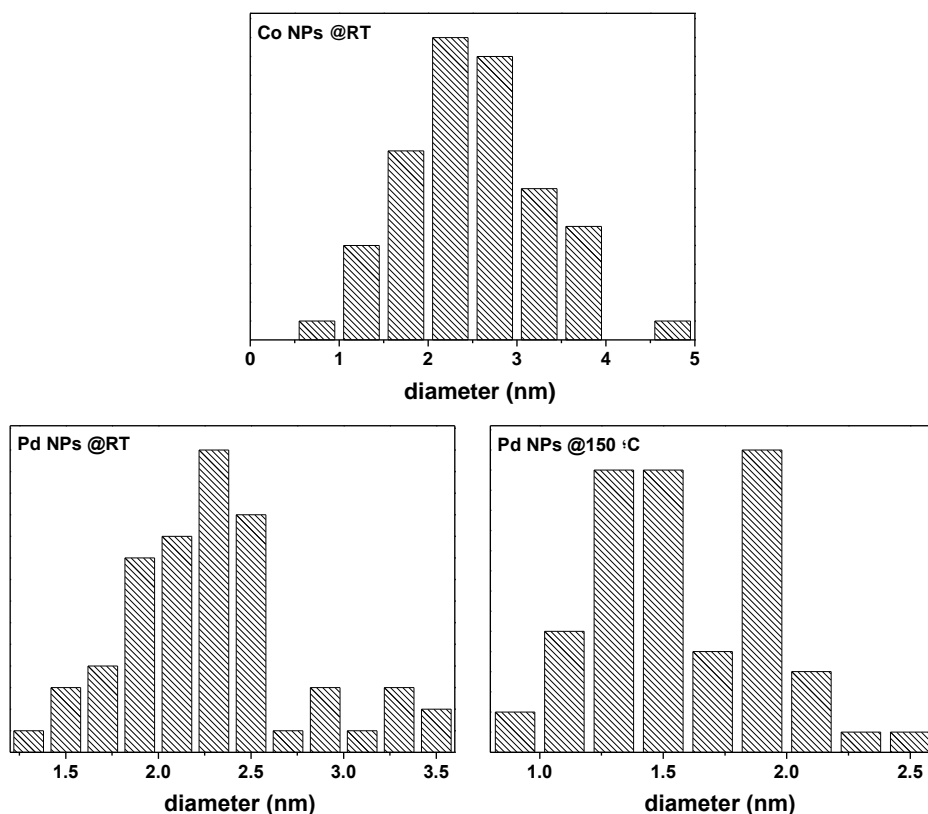


Figure 6.8. Size histograms for NPs – Co (a) and Pb (b-c) nanoparticles formed at: a) room temperature after 1 minutes; b) room temperature after 5 minutes and c) 150°C after 5 minutes. The mean diameter for the Co NPs in a) is about 2.5 nm; for the Pd NPs in b) about 2.3 nm and c) 1.6 nm.

Furthermore, the 3D reconstruction by the high-angle annular dark field scanning transmission electron microscopy (HAADF-STEM) tomography technique<sup>25-27</sup> has allowed us to fully describe the internal microstructure of these hybrid nanostructures. The snapshots in Figure 6.7 (c)-(e) (see also Videos 1 and 2) show that the Pd NPs have been formed at the surface of the ONW (Figure 6.7 (c) and (e)) while the inner ONW structure remains untouched (Figure 6.7 (d)). This analysis also demonstrates that the longer the plasma treatment duration, the higher the number of nanoparticles (compare Figure 6.7

(b) corresponding to plasma treatment of 1 minute and (c) resulting from a plasma treatment of 5 minutes).

### 6.3.2.2 Nps formed by treatments at temperatures above RT on NWs surfaces

Unlike the plasma processing at room temperature, the treatment at higher temperatures strongly modifies the ONWs microstructure. Figure 6.9 and Video 6.3 shows that after the plasma treatment at 150° C the nanoparticles mean diameter decreases while their number abruptly increases (Figure 6.8). This result can be interpreted by assuming that the combined effect of plasma and temperature enhances the mobility of the molecules producing a highly porous 1D nanostructure.

Moreover, the surface of the nanowires presents a pronounced roughness and small channels communicating with their core. Clear examples of this new type of nanostructure are reported in Figure 6.9 (a) and (d) where the NWs appear to be hollow. The vertical orthoslice in (f) further demonstrates the internal porosity induced by the plasma processing at mild temperatures. The high number of nanoparticles at the surface of the NWs would support the hypothesis of a certain diffusion of molecules towards the surface.

### 6.3.2.3 NPs as nucleation centres allowing the growth of secondary NWs

In a similar way than for the formation of hierarchical NWs from the modified surface of the primary NWs by oxygen plasma treatments, the nanoparticles located at the surface of the ONWs can also act as nucleation centres for the growth of secondary ONWs following the procedure described in section 3.1.3. This effect can be observed in Figure 6.10.

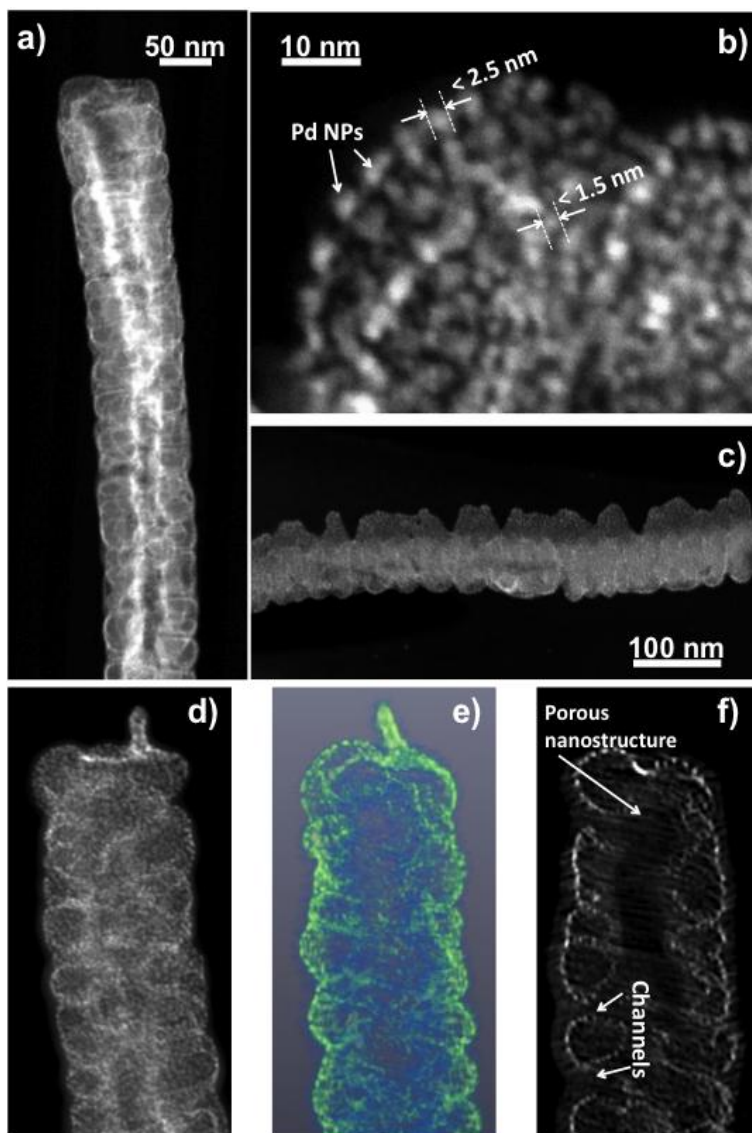


Figure 6.9. Formation of metal NPs on ONWs by oxygen plasma treatment at temperatures above RT – (a-d) STEM micrographs at different magnifications of hybrid Pd-NPs/PdOEP-NWs formed by oxygen plasma treatment at 150 °C temperature of PdOEP NWs. See also the 3D reconstruction of a Pd-NP/PdOEP-NW in the Video 6.3. (e) Voxel projection view and (f) vertical orthoslice of the NW in (d) (diameter  $\sim 90$  nm) showing the highly porous nanostructure.

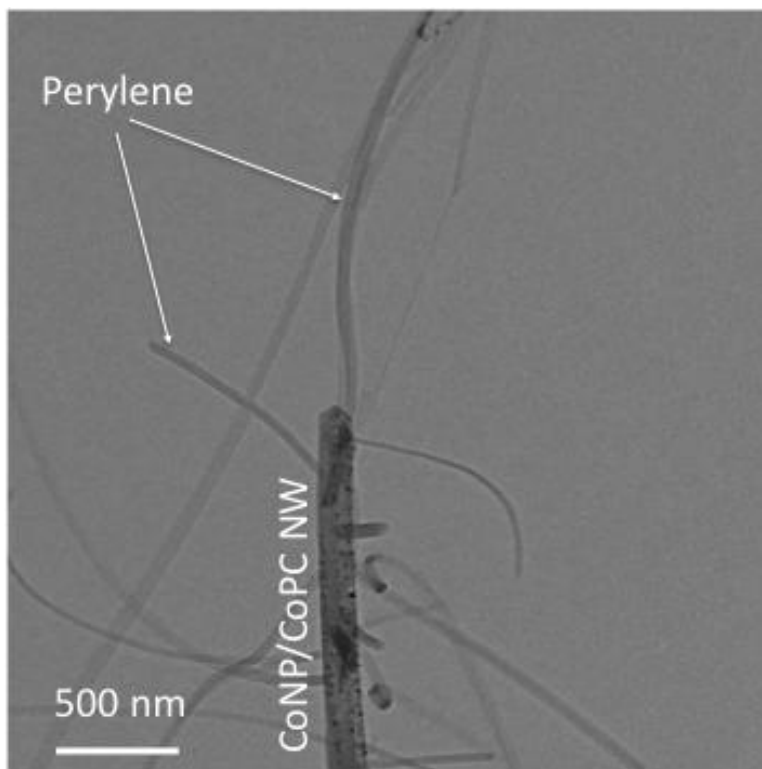


Figure 6.10. Metal-Organic hybrid NW – TEM micrograph showing perylene NWs growing from the Co NPs formed at RT on the surface of a CoPc NW.

### 6.3.3 From Hybrid to metal and oxide NWs

Finally, another choice of the plasma methodology developed here consists of the use of these structures as a template for the fabrication of supported 1D metal and oxide nanostructures.

Figure 6.11 illustrates an example of the realization of this idea. The reported 1D nanostructure is the result of the plasma processing during 10 minutes of PdOEP NWs at 150 °C. XPS spectra (not shown) exhibit that after this treatment the organic components are completely removed and partially oxidized palladium nanoparticles agglomerate in the form of a highly porous inorganic nanostructure keeping memory of the original ONW. It is interesting

to emphasize the homogeneity of the plasma processing of the 1D supported nanostructures along their entire lengths.

The application of this procedure to other metal organic molecules clearly opens a new route for the formation of highly porous inorganic 1D nanostructures, as will be discussed in the next chapter.

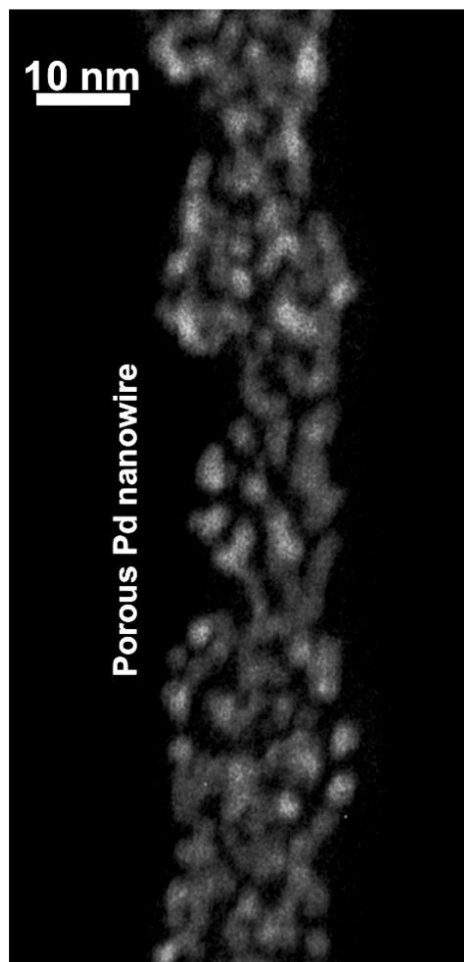


Figure 6.11. Supported metal oxide NW- STEM micrograph of a Pd nanowire obtained after prolonged plasma processing (about 8 min) at mild temperature (150°C).

The method presents several advantages. One of them consists in the possibility of combining different metal organic molecules in the same nanowire to get inorganic 1D inorganic heterostructures of two different elements, large area deposition and low energy consumption. Furthermore, the two step processes involved in the proposed methodology, PVD for ONWs growth and the plasma treatment, are made in a vacuum environment that is fully compatible with the fabrication of photonic and microelectronic devices.<sup>28, 29</sup>

## 6.4 Conclusions

In summary, herein we have discussed the effect of the soft plasma processing of organic nanowires formed by the stacking of small molecules. Plasma treatments of pure organic NWs induce the formation of nucleation sites along the NW length that act as centres for the growth of secondary ONWs in a hierarchical configuration. The treatment of NWs fabricated from metal organic molecules results in the formation of hybrid metalorganic NWs whose microstructure can be controlled by the substrate temperature and the plasma treatment duration.

Furthermore, under certain conditions, the procedure works as a template process for the development of inorganic NWs constituted by the metal NPs (or the corresponding metal oxide NPs) corresponding to the metallic cation of the original organic molecules. Different fields of applications will likely profit from these supported hybrid nanowires (e.g., applications in catalysis, for non-volatile memory devices, SERS, enhanced fluorescence and electroluminescence, etc.).<sup>1, 22, 30, 31</sup> On the other hand, although in this work we have processed supported ONWs fabricated by a PVD method, we believe that similar results will be reproducible on ONWs synthesised by other established methodologies.<sup>1, 22, 30, 31</sup> Finally, it is important to remark the large margin for experimental conditions provided by the cold plasmas for the fabrication of these



new organic and hybrid nanostructures. This type of plasmas permits a wide range of possibilities from mild treatments with effects barely visible under the electron beam of the SEM or TEM instruments to the much stronger conditions enabling a new type of template synthesis for the formation of inorganic NWs.

## REFERENCES

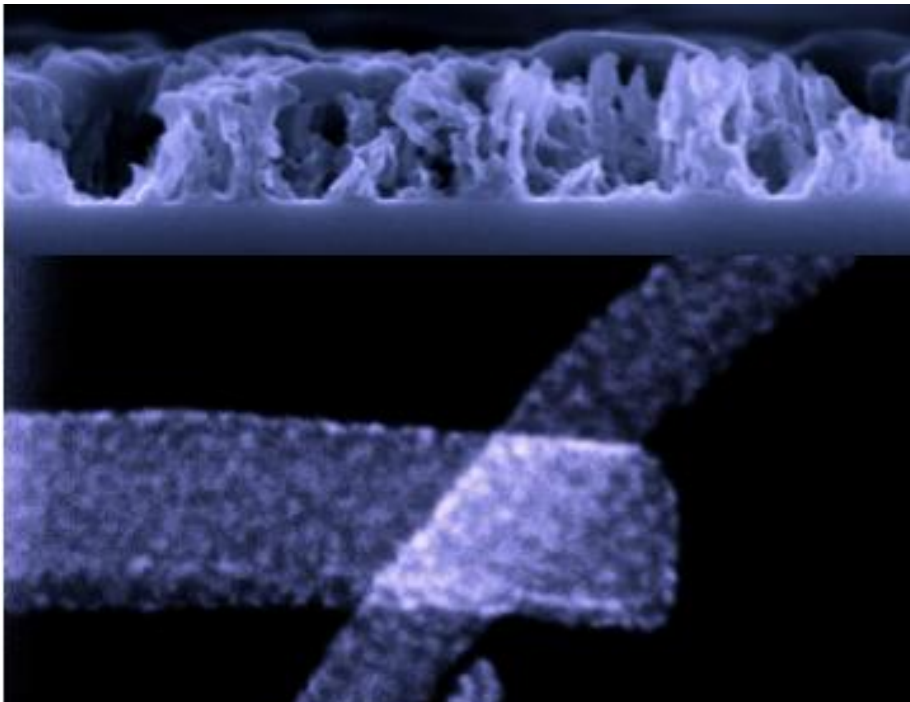
1. Briseno, A. L.; Mannsfeld, S. C. B.; Jenekhe, S. A.; Bao, Z.; Xia, Y. N., Introducing organic nanowire transistors. *Materials Today* **2008**, 11, (4), 38-47.
2. Forrest, S. R., The path to ubiquitous and low-cost organic electronic appliances on plastic. *Nature* **2004**, 428, (6986), 911-918.
3. Claessens, C. G.; Hahn, U.; Torres, T., Phthalocyanines: From outstanding electronic properties to emerging applications. *The Chemical Record* **2008**, 8, (2), 75-97.
4. Troshin, P. A.; Koeppe, R.; Peregudov, A. S.; Peregudova, S. M.; Egginger, M.; Lyubovskaya, R. N.; Sariciftci, N. S., Supramolecular Association of Pyrrolidinofullerenes Bearing Chelating Pyridyl Groups and Zinc Phthalocyanine for Organic Solar Cells. *Chemistry of Materials* **2007**, 19, (22), 5363-5372.
5. Curtis, M. D.; Cao, J.; Kampf, J. W., Solid-state packing of conjugated oligomers: from pi-stacks to the herringbone structure. *Journal of the American Chemical Society* **2004**, 126, (13), 4318-4328.
6. Wang, W.; Han, J. J.; Wang, L.-Q.; Li, L.-S.; Shaw, W. J.; Li, A. D. Q., Dynamic  $\pi$ - $\pi$  Stacked Molecular Assemblies Emit from Green to Red Colors. *Nano Letters* **2003**, 3, (4), 455-458.
7. Xiao, K.; Ivanov, I. N.; Puretzky, A. A.; Liu, Z.; Geohegan, D. B., Directed Integration of Tetracyanoquinodimethane-Cu Organic Nanowires into Prefabricated Device Architectures. *Advanced Materials* **2006**, 18, (16), 2184-2188.
8. Naddo, T.; Che, Y.; Zhang, W.; Balakrishnan, K.; Yang, X.; Yen, M.; Zhao, J.; Moore, J. S.; Zang, L., Detection of Explosives with a Fluorescent Nanofibril Film. *Journal of the American Chemical Society* **2007**, 129, (22), 6978-6979.
9. Tang, Q.; Tong, Y.; Zheng, Y.; He, Y.; Zhang, Y.; Dong, H.; Hu, W.; Hassenkam, T.; Bjørnholm, T., Organic Nanowire Crystals Combine Excellent Device Performance and Mechanical Flexibility. *Small* **2011**, 7, (2), 189-193.
10. Krauss, T. N.; Barrera, E.; Lohmuller, T.; Spatz, J. P.; Dosch, H., Growth mechanisms of phthalocyanine nanowires induced by Au nanoparticle templates. *Physical Chemistry Chemical Physics* **2011**, 13, (13), 5940-5944.
11. Hirade, M.; Nakanotani, H.; Yahiro, M.; Adachi, C., Formation of Organic Crystalline Nanopillar Arrays and Their Application to Organic Photovoltaic Cells. *Acs Applied Materials & Interfaces* **2011**, 3, (1), 80-83.
12. Zhang, Y. J.; Dong, H. L.; Tang, Q. X.; Ferdous, S.; Liu, F.; Mannsfeld, S. C. B.; Hu, W. P.; Briseno, A. L., Organic Single-Crystalline p-n Junction Nanoribbons. *Journal of the American Chemical Society* **2010**, 132, (33), 11580-11584.

13. Borrás, A.; Aguirre, M.; Groening, O.; Lopez-Cartes, C.; Groening, P., Synthesis of Supported Single-Crystalline Organic Nanowires by Physical Vapor Deposition. *Chemistry of Materials* **2008**, 20, (24), 7371-7373.
14. Borrás, A.; Groning, O.; Aguirre, M.; Gramm, F.; Groning, P., One-Step Dry Method for the Synthesis of Supported Single-Crystalline Organic Nanowires Formed by pi-Conjugated Molecules. *Langmuir* **2010**, 26, (8), 5763-5771.
15. Borrás, A.; Groning, P.; Sanchez-Valencia, J. R.; Barranco, A.; Espinos, J. P.; Gonzalez-Elipe, A. R., Air- and Light-Stable Superhydrophobic Colored Surfaces Based on Supported Organic Nanowires. *Langmuir* **2010**, 26, (3), 1487-1492.
16. Borrás, A.; Groning, O.; Koble, J.; Groning, P., Connecting Organic Nanowires. *Advanced Materials* **2009**, 21, (47), 4816-+.
17. d'Agostino, R., *Plasma Deposition, Treatment, and Etching of Polymers*. Academic Press Inc.: San Diego (US), 1990.
18. Ostrikov, K.; Xu, S.; Huang, S. Y.; Levchenko, I., Nanoscale surface and interface engineering: Why plasma-aided? *Surface & Coatings Technology* **2008**, 202, (22-23), 5314-5318.
19. Cademartiri, L.; Ghadimi, A.; Ozin, G. A., Nanocrystal Plasma Polymerization: From Colloidal Nanocrystals to Inorganic Architectures. *Accounts of Chemical Research* **2008**, 41, (12), 1820-1830.
20. Yasuda, H., *Luminous Chemical Vapor Deposition and Interface Engineering*. Marcel Dekker: New York, 2005.
21. Grill, A., *Cold plasma in materials fabrication* IEEE Press ; Institute of Electrical and Electronics Engineers: Birmingham (UK), 1994.
22. Wang, Z. C.; Medforth, C. J.; Shelnutt, J. A., Porphyrin nanotubes by ionic self-assembly. *Journal of the American Chemical Society* **2004**, 126, (49), 15954-15955.
23. Douglas, P.; Eaton, K., Response characteristics of thin film oxygen sensors, Pt and Pd octaethylporphyrins in polymer films. *Sensors and Actuators B: Chemical* **2002**, 82, (2-3), 200-208.
24. Blaszczyk-Lezak, I.; Aparicio, F. J.; Borrás, A.; Barranco, A.; Alvarez-Herrero, A.; Fernandez-Rodriguez, M.; Gonzalez-Elipe, A. R., Optically Active Luminescent Perylene Thin Films Deposited by Plasma Polymerization. *Journal of Physical Chemistry C* **2009**, 113, (1), 431-438.
25. Midgley, P. A.; Weyland, M., 3D electron microscopy in the physical sciences: the development of Z-contrast and EFTEM tomography. *Ultramicroscopy* **2003**, 96, (3-4), 413-431.
26. Banhart, J., *Advanced Tomographic Methods in Materials Research and Engineering*. Oxford (United Kingdom), 2008; p 335-373.

27. Midgley, P. A.; Weyland, M.; Thomas, J. M.; Johnson, B. F. G., Z-Contrast tomography: a technique in three-dimensional nanostructural analysis based on Rutherford scattering. *Chemical Communications* **2001**, (10), 907-908.
28. Aparicio, F. J.; Holgado, M.; Borrás, A.; Blaszczyk-Lezak, I.; Griol, A.; Barrios, C. A.; Casquel, R.; Sanza, F. J.; Sohlstrom, H.; Antelius, M.; Gonzalez-Elipe, A. R.; Barranco, A., Transparent Nanometric Organic Luminescent Films as UV-Active Components in Photonic Structures. *Advanced Materials* **2011**, 23, (6), 761-765.
29. Barranco, A.; Aparicio, F.; Yanguas-Gil, A.; Groening, P.; Cotrino, J.; Gonzalez-Elipe, A. R., Optically active thin films deposited by plasma polymerization of dye molecules. *Chemical Vapor Deposition* **2007**, 13, (6-7), 319-325.
30. Tseng, R. J.; Huang, J.; Ouyang, J.; Kaner, R. B.; Yang, Polyaniline Nanofiber/Gold Nanoparticle Nonvolatile Memory. *Nano Letters* **2005**, 5, (6), 1077-1080.
31. Milliron, D. J.; Gur, I.; Alivisatos, A. P., Hybrid Organic–Nanocrystal Solar Cells. *MRS Bulletin* **2005**, 30, (01), 41-44.




## 7 Highly porous ZnO thin films and 1D nanostructures by remote plasma processing of Zn-phthalocyanine



### ABSTRACT

We present the fabrication of highly porous ZnO layers and 1D nanostructures by a vacuum and plasma etching combined protocol. Zn-phthalocyanine (ZnPc) is utilized as solid precursor to form the ZnO. First the ZnPc is sublimated in low Argon pressure. Depending on the substrate temperature and microstructure, polycrystalline films or single crystal ZnPc nanowires are grown. These starting materials are then subjected to a remote plasma oxidizing treatment. Experimental parameters such as plasma gases composition, plasma power, treatment duration and substrate temperature determine the microstructure and properties of the final ZnO nanostructures. The chapter gathers an in deep study by SEM, TEM, XPS, UV-Vis transmittance and fluorescence spectroscopy on the different porous nanostructures obtained. In addition, the use of the ZnO layers as optical oxygen sensor is proposed.

## **8 General conclusions**



---


This chapter summarize in a list the main achievements and conclusions of the work developed throughout the present Thesis:

- A deposition technique based on ECR remote plasma has been used to grow organic thin films and nanostructures integrating functional molecules. The technique called remote plasma assisted vapour deposition (RPAVD) employs solid organic precursors.
- Transparent thin films have been obtained by the plasma assisted vacuum deposition of adamantane. The films are completely transparent in the visible and in the UV regions at wavelengths higher than 300 nm. The deposition process is fully compatible with plasma etching processes and wafer scale integration.
- The films present very high dielectric breakdown field in the range 4.5-7.3 MV/cm and can be conformally deposited on delicate substrates as graphene monolayers and organic nanowires to fabricate devices. The deposition process does not damage these substrates.
- The results probe the adamantane films are ideal candidates for their integration as versatile dielectric element in organic electronic devices. For example, the films can be used as insulator elements for conducting organic nanowires protecting such structures against oxidation and reduction in saline environments.
- Adamantane thin films deposited on flat substrates are partially hydrophobic (WCA about 85°) at room and sub-zero temperatures.
- The WCAs of the adamantane thin films does no depend on the thin film thickness.
- The freezing delay time of flat adamantane thin films strongly depends on the thickness. Thicker films yield longer delay times. A freezing delay times as long as 54 minutes has been achieved for a 1 um thick



film. The freezing delay time of adamantane thin films decreases as the water droplet volume increases.

- Hydroxylation of the adamantane surface by functionalization with a soft oxygen plasma treatment reduces the freezing delay time.
- Adamantane layers delay the freezing on nanostructured SiO<sub>2</sub> thin films (up to 90 times with respect to the reference) while the deposition of adamantane on 1D supported nanostructures provides highly hydrophobic surfaces with freezing delay time of about 40 minutes. The deposition of adamantane on dual scale rough substrates produces water repellent surfaces (WCA ca. 180°) showing freezing times above 2 hours.
- Three dimensional nanonetworks can be fabricated by combining growth of ONWs by physical vapor deposition, soft plasma etching of the nanowires and conformal deposition of adamantane by RPAVD.
- Ultra-water-repellent surfaces are formed by controlling the adamantane thickness deposited on the organic nanonetwork. The organic nanonetworks delay the freezing time up to 80 minutes.
- Anti-freezing properties of the adamantane can be applied also to metallic substrates. The degree of coverage of these substrates and thickness of the adamantane controls the anti-freezing behaviour, the thicker the film the higher the coverage of the metal and therefore the longer the freezing time delay.
- Nanocomposite films have been fabricated from the simultaneous copolymerization of adamantane and DCM laser dye. The films are thermally and chemically stable at temperatures higher than the corresponding to the sublimation of the precursors.
- Luminescent thin films have been obtained by the remote plasma assisted vacuum deposition of adamantane and DCM laser dye. The



---

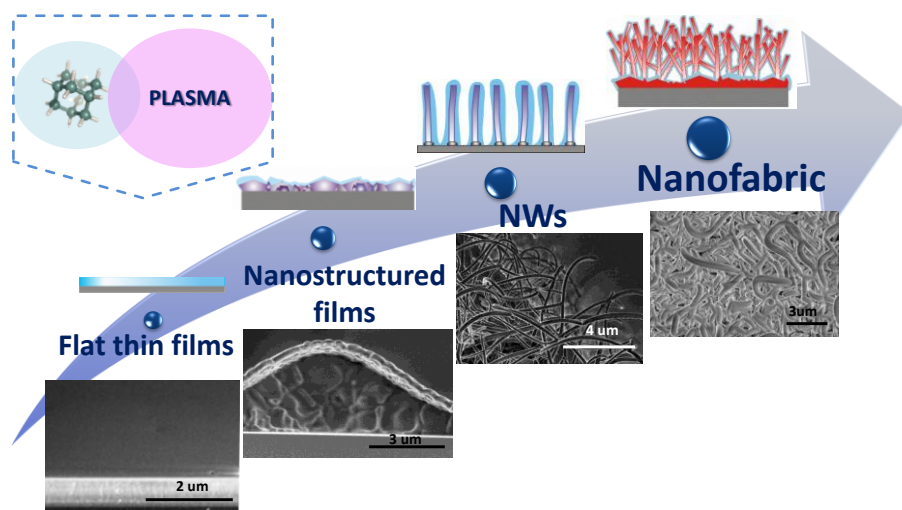
optical properties of the films can be controlled as a function of the dilution of the dye in the organic matrix. Thus, films with refractive indexes in the range 1.56-1.67 have been deposited.

- The films present a multicolor luminescent emission that is a function of the dilution of the dye in the range  $\lambda_{em}=507-607$  nm. The intensity of the luminescent emission is also a function of the dye dilution.
- DCM/Adamantane composite films show improved stability and mechanical properties against photoinduced sublimation as compared to pure DCM plasma films. Moreover, ASE experiments have shown positive optical gain, with a threshold  $450$  kW/cm<sup>2</sup>, in the nanocomposite material, while no ASE was detected in neat DCM waveguides.
- Distributed feedback laser emission was obtained when the remote plasma polymerization composite dye thin film was deposited on a 1D corrugated silica substrate
- Plasma treatments of pure organic nanowires induce the formation of nucleation sites along the NW length that act as centres for the growth of secondary organic nanowires in a hierarchical configuration.
- The treatment of nanowires fabricated from metal organic molecules results in the formation of hybrid metalorganic nanowires whose microstructure can be controlled by the substrate temperature and the plasma treatment duration.
- Under certain conditions, the procedure works as a template process for the development of inorganic nanowires constituted by the metal nanoparticles or the corresponding metal oxide nanoparticles corresponding to the metallic cation of the original organic molecules.

- A versatile protocol for the formation of highly porous ZnO thin films and nanowires by oxygen plasma treatment under different conditions of Zn-phthalocyanine thin films and nanowires has been demonstrated.
- The ZnPc conversion to ZnO is preferentially dominated by the geometry of the plasma and the substrate temperature during the experiments.
- Highly porous ZnO thin films with surface coverages as low as 55% can be produced by the aforementioned method. Such a reduced density yields an extremely low refractive index ( $n_0 = 1.05$ ) for an optical thickness of  $t_0 = 135$  nm. As far as we know, this is one of the lowest refractive index reported for ZnO and opens the possibility of applying these layers as antireflective coatings and in graded index multilayer systems.
- Fluorescence emission of the thin films is dominated by the exciton in the UV region.
- The exciton peak can be monitored to follow the amount of oxygen in gas phase.
- 1D nanostructure formed by a ZnPc core surrounded by ZnO nanoparticles with sizes in the range between 1.1 and 3.5 nm have been synthesized by plasma treatments.



# A 1 Adamantane RPAVD: from thin films to 3D networks



## ABSTRACT

Protective organic composite in the form of thin films completely transparent in the UV-visible region were synthesized by plasma assisted vacuum deposition method (RPAVD) from adamantane as precursor. We control the optical, compositional and microstructural properties of these films by imposing different experimental conditions: varying geometry of the substrates with respect to the plasma, pressure in the reactor, plasma source power and growth rate. Once these properties were defined, the synthesis of RPAVD materials has been extended to the nanoscale due to its interest in several applications. Adamantane RPAVD nanostructures (nanostructured films, nanowires and nanofabric) have been achieved taking the advantage of conformality property of RPAVD composites using nanostructured substrates.

## A1.1 Introduction

Adamantane ( $C_{10}H_{16}$ ) is a molecular hydrocarbon compound whose structure is relatively similar to the diamond. It has a tricyclic rigid ring structure as shown in Figure A1.1 (a).<sup>1</sup> This molecule has a high vapour pressure even at room temperature and can be easily sublimated.

In recent years, we have developed remote plasma polymerized thin films of dye molecules incorporating adamantane.<sup>2-6</sup> These previous investigations have revealed RPAVD adamantane as an optimum host matrix for the development of photonically active composite intended for the development of sensors materials due to their chemical stability and transparency in the UV-region<sup>3</sup>. In the present Thesis, the characteristics and the applications of RPAVD films fabricated from adamantane without any other molecule added have been studied in-depth. The experimental device has been designed to control the variable reactor parameters (geometry of the substrates with respect to the plasma, reactor pressure, MW power of plasma source, etc.). In this Annex, we have selected a wide range of growth conditions in order to found the differences among the fabricated adamantane RPAVD thin films. As a result of this analysis, it is evidenced that adamantane RPAVD nanocomposites provide new possibilities what are beyond in advance properties.

Thus, the reactions produced between plasma (in this case, argon plasma) and precursor during the deposition can influence in the ultimate thin films. On another side of the process, we have also performed a qualitative analysis of the deposition system by mass spectrometry. The objective was to identify the produced compounds into the reactor by dosing adamantane vapour to argon plasma under different experimental conditions.

Finally, the last part of this annex is focused on the synthesis of RPAVD nanostructures. The main property allowing the fabrication of these nanostructures is the conformal growth RPAVD materials on the substrates.

Thus, we have achieved the growth of adamantane RPAVD nanostructured films as well as nanowires and as a last resort, nanofabrics, using organic nanostructures as substrates. Some advantages and applications of the adamantane RPAVD nanostructures have been displayed throughout this Thesis. The conformality is a common property of all RPAVD materials. We add some cases of nanostructures by RPAVD using other precursors. These results involve an important accomplishment in RPAVD since they entail the combination of properties of RPAVD films and nanostructures.

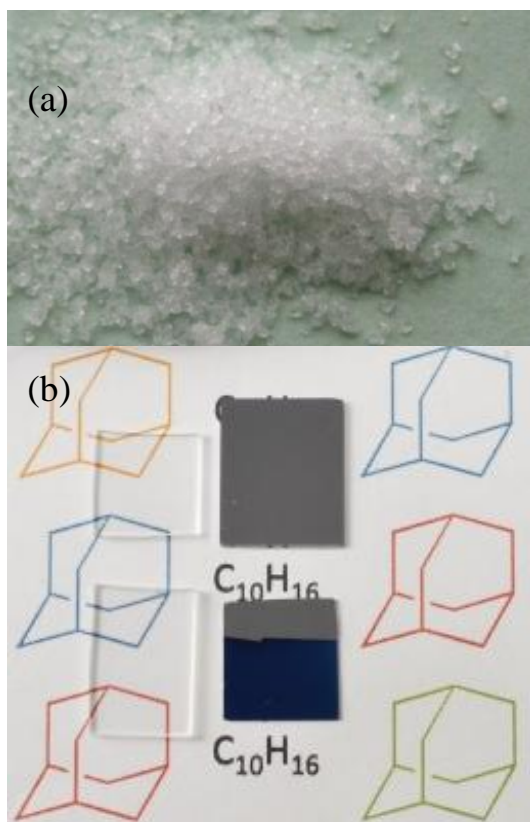


Figure A1.1. Adamantane precursor and RPAVD thin films on regular substrates – Images of (a) adamantane solid precursor, (b) adamantane RPAVD films on fused silica and silicon (100) substrates (below) and fused silica and silicon (100) substrates as references (above).

## A1.2 Experimental Setup

### *\*Thin film preparation*

The plasma deposition process is carried out in a remote configuration by sublimating adamantane (Aldrich) in the downstream region of an inert (Ar) microwave ECR plasma. The characteristics of the plasma reactor have been described in Chapter 1. The vapour pressure of adamantane is continuously dosing into the chamber by heating the external adamantane container. The temperature of dosing line is held at 65 °C while the container of adamantane is heating to 32, 37, 40, 43 °C according to the desired thin film deposition rate on the substrates, 0.1, 0.2, 0.3 and 0.4 A·s<sup>-1</sup>, respectively. The thickness of the films (range 90-500 nm) and the evaporation rate were monitored by using a quartz crystal monitor placed beside the sample holder in the deposition region. Pressure conditions are established among 10<sup>-1</sup>-10<sup>-3</sup> Torr and MW power of plasma source was varied in the range 90-270 W. The thin films have been deposited on polished fused silica plates (1 mm thick), silicon (100) substrates and gold (100 nm) coated silicon wafer (100) (Aldrich).

The fabrication of the films was carried out at two different distances between sample holder and plasma source. In addition, there are also two possible positions on the sample holder respect to the plasma source for the substrates where the film is synthesized, in front of the plasma, and back to the plasma. In summary, we studied four cases corresponding to two different distances between the sample holder and the plasma source (4 cm; 17 cm) in combination with two positions on the sample holder for the substrates (front and back). Figure A1.2 shows a diagram with the four deposition geometries analysed in the present Annex. The four types of samples fabricated in the four selected geometries are denominated samples A, B, C, D. The experimental protocol of samples A, B, C and D has been chosen to enable a wide variety of



different interactions of the sublimated adamantane molecules with the plasma species (from lowest and highest interaction) during the preparation of plasma polymeric adamantane thin films.

The nanostructures adamantane RPAVD were fabricated under geometry C conditions at pressure of  $10^{-2}$  Torr and 150 W for the MW source. We used organic nanowires grown by PVD as support for RPAVD adamantane. The fabrication of these organic nanostructured substrates has been described in Chapter 1.

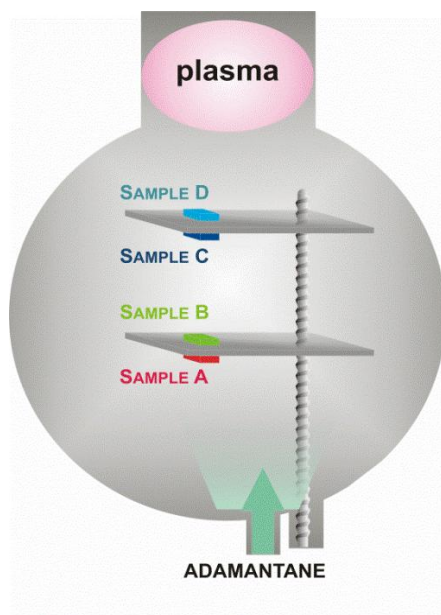


Figure A1.2. Location of substrates with respect to the sample holder and the plasma source - (a) the sample holder is located 17 cm from the plasma source while the substrates are back to the plasma source, (b) the sample holder is located 17 cm from the plasma source while the substrates are situated in front of the plasma source, (c) sample holder is located 4 cm from the plasma source while the substrates are back to the plasma, (d) sample holder, 4 cm from the plasma; the substrates, in front of the plasma.

*\*Thin film characterization*

The transmission spectra in the UV-visible region of thin films are recorded in a Varian Cary 100 spectrophotometer for samples deposited on fused silica slides. The optical properties of the films and the thickness are measured with a variable angle spectroscopic ellipsometer (VASE) from J.A. Woollam Co.,Inc.

The analysed spectral range is 400-900 nm and the measurements are performed at 60°, 65° and 70° angles of incidence. Transmission and depolarization data were analysed assuming the Cauchy dispersion law and an ensemble of three Lorentz oscillators. Tapping atomic force microscopy (AFM) measurements are carried out with a Cervantes AFM system from NANOTEC using commercial AFM tips of silicon (radio < 10 nm, dimensions: 125  $\mu\text{m}$  x 35  $\mu\text{m}$ ,  $f_0 = 325$  kHz,  $k = 0.6$  N/m; from MikroMasch). X-ray photoelectron spectroscopy (XPS) is recorded on an ESCALAB 210 spectrometer that was operated at constant pass energy of 20 eV. Nonmonochromatized Mg K $\alpha$  radiation was used as excitation source. Atomic ratios and surface concentrations were quantitative determined from the area of C1s peaks. Field emission scanning electron microscopy (FESEM) micrographs are obtained with a HITACHI S4800 microscope for samples deposited on silicon (100). Fourier transform infrared (FTIR) spectra were recorded in a Jasco 6200 spectrometer operating in specular reflection mode for samples deposited on gold (100nm) coated silicon wafer. Visible RAMAN spectroscopy in the samples deposited on silicon (100) substrates was performed to complete the information about vibrational modes achieved by FTIR. Furthermore, adamantane fragmentation analyses have been performed in situ by mass spectrometry by a Hiden Analytical Limited MASsoft mass spectrometer. The mass spectrometer was annexed to the deposition reactor to performance measurements under two acquisition modes of operation: Residual Gas Analysis (RGA) mode, by which

the internal ion source of the mass spectrometer is used to provide positive ions for mass analysis, and Secondary Ion Mass Spectrometer (SIMS) Positive Ion mode, through which external-generated positive ions in the reactor are analysed by the mass spectrometer.

Thermal stability of the films was analysed in a tubular oven in argon flow by heating the samples up to 250 °C during 1h. Solubility tests were conducted in water and toluene, for a period of 2 h. After each immersion test, the films were dried in flowing nitrogen during 1 h.

### **A1.3 Results and discussion**

Remote plasma assisted vacuum deposition process involves the condensation and surface reaction of reactive fragments of molecule to form plasma polymeric thin films. In this process, the fragmentation of molecule is not complete and a percentage of integer molecules are also embedded within the solid matrix. The number of non-fragmented molecules is reduced when the plasma interaction is more effective. Some general structural characteristic has been previously proved by UV-vis spectroscopy, FT-IR and other techniques, and exploited in several systems.<sup>1-8</sup> The results presented in this Annex are divided in three subsections. The first subsection includes the complete study of the characterization of adamantane RPAVD thin films fabricated under different experimental growth conditions. The modification of experimental parameters can involve structural differences in the growth of the film, and therefore, differences in their properties. The second subsection is focused in the processes arising while the deposition is taking place. The qualitative analyses of the positive ions produced in the reactor at the deposition conditions have been examined. The last subsection comprises the description of the RPAVD method for the synthesis of RPAVD nanostructures.

### A1.3.1 Characterization of RPAVD thin films

#### A1.3.1.1 Effect of geometry on Adamantane RPAVD thin film synthesis

The interaction of the sublimated adamantane molecules with the plasma discharge species during the synthesis follows the sequence sample A < sample B < sample C < sample D, as was specified in experimental section. The samples have been deposited on Si (100) under pressure and MW plasma source power conditions of  $10^{-2}$  Torr and 150 W.

##### *\*Topography of thin films*

The samples type A, B, C and D on Si (100) substrates have been investigated by atomic force microscopy (AFM) technique to assess the surface topography of adamantane plasma polymeric films. These analysis indicate that the films are very flat, with estimated RMS roughness values in the order of 0.2-0.3 nm for < 100 nm thick films, or even 0.6 nm for thicker films (sample D; 600 nm aprox.). These aforementioned low roughness values are similar to the substrates (RMS of Si (100) < 1 nm) and have also been found in other previous polymeric thin film deposited in a similar experimental setup.<sup>3-6</sup> Table A1.1 visualizes the obtained results for adamantane thin films A, B, C and D from the surfaces images and line profiles (Figure A1.3) of the prepared samples. In view of these results, the geometry of the substrate with respect to the plasma plays a key role in the fabrication of the thin film. Samples grown on top-geometry configuration (C and D) show microstructures more homogeneous than samples placed below (A and B). The analysis of different zones of the samples A and B (images not shown) exhibit some isolated clusters of material and higher grain sizes, even by analysing more homogeneous zones of the samples (see grain sizes in Table A1.1 and lines profiles in Figure A1.3). These agglomerations could be caused by material not fragmented since samples A and B have been

located further away from the plasma source during the deposition.

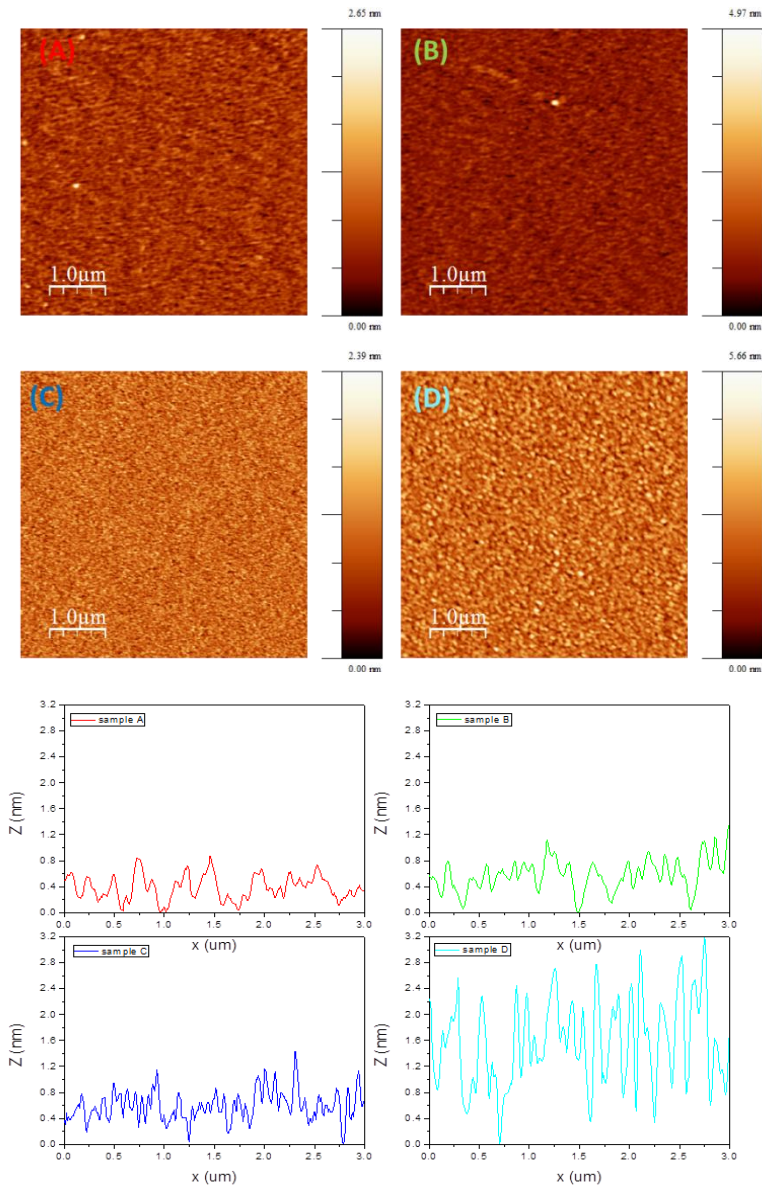


Figure A1.3. AFM micrographs and profiles of adamantane RPAVD samples grown at different geometries – AFM micrographs of the thin films grown at the geometries described in Figure A1.2 (above). The profiles have been measured on each micrograph.

Sample	Thickness (nm)	Grain size (um)	RMS (nm)
A	50	0.26	0.19
B	91	0.34	0.25
C	91	0.14	0.25
D	585	0.18	0.62

Table A1.1. Thickness, grain size and RMS of adamantane RPAVD thin films grown on silicon (100) at different geometries – Grain size and RMS value obtained by analysis of AFM images of samples A, B, C and D. The thickness was measured by ellipsometry.

On the other hand, there are only slight differences of thickness and RMS value among samples grown below (samples A and B) while thickness and RMS value among samples that are fabricated on top-geometry (samples C and D) differ significantly. Thus, in the same growth conditions, samples D present higher thickness and roughness than the rest of the samples.

#### *\*Optical Characterization of thin films*

Figure A1.5 exhibits UV-visible transmission spectra of the four types (A, B, C, D) of adamantane plasma-polymerized film deposited onto substrates of fused silica. The spectrum of the fused silica substrate is also shown for comparison. The spectra verify that the sublimation of the adamantane at the same time in four different zones of the plasma chamber produces transparent polymeric films in the visible and near infrared regions showing the typical interference patterns due to different refractive index and thickness between the substrate and film. This behaviour is more evident in sample D which present higher thickness of about 600 nm, in the face of the rest of samples which thicknesses are about 50 nm (sample A) and 100 nm (samples B, C). Thus, all samples with thickness lower than 100 nm (samples A, B, C) seem transparent for wavelengths higher than 300 nm independently of geometry conditions. However, a decrease on transmittance is observed in sample D at lower

wavelengths. These thin films absorptions in the absorption in the high energy region of the visible spectrum can be attributed to the presence of conjugated bonds typically observed in cross-linked polymeric structures obtained by plasma polymerization of organic precursors, producing the yellowish colour typical of hydrocarbon plasma polymers.<sup>5</sup>

The samples fabricated in low-geometry are less interesting for this work because of the rough and inhomogeneous microstructure studied in the previous section and not so good relationship growth rate-transparency. The Figure A1.5 (b) shows spectra corresponding to samples deposited on top-geometry (samples type C and D) where the distances plasma-samples were slightly varied from those initially imposed (0.3 and 2.0 cm). If we focus on these samples, it is remarkable that the parameter distance plasma-sample is more significant in samples directly exposed to the plasma than the samples grown back to it. The spectra for the sample type D deposited closer to the plasma (0.3 cm) shows less transparency in the UV region and greater number of interference maxima and minima.

Finally, Figure A1.5 (c) shows the spectra for samples C and D that were fabricated at RT and 90 °C in order to verify the influence of the temperature of substrates in the deposited films. It is apparent that increasing temperature has a greater influence in the samples that are not directly exposed to plasma. The high temperature complicates the adhesion of the adamantane to the substrates; therefore the thin film has a lower thickness. In addition, they present the inconvenience of a lower transparency.

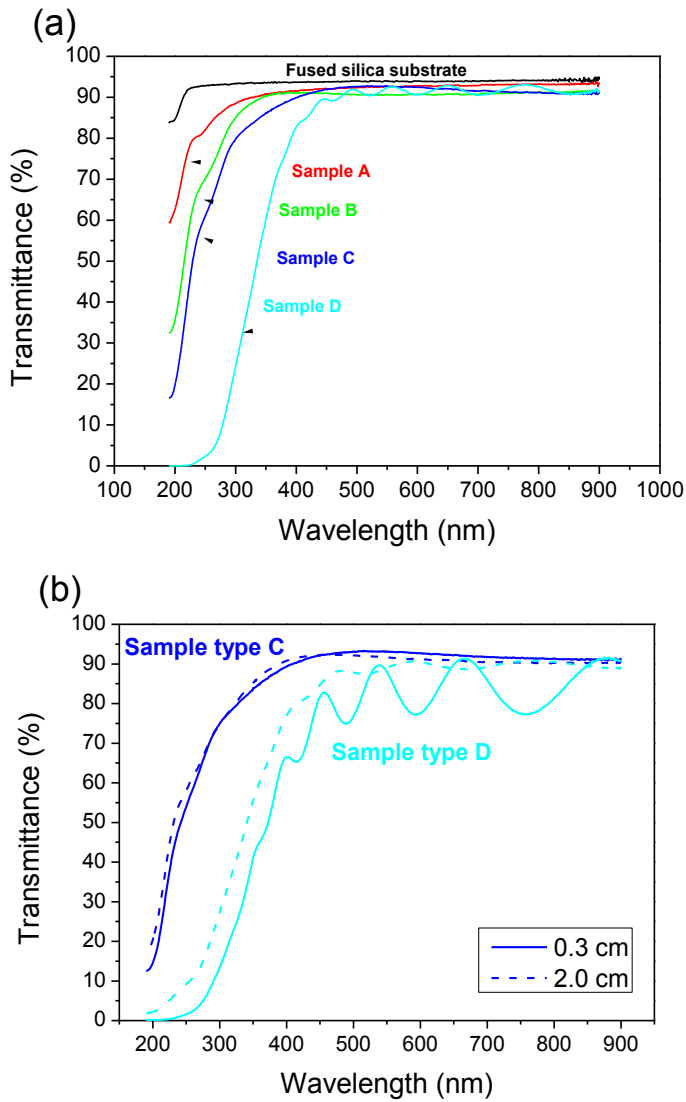


Figure A1.4. UV-visible spectra of transparent adamantane RPAVD thin films at different geometries – UV-visible transmittance spectra of adamantane RPAVD thin films grown simultaneously in: (a) the four different chamber geometries showed in Figure A1.2, (b) at top-geometry (C-D) varying slightly the distance plasma-substrate.



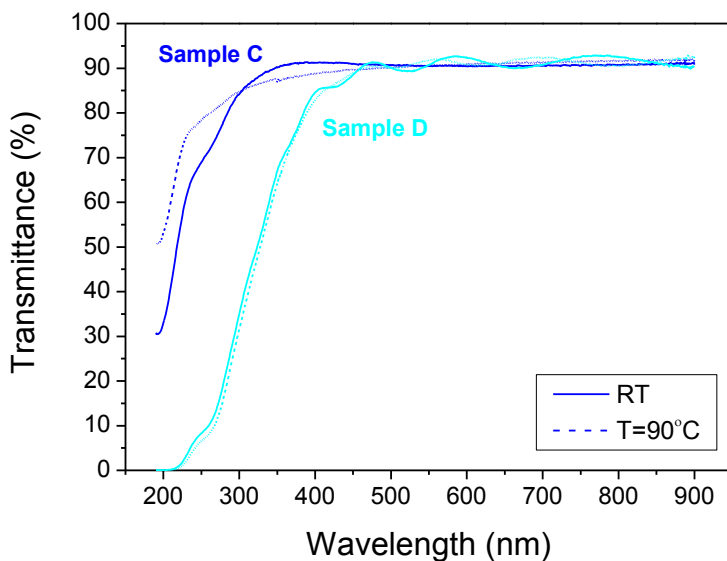


Figure A1.5. UV-visible spectra of adamantane RPAVD thin films at different temperatures and geometries - UV-visible spectra of adamantane RPAVD thin films above RT temperature at top-geometry (C-D) and RT and 90°C.

The type C of adamantane RPAVD samples is a suitable candidate overlooking optimal conditions in producing thin films for optical applications due to their topographic and optical characteristics at RT: homogeneity, low grain size, low roughness, controlled growth rate and transparency.

The present Thesis shows several applications of the adamantane thin films fabricated at the geometry of sample C. However, we will continue evaluating the characterization of adamantane thin films grown under different geometrical conditions in the next sections in order to establish the differences among them.

### *\*Chemical composition of thin films*

The surface composition of adamantane thin films types C and D have been determined by X-ray Photoelectron Spectroscopy (XPS) deposited on Si (100) under mentioned conditions. The survey XPS spectra of the samples C and D have been measured (spectra not shown). The polymerized adamantane films are composed of C, O and N atoms. The results are summarized in Table A1.2 where the atomic percentages are presented. It is observed lower percentage of carbon in the sample deposited from direct exposure to plasma (D) than in the sample deposited back to the discharge (C). Both samples contain oxygen even if this element is not present in the adamantane monomer, and no oxygen flow is added to the discharge. A higher amount of oxygen is noticed for samples D in comparison with the film growth under geometry D (C: 8.3%; D: 14.6%). Oxygen enrichment is a common phenomenon in most plasma polymerized organic materials. Its origin can be post deposition reactions of the samples exposed to the air or direct incorporation of residual oxygen from the reactor during the deposition.<sup>3, 9-12</sup> The incorporation of nitrogen into the sample occurs similarly.

Sample	C1s (%)	O1s (%)	N1s (%)
C	90.1	8.3	1.6
D	76.7	14.6	8.7

Table A1.2. Relative atomic concentration of oxygen and carbon on adamantane RPAVD grown at different geometries by XPS. – C1s, O1s and N1s relative surface concentration on samples grown at geometries C and D.

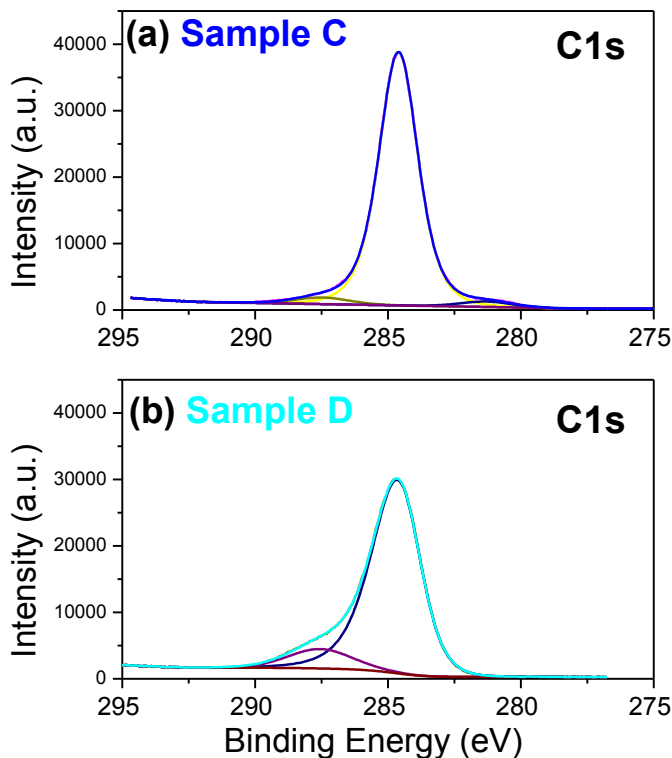


Figure A1.6. XPS spectra of C1s signal of adamantane RPAVD thin films grown at different geometries – Fitted C1s signal of adamantane into different components for a sample type C (a) and D (b).

Figure A1.6 shows fitted C1s spectra XPS corresponding to the survey of the samples C and D. The fitting procedure enables a semiquantitative evaluation of the relative concentration of carbon functional groups in the surface of the films. C1s signals obtained can be divided into several components due to different types of carbon-carbon, carbon-oxygen and hydrogen bonds in the thin film. The position of the individual components has been taken from previous works of plasma polymerization.<sup>13</sup> Both spectra are characterized by an intense peak at around 285 eV due to C-C and C-H bonds. It also presented a defined shoulder at 288 eV which is typical of the presence of C-O and C-N bond structures in the film. The relative intensity of the shoulder is

significantly smaller for the sample C which shows an additional slight peak at around 281 eV. Thus, the C1s spectrum of sample C is more symmetric, confirming the relatively small oxygen content in this sample. While the relative high intensity of the shoulder at 288 eV in the sample D indicates that the concentration of C-O and C-N groups is rather abundant in this case.

The FTIR and RAMAN spectroscopy examination of the adamantane thin films provide important information about the chemical bonds and functional groups constituting the film structure. Hence, the polymeric character of the films was completed by these analyses. Figure A1.7 shows the normalized FTIR spectra of an adamantane plasma polymerized films. To record these spectra, it is necessary a thickness in the range at least of 100 nm to have enough sensitivity. Assignment of the bands in the FT-IR spectra has been done according to the bibliography.<sup>1, 6, 12, 14, 15</sup> Spectra recorded for sublimated adamantane molecules and remote plasma polymerized adamantane film have been reported previously in some works on perylene plasma polymer.<sup>3</sup> Both spectra are dominated by two strong bands, at around  $2900\text{ cm}^{-1}$ , that are attributed to C-H vibrations, but with an appreciable broadening for the plasma polymer. Thus, these vibrational features in plasma deposited sample have a tendency to a single broad band at the same time that the plasma-molecules interaction has been higher during the deposition (see Figure A1.7 (a)). Another band at around  $1500\text{ cm}^{-1}$  due to C-H vibrations is present in all cases. In addition, other less-intense bands due to C=C, -C=O and -OH stretching vibration are observed at about 1400, 1700 and  $3400\text{ cm}^{-1}$ . Such bands due to -C=O and -OH groups respond to the aforementioned phenomenon in plasma deposition processes since the residual oxygen and/or water molecules in the chamber that become plasma activated and react with the fragments of the monomer and post deposition reactions of trapped radicals and  $\text{O}_2$ . In agreement with the XPS results, these contributions are greater in the sample D.

Position (cm <sup>-1</sup> )	Group	Vibration mode
3400	O-H	Stretching
2940	C-H	Stretching, aliphatic groups
2860	CH <sub>2</sub>	Stretching, aliphatic groups
1466	CH <sub>2</sub>	Scissors
1700	C=O	Stretching in aliphatic groups
1450-1600	C=C	Stretching in aromatic ring system

Table A1.3. Raman spectroscopy peak positions (cm<sup>-1</sup>) – Raman peaks assignments for the adamantane RPAVD samples.<sup>15</sup>

In Figure A1.7 (b), visible RAMAN spectra show the comparison among adamantane powder and remote plasma polymeric films deposited at geometries C and D. In general, an amorphous carbon can have any mixture of sp<sup>3</sup>, sp<sup>2</sup>, and even sp<sup>1</sup> sites, with the possible presence of up to 60 at.% hydrogen.<sup>16</sup> The Raman spectra of carbons show several common features in the 1000–2000 cm<sup>-1</sup> region. Two basic common features are observed around 1350 and 1600 cm<sup>-1</sup> for the visible excitation, called G and D peaks. The G and D peaks are due to sp<sup>2</sup> sites only. The G peak is due to the bond stretching of all pairs of sp<sup>2</sup> atoms in both rings and chains. The D peak is due to the breathing modes of sp<sup>2</sup> atoms in rings.<sup>17</sup> However, it was demonstrated the indirect influence of the sp<sup>3</sup> content on increasing G position. The experimental visible Raman spectra on amorphous carbons is interpreted using a phenomenological three-stage model.<sup>16</sup> The most intense band in the spectrum of the adamantane powder around 1230 cm<sup>-1</sup> does not appear in adamantane polymerized samples C and D. The peaks G and D are presented in both samples, but the bands are much broadened for the sample D than C. This band broadening has also been observed in FTIR spectra. The spectrum shape of sample D indicates a greater

bond disorder than in sample C. The band from adamantane powder at  $1440\text{ cm}^{-1}$  is observed in the sample C, while it disappears for sample D.

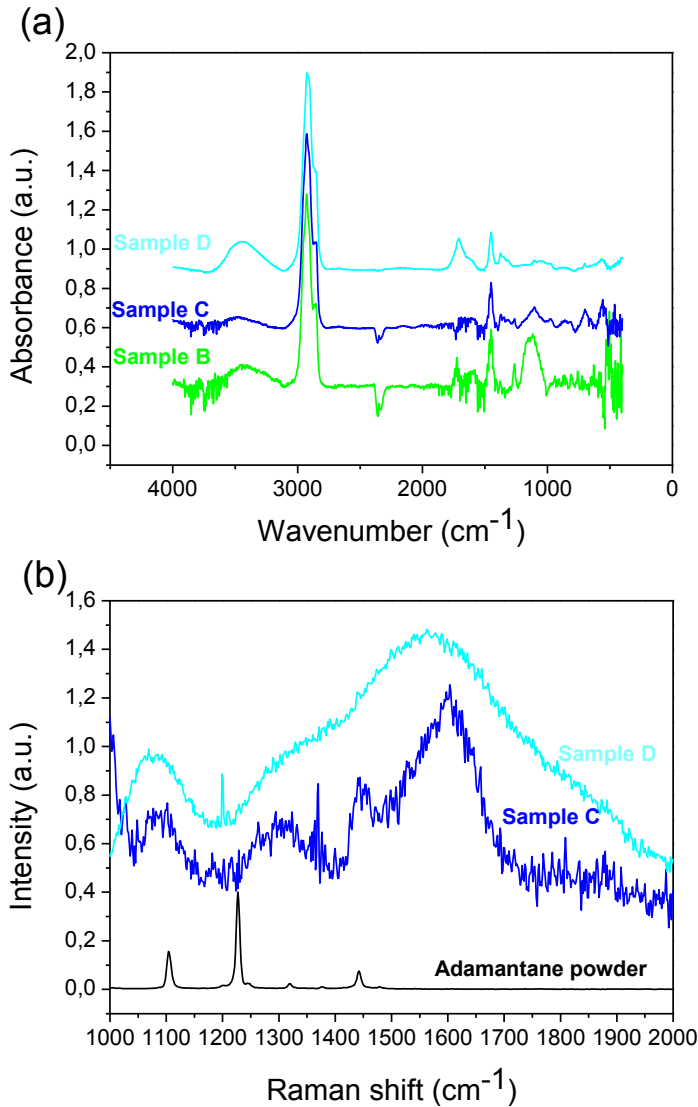


Figure A1.7. FTIR and visible RAMAN spectroscopy of adamantane RPAVD thin film at different geometries - (a) FTIR spectra for samples A,B;C ;D. (b) visible RAMAN spectra of samples C and D

The XPS, FTIR and RAMAN analyses of the polymeric thin film are congruent with a cross-linked structure resulting from the fragmentation of the adamantane molecules during the film growth. The cross-linking is apparently greater in the case of the samples growth under geometries more exposed to the plasma. This solid polymeric character of the thin films provides thermal and chemical stability in air and insolubility in organic solvents. Despite the high cross-linking degree observed in sample C, plasma is softer and less effective than in sample D. Thus, position C allows the use of sensitive substrates as paper, polymers or organics nanostructures.

#### **A1.3.1.2 Effect of Pressure, Power of MW plasma source and growth rate on Adamantane RPAVD thin film synthesis**

The RPAVD reactor supplies a very wide range of experimental possible conditions for the growth of the polymeric material, as discussed in the experimental setup section. Previously, it has been proved that the geometry of sample holder with respect to the plasma influences the growth and the resulting materials. Others experimental conditions such as pressure, MW power and growth rate can potentially affect the cross-linking degree of the polymeric thin film and consequently the material properties. A study of a set of samples in geometries close to C at different growth conditions selected in the reactor and thickness is presented in Table A1.4. The objective of this study was to achieve the conditions of the polymerization degree for adamantane thin films providing transparency in UV-range, chemical and thermal stability and insolubility in solvents.

Sample	Sample-plasma distance (cm)	p (Torr)	P (W)	Growth rate (Å/s)	Thickness (nm)
RPDA-1	1.8	$10^{-2}$	150	0.2	82
RPDA-2	1.8	$10^{-2}$	240	0.3	102
RPDA-3	1,8	$10^{-3}$	240	0.3	116
RPDA-4	0.3	$10^{-2}$	150	0.2	164
RPDA-5	0.3	$10^{-3}$	240	0.2	165
RPDA-6	1.8	$10^{-2}$	240	0.4	290
RPDA-7	3.8	$10^{-2}$	150	0.2	395

Table A1.4. Experimental growth conditions of a set of samples of adamantane RPAVD films at geometry type C – The experimental parameters of growth are sample-plasma distance, pressure, MW source power, growth rate and the thickness of the films.

In Figure A1.8 (a) are plotted UV-visible transmission spectra of the set of adamantane RPAVD samples. Fused silica spectrum is included in the figure as reference. The spectra define a very flat high transmittance in the spectral region extending from 300 to 900 nm for samples of up to thickness at around 200 nm while a shorter transparent spectral region is observed for thicker samples (400-900 nm). The transmittance decreases in the RPAVD thin films showing a broad absorption (at about 270 nm) that is not noticeable in fused silica substrate spectrum. Such absorption in the UV region can be attributed to the presence of conjugated unsaturated bonds in the film because of adamantane are not completely fragmented.<sup>3</sup> This partial fragmentation could confirm that the plasma in RPAVD is soft. It represents an advantage in the use of sensitive substrates that are not damaged for the plasma.



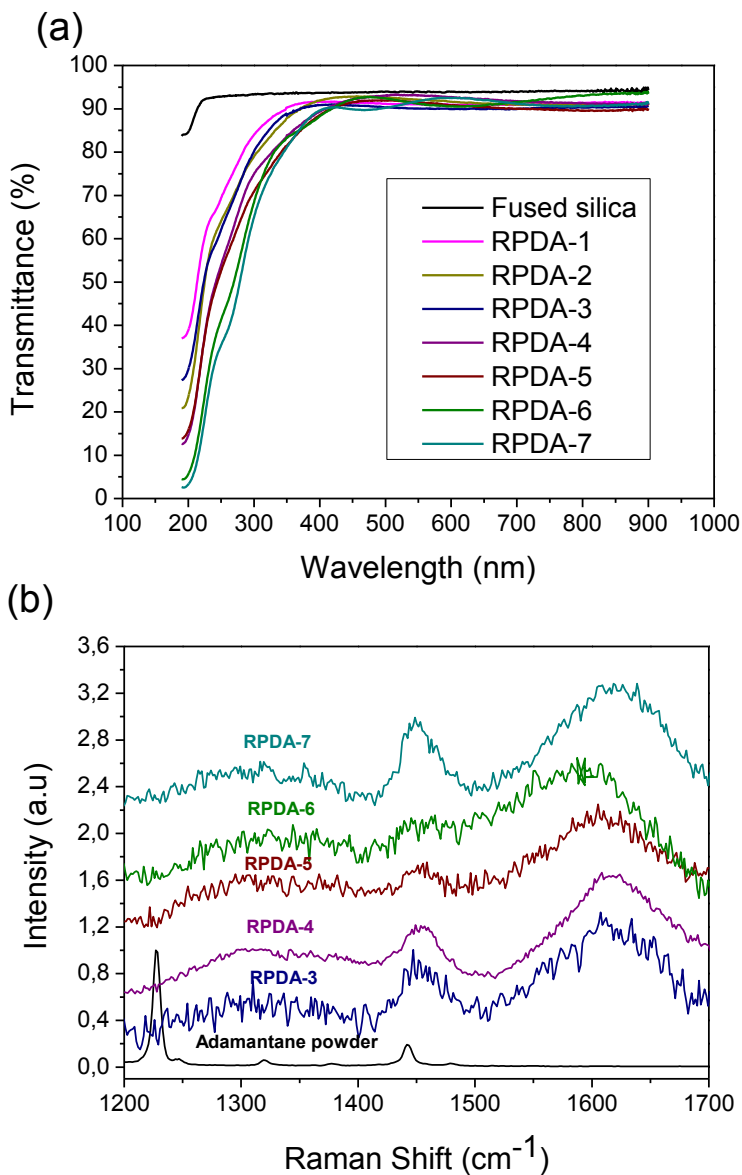


Figure A1.8. Spectroscopy of RPAVD thin film deposited under different experimental parameters at geometry type C - (a) UV-visible transmittance and (b) RAMAN spectra of samples which growth conditions are described in Table A1.4. The measurement of fused silica in (a) and adamantane powder in (b) have been included as references respectively.

Comparing samples RPDA-3 and RPDA-2 demonstrate that only varying the pressure between  $10^{-2}$  Torr- $10^{-3}$  Torr does not show significant influence on the spectrum. Nevertheless, increasing power of MW plasma source and growth rate (see RPDA-1 vs RPDA-2 and RPDA-4 vs RPDA-5) leads to narrower range of transparency in the films. Finally, the transmittance observed for RPDA-6 and RPDA-7 are similar in spite of the difference between their thicknesses. The experimental parameters during the deposition of RPDA-6 (sample holder closer to the plasma source, higher power of MW source of plasma, higher rate) result in more cross-linked materials.

RAMAN spectra in Figure A1.8 (b) show adamantane power as a reference and remote plasma polymeric films. There are not apparent differences among the spectra shape of adamantane RPAVD thin films fabricated by varying experimental parameters such as pressure and MW power. Only it is observed the expected broadening of bands typical in plasma polymerization. The peaks G and D are presented in all samples. A band at  $1440\text{ cm}^{-1}$  from adamantane molecular is also observed. Spectra sample fabricated at the greater distance from the plasma glow (3.8 cm), low growth rate ( $0.2\text{ \AA/s}$ ) and low MW power (150 W) shows more intense band at  $1440\text{ cm}^{-1}$ .

The results suggests that greater distance to the plasma, lower growth rate, lower MW power source and higher pressure lead to less cross-linked thin films.

#### **A1.3.1.3 Chemical and thermal stability of ADAMANTANE RPAVD thin film**

Previous studies have confirmed the insolubility of the films in water, ethanol and toluene solvents, as well as the thermal stability up to  $250\text{ }^{\circ}\text{C}$  in an oven under argon flow at atmospheric pressure of the RPAVD.<sup>3</sup> Adamantane RPAVD thin films resulted insoluble by immersing in the aforementioned solvents during 12 hours at room temperature. In order to find the upper thermal

limit resistance, a film was checked before and after calcination treatments on an electric plate heater at atmosphere. The UV-vis spectrum of the film shows a yellowing after the treatment at 250 °C during 1 hour.

XPS thermal evolution of an adamantane RPAVD thin film was carried out in ultra-high vacuum. Oxygen concentration decreases up to 170 °C remaining fairly constant from 170 °C to 350 °C. C-O bond structure from C1s signal gradually disappears by raising the temperature while O1s signal remains. These results indicate that two oxygen species are contributing to the signal of O1s. However, only one of them is chemically linked to C. Table A1.5 shows the thermal evolution of relative atomic concentration of oxygen and carbon functional groups in the surface of the films. Components from C1s due to carbon-carbon and carbon-oxygen bonds in the thin film have been evaluated using the same fitting model.

Temperature (°C)	C1s [C-C] (%)	C1s [C-O] (%)	O1s (%)
RT	85,5	4,8	9,6
100	90,6	2,2	7,2
120	93,6	1,2	5,1
150	94,8	0,7	4,6
170	95,6	0,4	4,0
200	95,5	0,4	4,1
225	95,9	0,1	4,0
250	96,7	0,0	3,3
350	96,5	0,0	3,5

Table A1.5. Thermal evolution of relative atomic concentration of oxygen and carbon on adamantane RPAVD by XPS – Atomic concentration of C-C and C-O bond structure from C1s and O1s signals performed at temperatures of sample holder from RT to 350°C.

### A1.3.2 Adamantane RPAVD in the reactor: effects of pressure, power of MW plasma source and growth rate on

Up to this point, the effects of the variable experimental parameters have been evaluated from the perspective of the resulting thin films, but what is happening in the reactor during the deposition? For this purpose, argon gas and adamantane fragmentation qualitative analyzes have been performed in situ by mass spectrometry under two acquisition modes of operation: Residual Gas Analysis (RGA) mode and Secondary Ion Mass Spectrometer (SIMS) Positive Ion mode by holding fixed the position of the probe. The experiments have been carried out varying the experimental conditions of pressure, MW source power and growth rate of the RPAVD adamantane thin films.

#### *\*RGA measurements*

The films are fabricated in presence of argon plasma. Thus, we measured the spectra of argon plasma under different experimental conditions as references. The mass signals in the spectra are greater by increasing the reactor pressure. Modifying the value of the MW source power applied does not produce changes in the spectrum either in intensity or fragmentation. The main peaks observed in the spectra are the peaks associated with the  $\text{Ar}^+$  and  $\text{Ar}^{++}$  at masses 40 and 20 respectively. Additionally, there were peaks at mass 2 (hydrogen), 18 ( $\text{H}_2\text{O}$ ), 28 ( $\text{CO}$ ) and 44 ( $\text{CO}_2$ ) in the spectra. Adamantane vapour in argon flow (without plasma) and adamantane plasma (without argon flow) have also been analyzed as references. In the first case, the fragmentation of the adamantane is similar to the studied in the literature (see Figure A1.9(b,c)). In addition, other fragments appear at mass 57, 40, 20 (argon), 32 (oxygen), 44 ( $\text{CO}_2$ ), 28 ( $\text{CO}$ ), 18 ( $\text{H}_2\text{O}$ ), 2 (hydrogen). The spectra were collected at three pressures  $10^{-1}$ ,  $10^{-2}$ ,  $10^{-3}$  Torr. The signal intensity remained constant in the

pressure range  $10^{-2}$ - $10^{-1}$  Torr. However, it decreased to two orders of magnitude for lowest pressure spectrum ( $10^{-3}$  Torr). Adamantane plasma (without argon) mass spectra shows low signal. The fragments are the same than in previous case except the peaks corresponding to argon (Figure A1.9 (d)).

All spectra measured under different experimental conditions of depositions of adamantane RPAVD films showed the fragments of lower  $m/z$  (27, 29, 39, 41, 53, 55, 67) due to the fragmentation of adamantane. In addition, we observed other fragments that were not shown in the fragmentation of adamantane from the literature. However, these peaks are presented in reference spectra of Figure A1.9 (b-d) and correspond to  $\text{CO}_2^+$ (44),  $\text{H}_2\text{O}^+$ (18),  $\text{H}_2^+$ (2),  $\text{CO}^+$ (28),  $\text{O}_2^+$ (32). Their intensities in the measured spectra are comparable to the higher  $m/z$  fragments. No important changes were observed in the pressure range 90-270 W. The intensity signals increase with the pressure, keeping their proportions. On the other hand, the increase of the amount of adamantane molecules in the reactor (growth rate of adamantane) by annealing the precursor at higher temperatures causes differences in the spectra gathered. Figure A1.9 (e-f) depicts mass spectra under fixed pressure and plasma power conditions ( $10^{-2}$  Torr, 150 W) at different growth rate of material. Fragments with greater  $m/z$  are more intense at highest deposition rate, while lowest  $m/z$  fragments due to adamantane smaller decrease in intensity. Moreover, the Ar intensity rises by introducing adamantane in the reactor (0.1-0.3 A/s). In contrast, this signal decreases at 0.4 A / s. We have also inquired at mass above 140, but the signal is zero from this mass range.

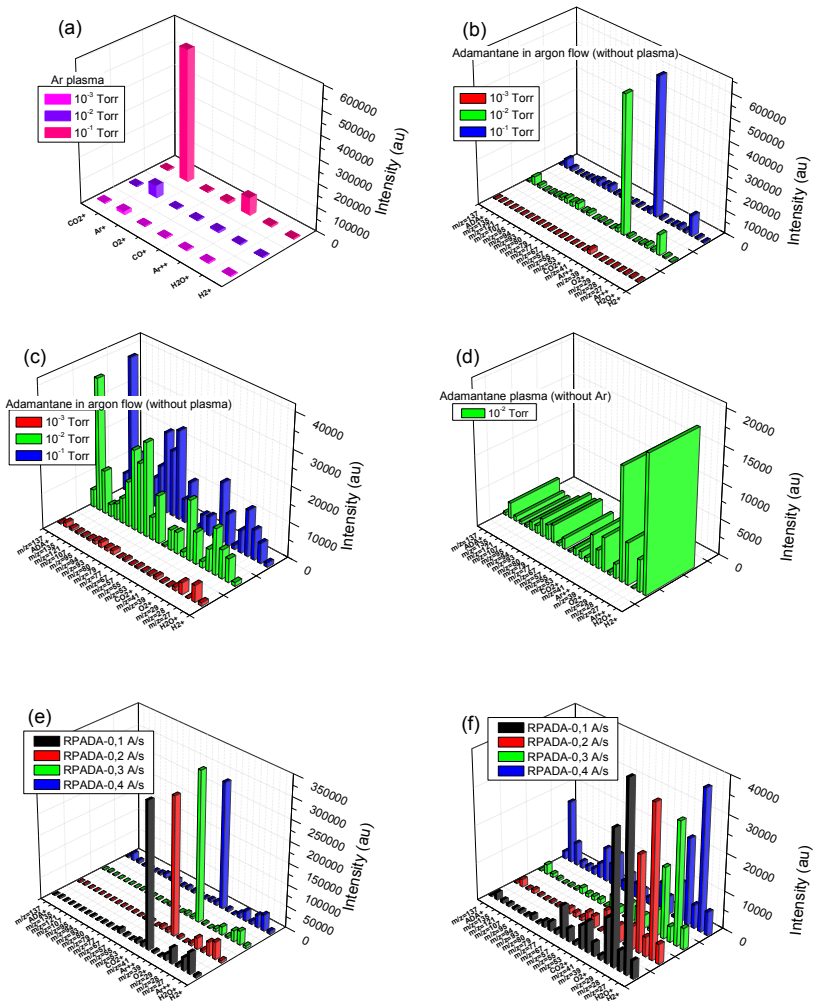


Figure A1.9. RGA mass spectrometry in the RPAVD reactor under different adamantane RPAVD experimental conditions – Mass spectroscopy of: argon plasma at three pressure values (a), adamantane in argon flow at three pressure values (b), adamantane in argon flow at three pressure values removing the argon peaks (c), adamantane plasma (d), RPAVD conditions at three growth rate values (e) and RPAVD conditions at three growth rate values removing the argon peaks (f).

**\*SIMS measurements**

The signal of positive ions in argon plasma versus mass was studied at pressures from  $10^{-1}$  to  $10^{-3}$  Torr and power of 90 to 270 W as reference. The measurements are zero in all cases. Mass 40 (Ar+) energy is gathered under different conditions of pressure and power. Figure A1.10 shows higher energies at lower pressures being zero at  $10^{-1}$  Torr. On the other side, the energy increases as the applied MW source power.

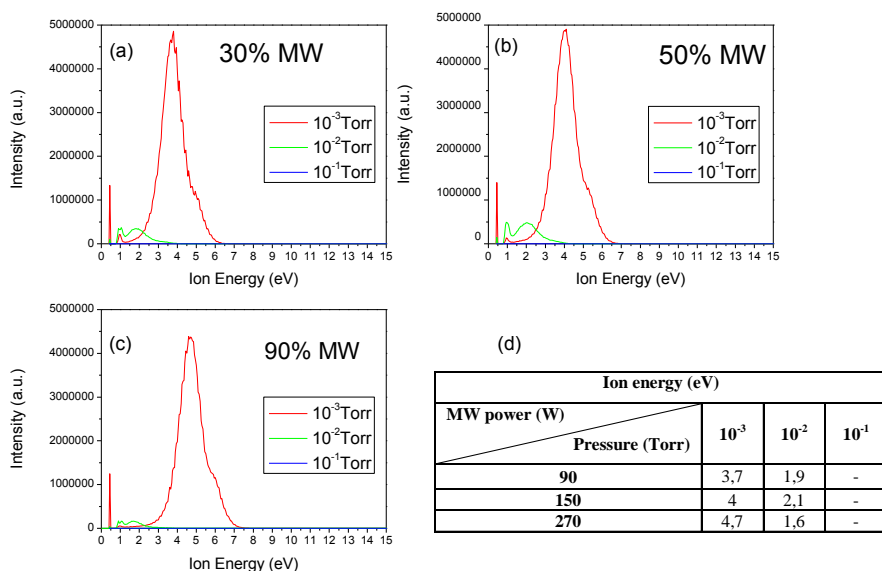


Figure A1.10. Ar<sup>+</sup> ion energy under different experimental conditions – Spectrometry of Ar<sup>+</sup> ion energy (a-c) and Ar<sup>+</sup> ion energy values (d) at pressure and MW power source values of  $10^{-1}$ - $10^{-3}$  Torr and 90-270 W.

Figure A1.11 (a) shows the mass spectrum of adamantane plasma (without argon) obtained at  $10^{-3}$  Torr (lowest pressure) and 150 W. There were not any signals under others experimental conditions. Figure A1.11 (b,d) presents RPAVD at different powers and pressures. Greater mass fragments predominate at higher pressures, while lower mass fragments increase at lower pressures. Ion mass spectra of adamantane show low intensity, especially at higher pressures. Particularly, at 150 W and pressure close to  $10^{-2}$  Torr, the intensity is almost zero, see Figure A1.11(c).

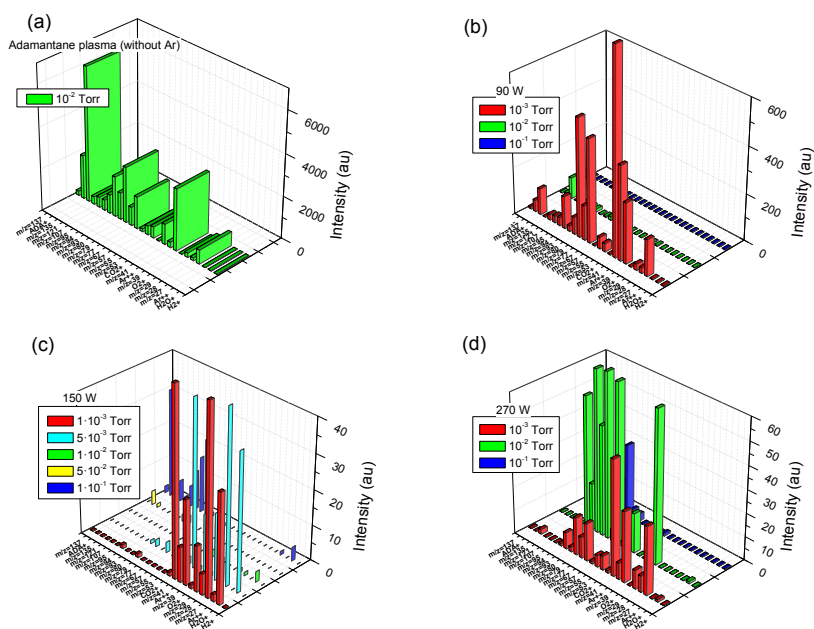


Figure A1.11. SIMS mass spectrometry in the RPAVD reactor under different adamantane RPAVD experimental conditions – Mass spectroscopy of: adamantane plasma (a), RPAVD conditions at 90 W (b), at 150 W (c) and 270 W (d) MW power source for several pressures values.



Regarding energy measurements of argon ( $\text{Ar}^+$ ) and adamantane ( $\text{ADA}^+$ ), the increment of growth rate of adamantane shifts argon peak to higher energies. Greater energies of ions argon and adamantane are observed for lowest pressures. The intensity of  $\text{ADA}^+$  signal is lower than  $\text{Ar}^+$ , and becomes absent at higher pressures, mainly at  $10^{-1}$  Torr (Figure A1.12). It is worth noting that intermediate values of pressure and MW power (about  $10^{-2}$  Torr, 150 W) show minimum energies.

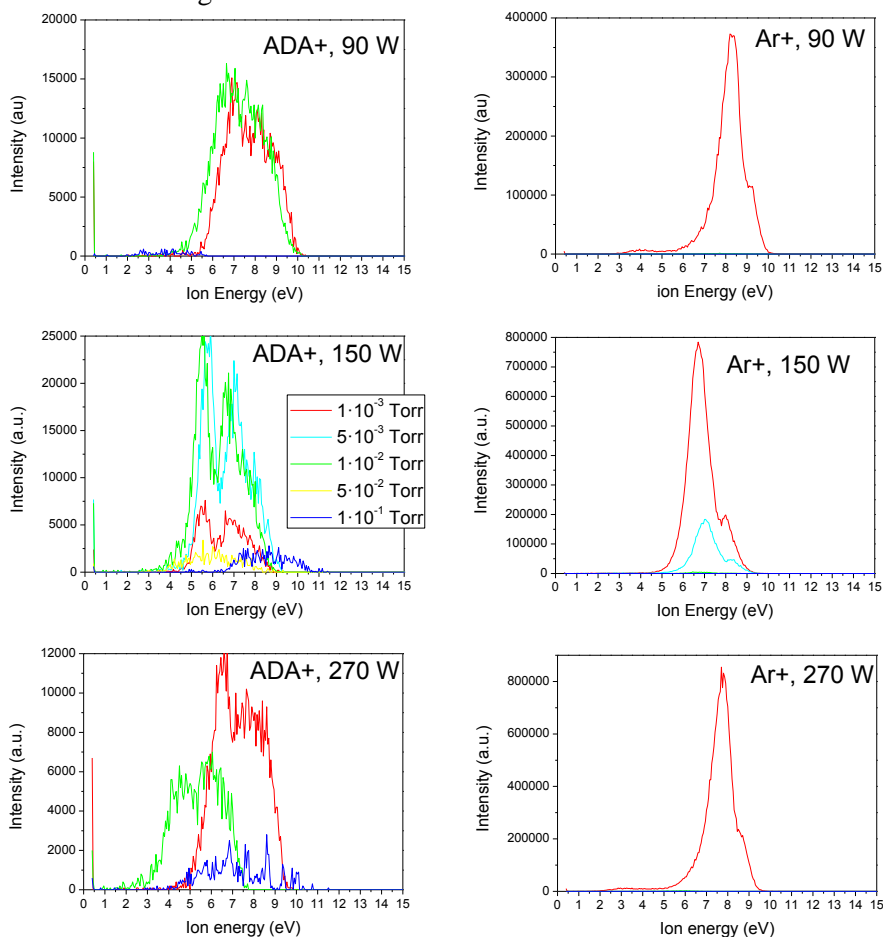


Figure A1.12.  $\text{Ar}^+$  and adamantane positive ion energies under different experimental conditions – Spectrometry of  $\text{Ar}^+$  and positive adamantane ion energies at pressure range of  $10^{-1}$ - $10^{-3}$  Torr and MW power source values of 90-270 W.

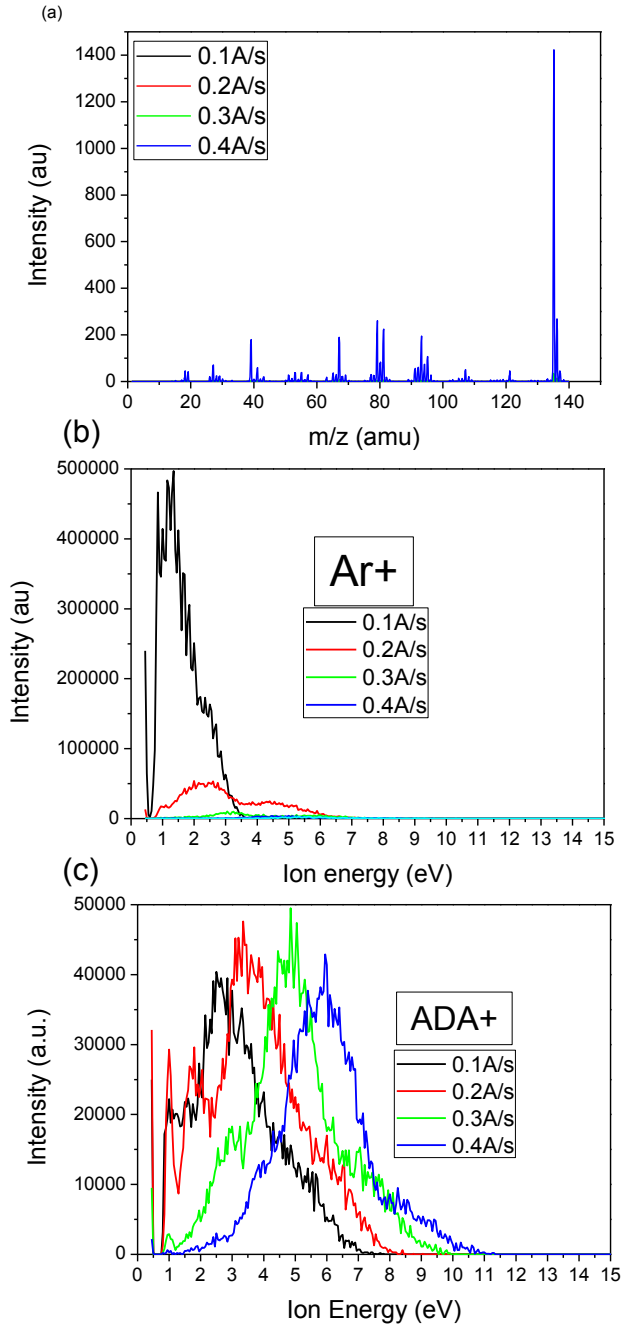


Figure A1.13. Mass spectrometry of adamantane RPAVD conditions at different growth rate – Mass spectra (a) and  $Ar^+$  (b) and adamantane positive (c) ion energies at growth rate of 0.1, 0.2, 0.3 and 0.4 A/s (10-2 Torr, 150 W)

Mass spectra under fixed pressure and plasma power conditions ( $10^{-2}$  Torr, 150 W) at different growth rate of material only are obtained for the greatest growth rate, 0,4 A/s, Figure A1.13(a).  $\text{Ar}^+$  shape spectrum of energy changes when growth rate of adamantane raises. Figure A1.13(c)  $\text{ADA}^+$  energy shifts towards higher energies with increasing the adamantane growth rate, Figure A1.13(b).

### **A1.3.3 Effect of substrate microstructure on ADAMANTANE RPAVD thin film synthesis**

Adamantane RPAVD thin films on Si (100) and quartz substrates (flat substrates without microstructure) are very stable, insoluble in water, ethanol and toluene solvents, thermally stable up to  $250^\circ\text{C}$  and have flat, continuous, regular and homogeneous microstructures, free of cracks and micro aggregates that are responsible for light dispersion (Figure A1.14). These properties are general for RPAVD thin film and were presented in Chapter 1. Taking step forward in the analysis of the material, the microstructure of the RPAVD films is quite different when the deposition takes place on substrates that are not flat in the microscale. In previous works, it has previously reported conformal plasma polymerization of 3-hydroxyflavone with adamantane on polystyrene opals<sup>18, 19</sup>. The topmost layer of the opal acted as a template for the growth of the polymeric nanostructured film with a perpendicular preferential direction of expansion and a low lateral growth. A similar behaviour is depicted by adamantane RPAVD film grown on ZnO nanorods.<sup>20</sup> The preferential growth of the polymeric material is on top of these nanostructures (Figure A1.15 (a) and (b)). The images further illustrate that the RPAVD film is covering entirely the nanorods reaching even their bases (Figure A1.5 (c) and (d)).

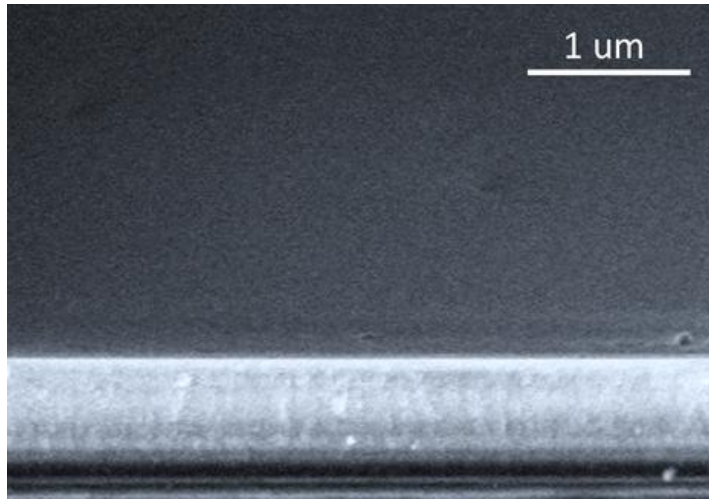


Figure A1.14. SEM micrography of surface and edge of RPAVD adamantane on flat substrate of Si (100) – Smooth grown of RPAVD adamantane film on flat substrate has been grown in position C.

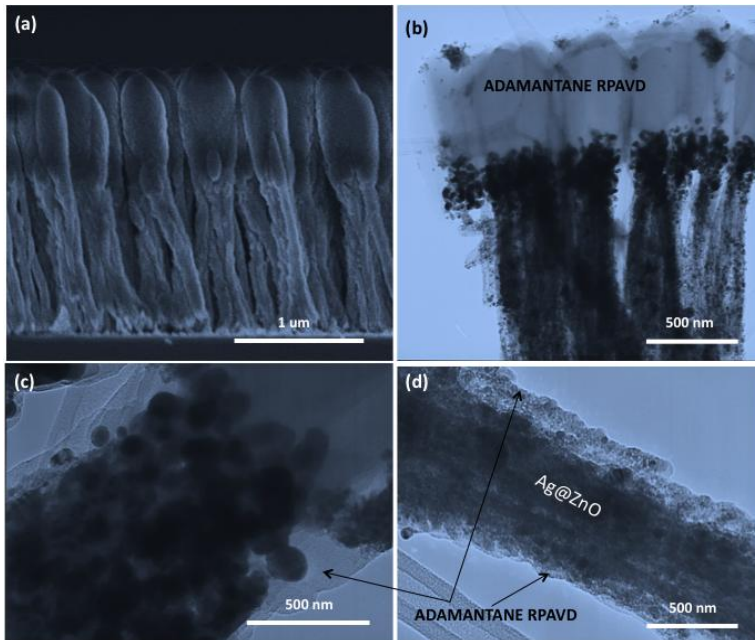


Figure A1.15. Adamantane RPAVD on nanorods of oxides - SEM (a) and TEM (b-d) micrographs of adamantane RPAVD on Ag@ZnO nanorods.

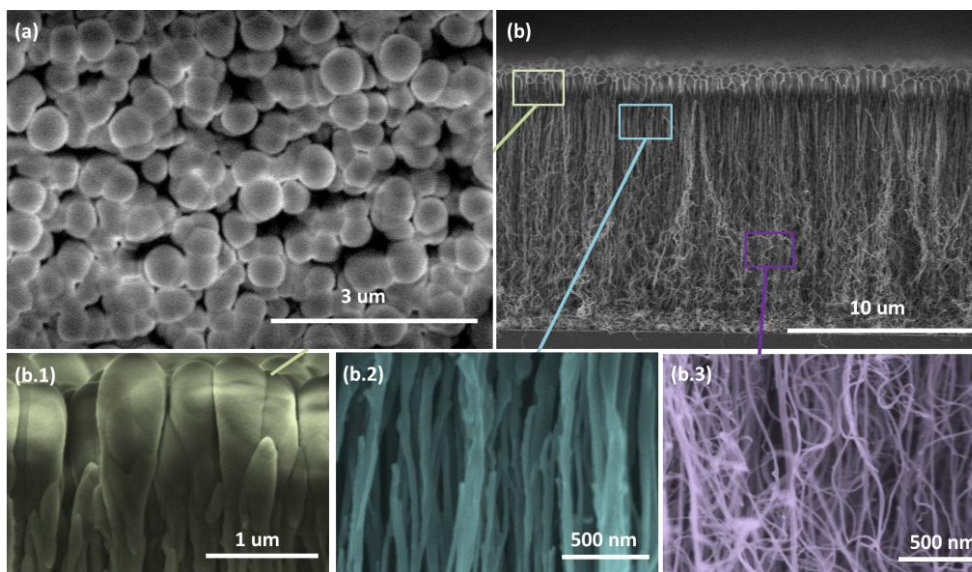


Figure A1.16. Adamantane RPAVD on carbon nanotubes - Surface view (a) and (b) cross section SEM micrographs of adamantane RPAVD on carbon nanotubes.

On the other hand, Figure A1.16 shows an adamantane RPAVD material deposited on carbon nanotubes. RPAVD adamantane have partially deposited on the outermost surface of the nanotubes (Figure A1.16 (b.1,b.2)) while the innermost areas of the polymeric material has not reached (Figure A1.16.b.3). Thus, the distance among the nanostructured features is playing an essential role in the growth of RPAVD adamantane.

In the same way, adamantane RPAVD materials on other not flat substrate were grown. Figure A1.17 (a),(b) and (c) show SEM micrographs of adamantane plasma polymerized thin films deposited on ITO, gold, and NaCl substrates. The images confirm that the RPAVD films reproduce the shape of the surface microstructure of the substrates where the thin film has been deposited. In addition, the film fills the void space among nanostructures composing the substrates. Nevertheless, the covering presents a strong dependency with: the size of substrates nanostructures, the distance among them

and their height. In summary, when the nanostructured features are separated hundred nanometers and have a height of the order of microns, the adamantane RPAVD thin film reaches the base. Hence, the materials are conformed to the surface of the substrates. On the other side, if the nanostructures have a separation of tens of nanometers and a height of tens of microns such as carbon nanotubes in Figure A1.16, the coating is partial and does not reach the substrate. This behaviour of the material has been also tested by AFM analysis technique.

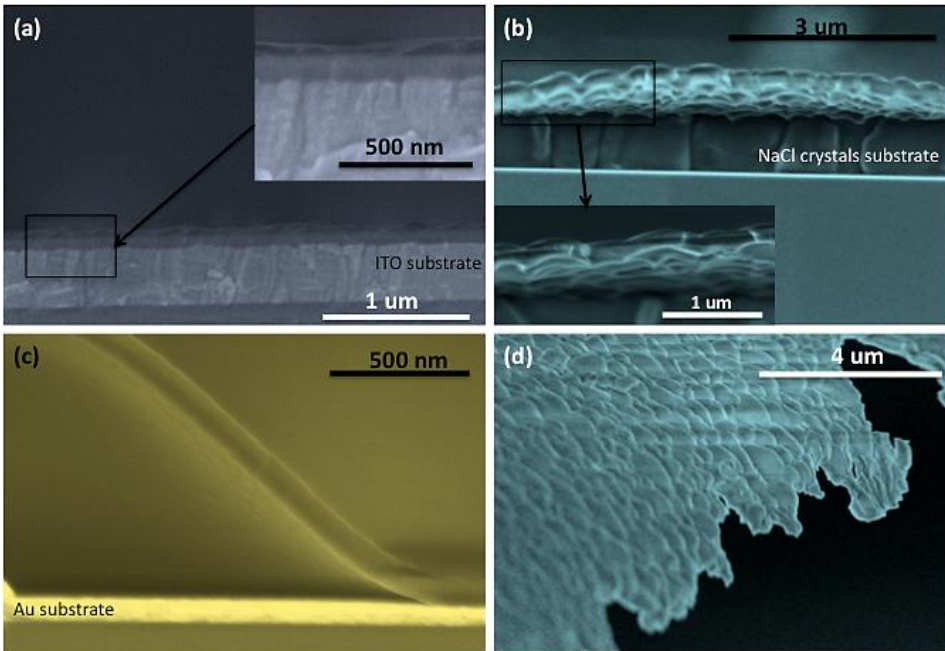


Figure A1.17. Adamantane RPAVD on rough surfaces of ITO, gold and NaCl - SEM micrographs of conformed and self-supported adamantane RPAVD on substrates of ITO (a), NaCl crystals (b) and Au (c), grown in position of the sample C. An image of adamantane RPAVD self-supported is shown in (d).

Moreover, the polymeric film can be easily separated from the substrate. This sets a way to obtain self-supported thin film of adamantane RPAVD with a desired microstructure. Figure A1.17(c) illustrates adamantane polymeric film removing from the gold substrate and Figure A1.17 (d) an adamantane RPAVD completely removed from the NaCl crystal substrate by dissolving in water and transferred to a TEM grid. The observed characteristics of adamantane RPAVD nanostructuration in the present section are applicable to all polymeric materials deposited by RPAVD.

#### A1.3.3.1 1D nanostructures of adamantane RPAVD

In the course of this Thesis we have contemplated the possibility of achieving the synthesis of adamantane RPAVD 1D nanostructures due to the importance of nanostructures such as nanowires in photonics, photovoltaic, photocatalysis, microelectronic and nanosensing applications.<sup>21-25</sup> Previous section demonstrated that adamantane RPAVD films are conformal to the substrate surface under certain conditions of separation among its micro/nanostructured motifs. Based on this property, the combination of two methodologies was proposed for the synthesis of RPAVD nanostructures: organic nanowires (ONWs) by PVD and organic composite thin films by Remote Plasma Activated Vacuum Deposition (RPAVD). The procedure consists of two steps. First, we deposit organic nanowires by physical vapour deposition, as was detailed in the Chapter 1. Secondly, these ONWs are covered with an adamantane coating grown by remote plasma assisted vapour deposition (RPAVD). By this way, we achieve supported organic core@shell structures by vacuum methodologies. SEM and STEM micrographs in Figure A1.18 show an example. Perylenediimide (2,9-dimethyl-anthra[2,1-def:6,5,10-d'e'f'] diisoquinoline 1,3,8,10-tetrone (Me-PTCDI) (from Sensient Imaging

Technologies) ONWs by PVD are forming the core of these heterostructures. It is worth to notice that organic shell also covers the substrate even high NWs density (as shown in Figure A1.18 (b)). The studies of adamantane RPAVD nanowires included in Chapters 3-4 have demonstrated that dielectric or freezing properties of adamantane RPAVD thin films remains in the adamantane RPAVD shells of ONWs. Thus, the adamantane RPAVD ONWs keep their chemical and optical properties.

In addition, the procedure enables the fabrication of organic hollow 1D RPAVD nanostructures by vacuum heating post-treatments. Organic core@shell nanostructures such as those of Figure A1.18 were heated until temperatures above 250 °C in vacuum ( $10^{-5}$  mbar). This process leads to the sublimation of the organic inner part of structure fabricated by PVD.

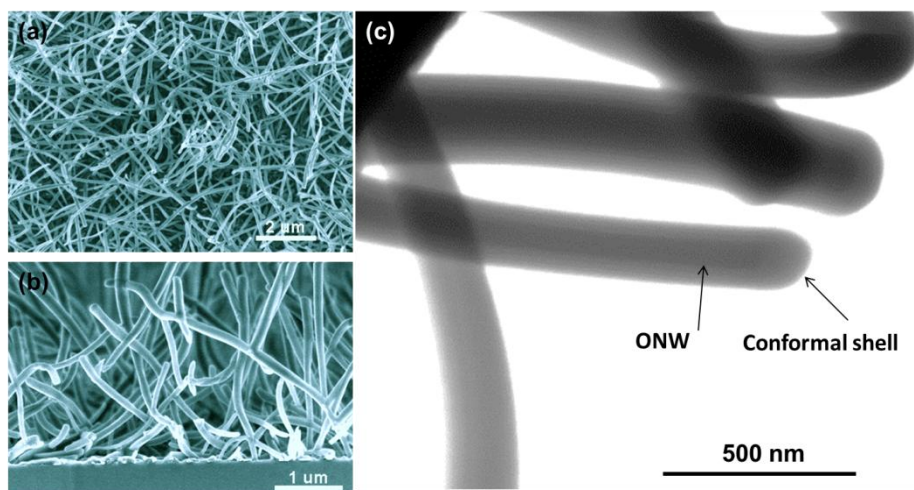


Figure A1.18. 1D nanostructures core@shell - SEM (a,b) and STEM (c) images of organic core@shell fabricated from Me-PTCDI ONWs as core and adamantane RPAVD coatings as shell.



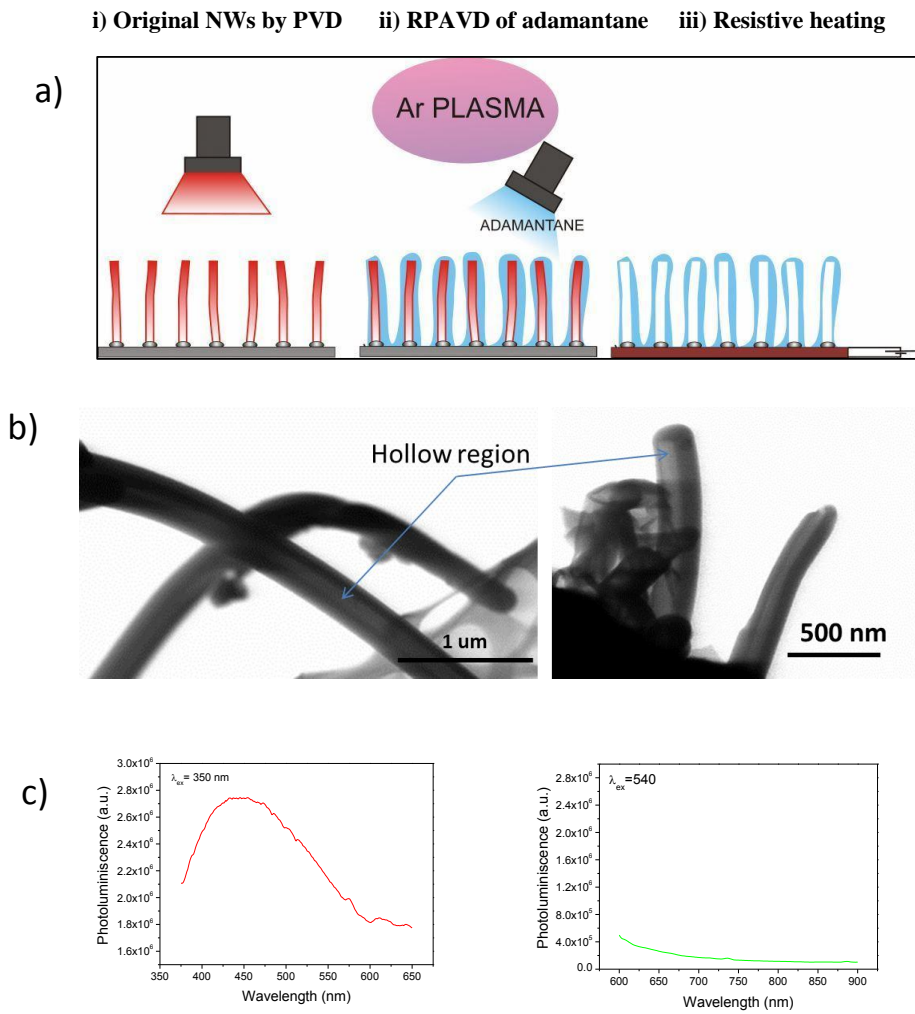


Figure A1.19. Hollow adamantane nanowires – (a) Growth sketch, (b) SEM micrographs and (c) fluorescent emission of hollow adamantane nanostructures.

Figure A1.19 shows a scheme of the fabrication sequence and two magnifications of STEM micrograph of hollow adamantane nanostructure. These structures could be interesting to microfluidics applications actuating as nanocanals. We have tested if the external adamantane composite remains unaffected from photoluminescence measurements. Me-PTCDI shows an intense photoluminescence emission at around 700 nm under excitation wavelengths in the range of 400-580 nm. On the other hand, adamantane shows a slight broad emission at 450 nm under UV excitation. Fluorescence emission at different wavelength excitations was measured in order to check whether the inner Me-PTCDI has been completely removed. Only adamantane composite is keeping after heating treatment, as demonstrated in the Figure A1.19(c). The fluorescence emission of adamantane (less intense than Me-PTCDI emission) is observed at 350 nm of excitation, while the signal is zero when the sample is excited under 540 nm wavelength corresponding to Me-PTCDI excitation.

#### **A1.3.3.2 Nanofabric of adamantane RPAVD**

In Chapter 6, we have developed a general methodology for the synthesis of organic heterostructures by a two steps process: ONWs deposition and soft plasma treatments. This process supplied hierarchical 1D organic heterostructures formed by two or more interconnected ONWs. The present section addresses a new fabrication process being an improvement on that described in Chapter 6. This new method consists of the combination of two methodologies studied throughout the thesis. The first stage consists of the multiple repetition of the aforementioned heterostructures fabrication from the combined process ONWs by PVD – soft plasma treatments (Figure A1.20 i) (a-b)). The resulting nanostructures are named organic nanotrees. The second stage is the after growth of adamantane RPAVD coating on the organic nanotree forming a polymeric network. This structure is called nanofabric (Figure A1.20

ii)). The whole process is developed in the same reactor without breaking vacuum. The wetting and anti-freezing properties of adamantane nanofabric were analysed in Chapter 4 as an application of these nanostructures.

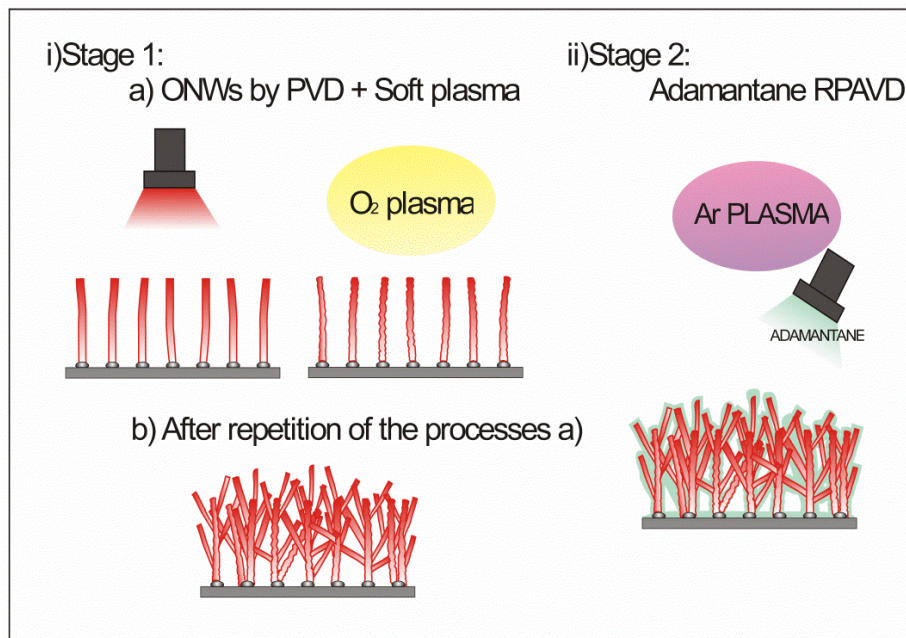


Figure A1.20. Sketch of two grown stages of adamantane nanofabrics – The complete process is produced by two stages. The Stage 1 is divided in several steps. The step 1 corresponds to the growth of organic nanowires (i.e. Me-PTCDI) by PVD, as described in previous Chapters. The step 2 corresponds to oxygen plasma etching producing new nucleation centres for the formation of new nanowires. These two steps have been described in previous Chapters. The next step consists of the repetition of steps 1 and 2 to achieve a nanotree structure formed by the interconnection of the whole nanowires. In the stage 2, adamantane RPAVD composite covers conformally the nanotree structure forming the nanofabric.

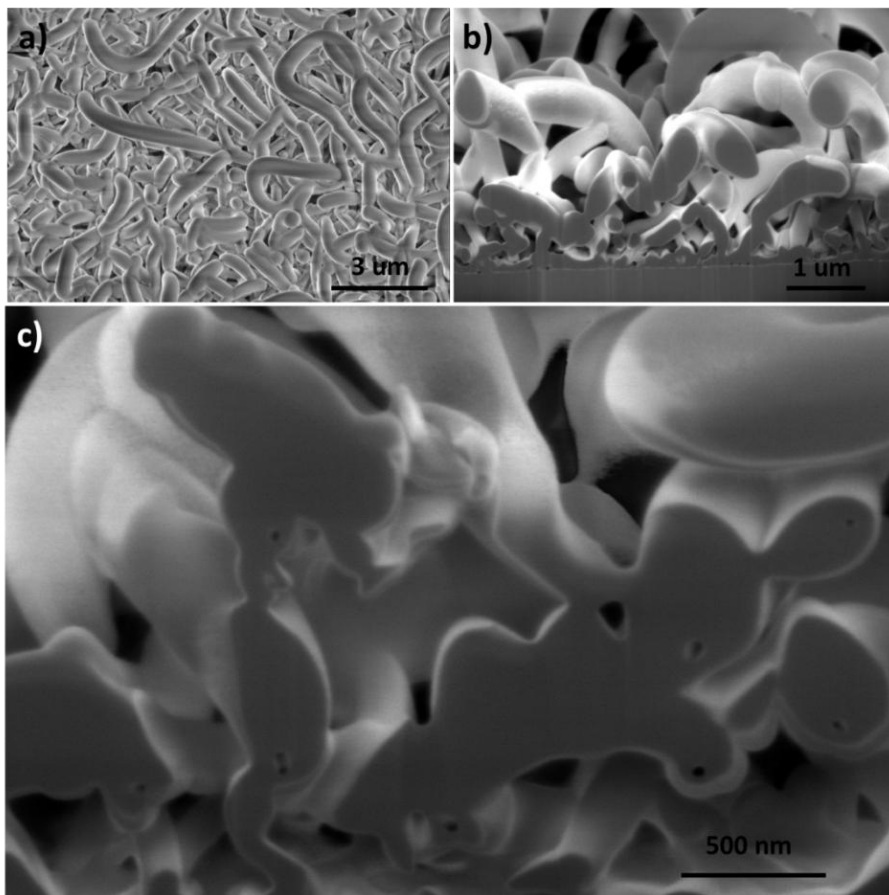


Figure A1.21. Microstructural characterization of adamantane nanofabric using a focused ion beam (FIB) system- Micrographs of adamantane nanofabrics covering an organic core of Me-PTCDI (a,b) and without core (c).

Figure A1.21 shows micrographs obtained by focused ion beam system (FIB). Micrographs (a) and (b) show the surface and a cross section of an adamantane RPAVD nanofabric covering a nanotree structure of Me-PTCDI. The sample was subjected to a heating treatment (above 250 °C in vacuum during 1 hour). The result appears in Figure A1.21(c) where a cross section of this sample shows the holes produced by the Me-PTCDI emptying of the structure.

These structures account for a great importance according to different point of views. First, these structures provide higher surface-volume rates of RPAVD materials. It could be an advantage in gas sensing applications. On the other side, we have achieved for the first time networks like membranes with the general properties of RPAVD materials (thermal stability, insolubility, regular and homogeneous microstructure) and also the particular properties of each material. Therefore, it opens the door to the fabrication of nanostructures with NO<sub>2</sub> sensing properties from perylene RPAVD materials, lasing properties from DCM RPAVD materials, etc. These properties combined with its peculiar microstructure suggest us some applications such as optical membranes, or liquid transport at the nanoscale.

#### **A1.3.3.3 1D nanostructures of other RPAVD materials**

Finally, this idea of expanding the RPAVD thin films properties to the nanostructures has been tested with several RPAVD materials. We have synthesized several examples of this type of heterostructures to highlight the versatility of the method: perylene adamantane RPAVD coatings (photoluminescence and NO<sub>2</sub> sensing properties)<sup>3</sup> on CuPc NWs, 3HF RPAVD coatings (photoluminescence and UV detection properties)<sup>2</sup> on Me-PTCDI NWs, DCM adamantane mixture (photoluminescence and lasing properties) on CoPc NWs. Its feasibility has been confirmed successfully. Thus, the process is general providing the possibility for selecting properties tailored to the needs of the RPAVD material application.

As an example, Figure A1.22 (a) and (b) shows the photoluminescence spectra of 3HF RPAVD coatings on Me-PTCDI NWs grown on TiO<sub>2</sub> columnar film. The spectra in Figure A1.22 (a) correspond to the comparison among the emission spectra at excitation wavelength of 400 nm of 3HF on Me-PTCDI NWs and, 3HF thin films and Me-PTCDI NWs as references.

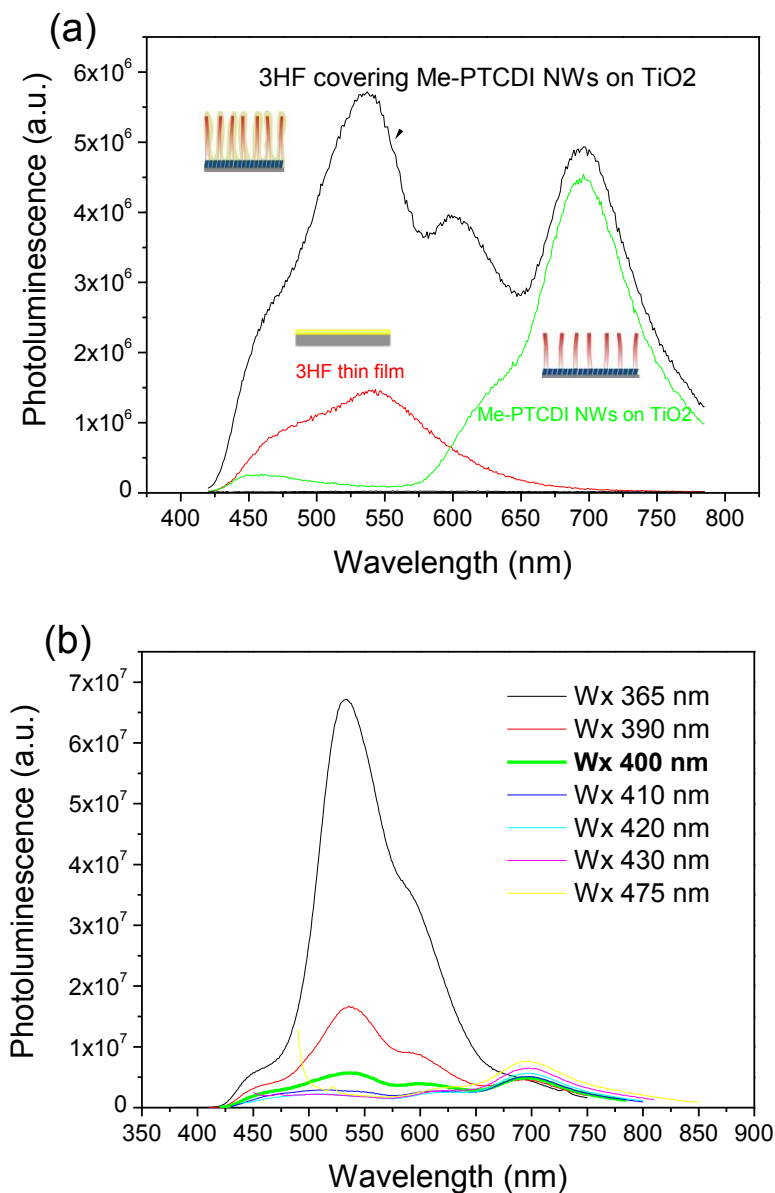


Figure A1.22. Photoluminescent properties of 1D nanostructures organic core@shell from Me-PTCDI and 3HF- (a) Fluorescent emission spectra of the core@shell structure formed by Me-PTCDI NWs and a coating of 3HF RPAVD composite in comparison with 3HF film Me-PTCDI NWs at 400 nm excitation wavelength. (b) Fluorescent emission spectra of the core@shell structure at several excitation wavelengths in the range of 365-475 nm.

We have found that the spectrum of the heterostructure is the combination of the two emissions already described in previous Chapters. The excitation wavelength of a 3HF RPAVD thin film is in the UV and Me-PTCDI NWs is in the range 400-580 nm, as was described in previous Chapters. Figure A1.22 (b) shows the different emissions obtained from the same sample of 3HF RPAVD coatings on Me-PTCDI NWs by tuning the excitation wavelength from 365 nm to 475 nm. The emission of 3HF is more noticeable at UV excitation wavelengths. While under visible wavelengths, Me-PTCDI NWs emission is more evident. The emission offset is at around 400 nm excitation wavelength whose emission (in bold) consists of a broad peak with a width of almost the complete visible spectra.

#### **A1.4 Conclusions**

Adamantane RPAVD thin films have been fabricated under different experimental conditions. The thin films grown at geometries closer and back to the plasma,  $10^{-2}$  Torr and 150 W power source show homogeneity, low grain size, low roughness and transparency. These properties make them suitable candidate to its integration in photonic devices. This geometry protects the substrates of plasma damages. It permits to use sensitive substrates.

Mass spectrometry analysis performed at the conditions of  $10^{-2}$  Torr, 150 W of MW power suggests a minimum of energy.

A new methodology for the synthesis of organic RPAVD structures type core@shell and nanofabric has been developed from the other already known methodologies.

## REFERENCES

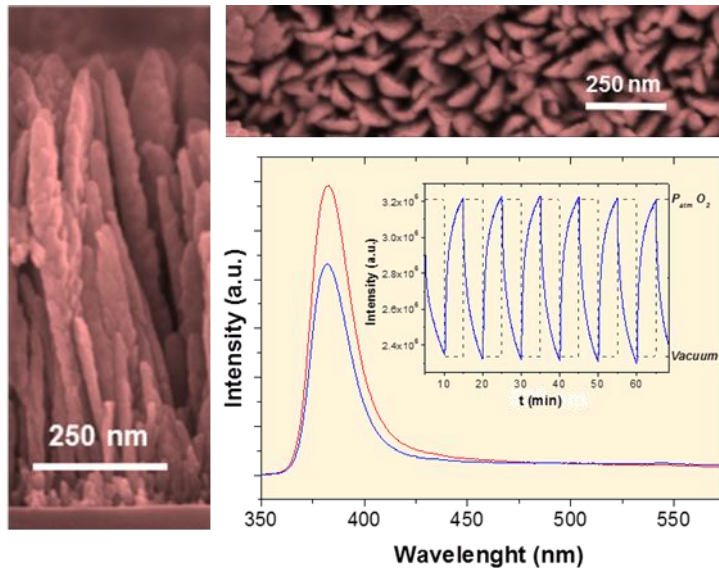
1. Ristein, J.; Stief, R. T.; Ley, L.; Beyer, W., A comparative analysis of a-C : H by infrared spectroscopy and mass selected thermal effusion. *Journal of Applied Physics* **1998**, 84, (7), 3836-3847.
2. Aparicio, F. J.; Alcaire, M.; Borrás, A.; Gonzalez, J. C.; Lopez-Arbeloa, F.; Blaszczyk-Lezak, I.; Gonzalez-Elipé, A. R.; Barranco, A., Luminescent 3-hydroxyflavone nanocomposites with a tuneable refractive index for photonics and UV detection by plasma assisted vacuum deposition. *Journal of Materials Chemistry C* **2014**, 2, (32), 6561-6573.
3. Aparicio, F. J.; Blaszczyk-Lezak, I.; Sanchez-Valencia, J. R.; Alcaire, M.; Gonzalez, J. C.; Serra, C.; Gonzalez-Elipé, A. R.; Barranco, A., Plasma Deposition of Perylene-Adamantane Nanocomposite Thin Films for NO<sub>2</sub> Room-Temperature Optical Sensing. *Journal of Physical Chemistry C* **2012**, 116, (15), 8731-8740.
4. Aparicio, F. J.; Borrás, A.; Blaszczyk-Lezak, I.; Groning, P.; Alvarez-Herrero, A.; Fernandez-Rodriguez, M.; Gonzalez-Elipé, A. R.; Barranco, A., Luminescent and Optical Properties of Nanocomposite Thin Films Deposited by Remote Plasma Polymerization of Rhodamine 6G. *Plasma Processes and Polymers* **2009**, 6, (1), 17-26.
5. Aparicio, F. J.; Holgado, M.; Borrás, A.; Blaszczyk-Lezak, I.; Griol, A.; Barrios, C. A.; Casquel, R.; Sanza, F. J.; Sohlstrom, H.; Antelius, M.; Gonzalez-Elipé, A. R.; Barranco, A., Transparent Nanometric Organic Luminescent Films as UV-Active Components in Photonic Structures. *Advanced Materials* **2011**, 23, (6), 761-765.
6. Blaszczyk-Lezak, I.; Aparicio, F. J.; Borrás, A.; Barranco, A.; Alvarez-Herrero, A.; Fernandez-Rodriguez, M.; Gonzalez-Elipé, A. R., Optically Active Luminescent Perylene Thin Films Deposited by Plasma Polymerization. *Journal of Physical Chemistry C* **2009**, 113, (1), 431-438.
7. Barranco, A.; Biemann, M.; Widmer, R.; Groning, P., Plasma polymerization of rhodamine 6G thin films. *Advanced Engineering Materials* **2005**, 7, (5), 396-400.
8. Barranco, A.; Groning, P., Fluorescent plasma nanocomposite thin films containing nonaggregated rhodamine 6G laser dye molecules. *Langmuir* **2006**, 22, (16), 6719-6722.
9. d'Agostino, R., *Plasma Deposition, Treatment, and Etching of Polymers*. Academic Press Inc.: San Diego (US), 1990.
10. Biederman, H., *Plasma polymer films*. Imperial College Press: London, 2004.
11. Yasuda, H., *Luminous Chemical Vapor Deposition and Interface Engineering*. Marcel Dekker: New York, 2005.



12. Grill, A., *Cold plasma in materials fabrication* IEEE Press ; Institute of Electrical and Electronics Engineers: Birmingham (UK), 1994.
13. Barranco, A.; Aparicio, F.; Yanguas-Gil, A.; Groening, P.; Cotrino, J.; Gonzalez-Eliphe, A. R., Optically active thin films deposited by plasma polymerization of dye molecules. *Chemical Vapor Deposition* **2007**, 13, (6-7), 319-325.
14. Zhizhi, A. H. K. a. G. N., *Handbook of Fourier transform Raman and infrared spectra of polymers*. Elsevier: Amsterdam, 1998.
15. Sokrates, G., *Infrared Characteristic Group Frequencies: Tables and Charts*. Wiley-Interscience: New York (US), 1994.
16. Ferrari, A.; Robertson, J., Interpretation of Raman spectra of disordered and amorphous carbon</title>. *Physical Review B* **2000**, 61, (20), 14095-14107.
17. Ferrari, A.; Robertson, J., Resonant Raman spectroscopy of disordered, amorphous, and diamondlike carbon</title>. *Physical Review B* **2001**, 64, (7), 075414.
18. Aparicio, F. J. L., G.Blaszczyk-Lezak, I.Barranco, A.Miguez, H., Conformal Growth of Organic Luminescent Planar Defects within Artificial Opals. *Chemistry of Materials* **2010**, 22, (2), 379-385.
19. Ostrikov, K., Colloquium: Reactive plasmas as a versatile nanofabrication tool. *Reviews of Modern Physics* **2005**, 77, (2), 489-511.
20. Macias Montero, M. J. New plasma-based synthesis procedures and applications of 1D-nanostructures. University of Seville, Seville, 2013.
21. Borrás, A.; Groning, P.; Sanchez-Valencia, J. R.; Barranco, A.; Espinos, J. P.; Gonzalez-Eliphe, A. R., Air- and Light-Stable Superhydrophobic Colored Surfaces Based on Supported Organic Nanowires. *Langmuir* **2010**, 26, (3), 1487-1492.
22. Macias-Montero, M.; Filippin, A. N.; Saghi, Z.; Aparicio, F. J.; Barranco, A.; Espinos, J. P.; Frutos, F.; Gonzalez-Eliphe, A. R.; Borrás, A., Vertically Aligned Hybrid Core/Shell Semiconductor Nanowires for Photonics Applications. *Advanced Functional Materials* **2013**, 23, (48), 5981-5989.
23. Zang, L.; Che, Y.; Moore, J. S., One-Dimensional Self-Assembly of Planar  $\pi$ -Conjugated Molecules: Adaptable Building Blocks for Organic Nanodevices. *Accounts of Chemical Research* **2008**, 41, (12), 1596-1608.
24. Briseno, A. L.; Mannsfeld, S. C. B.; Jenekhe, S. A.; Bao, Z.; Xia, Y. N., Introducing organic nanowire transistors. *Materials Today* **2008**, 11, (4), 38-47.
25. Liu, H. B.; Li, Y. L.; Zhu, D. B., Synthesis and properties of pi conjugated organic molecular one-dimensional nanomaterials. *International Journal of Nanotechnology* **2007**, 4, (1-2), 197-213.



## A2 Oxygen optical sensing with nanostructured ZnO thin films



### ABSTRACT

Transparent nanocolumnar porous ZnO thin films have been prepared by plasma enhanced chemical vapor deposition. By controlling the H<sub>2</sub>/O<sub>2</sub> ratio in the plasma gas, the deposition conditions were optimized to obtain an intense exciton emission at around 381 nm and virtually no luminescence in the visible region associated to electronic states in the gap. The intensity of the exciton band varied significantly and reversibly with the partial pressure of oxygen in the environment. This behaviour and its variations with temperature and water vapor sustain the use of these thin films as photonic sensors of oxygen. Further experiments in liquid water show that fluorescence intensity also varies with the amount of dissolved oxygen even for concentrations where commercial oxygen galvanic sensors show little or no sensitivity. These results and the use of ZnO as photonic sensor of oxygen are discussed by assuming a classical mechanism involving the photo-activated adsorption of oxygen when this oxide is irradiated with UV light during its fluorescence interrogation.

## A2.1 Introduction

ZnO is a well-known multifunctional material with an extremely wide range of applications in sectors such as solar cells, fabrication of transparent and conducting electrodes, fluorescence devices, piezoelectric devices and many others.<sup>1-8</sup> An interesting property of this oxide is its capability to emit fluorescence radiation at room temperature.<sup>1, 2, 5, 6</sup> The pattern of this fluorescence emission is relatively complex and it is formed by two main bands, one in the near UV region (hereafter called E-band) attributed to the recombination of excitons and some phonon replicas, and another broader one related with a series of several recombination processes involving defect electronic states in the gap (hereafter called D-band, also consisting of the convolution of several contributions).<sup>5-9</sup> Depending on the concentration of defects in the material, the relative intensity of these two bands may vary significantly. In general, an intense E-band and a low or even negligible D-band are obtained with well crystallized forms of this oxide (e.g. single crystals, annealed ceramic samples with large size of the individual crystallites, etc.). By contrast, ZnO in the form of nanostructured films, small nanoparticles, nanofibres or other nanostructures usually present a high concentration of defect states and therefore yields very intense D-bands. This behaviour has been usually attributed to that a high surface to volume ratio and low crystallinity preclude the effective healing of the electronic defects in the gap,<sup>5, 6, 10</sup> a situation that can be reverted to yield very intense E-bands by thermal or plasma post-treatments.<sup>9, 11, 12</sup>

The surface sensitivity of the fluorescence emission of ZnO has been used to develop gas photonic sensors of certain minority gas pollutants by following the changes in the D-band intensity.<sup>13-15</sup> Since a high sensitivity to gases implies a high surface to volume ratio, these fluorescent ZnO sensors are

mostly based on fibres, porous films and similar microstructures. To our knowledge, no similar sensing effects have been reported based on changes in the E-band, generally very small or residual in the utilized forms of nanostructured ZnO. However, correlations have been found between the UV photo-catalytic activity of ZnO, for example for the photo-degradation of dyes, and the relative intensity of this band.<sup>16, 17</sup>

In a previous publication about the synthesis of nanostructured ZnO thin films by plasma enhanced chemical vapour deposition (PECVD) we found that by modulating the plasma deposition conditions it is possible to obtain porous nanocolumnar thin films with a luminescence totally dominated by the E-band and a negligible intensity of the D-band.<sup>18, 19</sup> In the present work we report a thorough analysis of the dependence of the fluorescence properties of these oxide thin films and the concentration of oxygen in gas mixtures or dissolved in water. As a result of these investigations we propose the use of the PECVD ZnO thin films as reliable photonic sensors of oxygen. The work is completed with the analysis of the fluorescence behaviour of the films and how it is affected by water vapour and temperature. Tentative explanations accounting for the observed singular behaviour of ZnO complete this work.

## A2.2 Experimental Setup

ZnO thin films were grown onto surface oxidized Si (100) substrates by PECVD in a plasma reactor with a remote configuration using diethyl zinc ( $\text{ZnEt}_2$ ) as zinc precursor. Further details of the experimental set-up, dosing system and film characterization can be found in a previous publication.<sup>18</sup> The plasma source was operated at a power of 400 W with either  $\text{O}_2/\text{H}_2$  mixtures (in a flow ratio 4/1) (sample A) or pure  $\text{O}_2$  (sample B) at a total pressure of  $4 \times 10^{-3}$  Torr. The substrates and the prepared thin film samples were treated with pure  $\text{O}_2$  plasmas in order to clean the substrates and decompose completely any Zn

precursor molecules adsorbed in the film surface. The synthesis of the films was carried out at a substrate temperature tuned between room 475 K (sample A) and 410 K (sample B). The thickness of the investigated films was around ~750 nm (sample A) and 500 nm (sample B).

The surface and in-depth microstructure of the films have been characterized by Field Emission Secondary Electron Microscopy (FESEM) with a Hitachi S5200 microscope operating at 5.0 keV. The crystal structure of the films has been analyzed by XRD in a Siemens D5000 spectrometer operated in the  $\theta$ - $2\theta$  configuration using the Cu  $K\alpha$  radiation as excitation source. Photoluminescence (PL) measurements were carried out in front face configuration using a Horiba JobinYvon Fluorolog3 fluorimeter equipped with a 450 W Xe lamp and two monochromators in excitation and one in emission. The excitation wavelength was 280 nm. The light emitted by the sample was collected by a PMT detector through the emission monochromator. PL measurements were performed by wavelength scanning the emission spectra between 350 and 800 nm with a 5 nm monochromator step. To monitor the changes in photoluminescence when the films were exposed to gases (oxygen, vacuum, mixtures oxygen and argon, water vapour), the ZnO thin films were tested in a chamber where the different gas mixtures were introduced. In this case, light excitation and fluorescence emission were respectively directed and collected by a Y-shape optical fiber bundle connected to the chamber via a vacuum optical feedthrough. Gas mixtures were prepared by using suitable gas flow-meters. Water addition to the oxygen flow to check the effect of increasing amounts of water partial pressures was done by bubbling oxygen through water at 25 °C (gas pressure in equilibrium 18 Torr) and by diluting with another flow of pure oxygen. The experiments in liquid phase were carried out by bubbling mixtures of O<sub>2</sub>/N<sub>2</sub> through distilled and deionized water in a home-made Teflon chamber with a quartz window. The sample was placed parallel to the windows

inside the chamber. The PL spectra were recorded through the quartz window by using a Y-shape optical fibre. Oxygen concentration in the liquid phase was monitored continuously by using a calibrated galvanic dissolved oxygen sensor electrode (WTW CellOx 325) connected to a WTW InoLab Oxi Level 2 unit.

## A2.3 Results and discussion

### A2.3.1 Fluorescence, structure and microstructure of ZnO thin films prepared by PECVD

The ZnO thin films presented an open columnar nanostructure as shown in Figure A2.1. The relatively high porous character of these films is proved by a refraction index (i.e., 1.88 at 550 nm) value lower than that of bulk ZnO (2.02 at 550 nm), as determined from the interference fringes characterizing the UV-vis transmission spectra of the PECVD films by a Varian Cary 100 spectrophotometer. The nanocolumns forming the basic microstructure of these films were made of ZnO wurtzite nanocrystals with an average crystal size of 38 nm, as calculated by the Sherrer method. A certain preferential texture according to the (002) plane could also be deduced from the comparison of the diffraction diagrams of the films with that of a reference randomly oriented powder.<sup>18, 19</sup>

The fluorescence spectra of the PECVD ZnO thin films depended on the deposition conditions. The relative intensity of the E-band with respect to the D-band varied with process parameters such as plasma gas composition, temperature during deposition and thickness of the films.<sup>18, 19</sup>

Figure A2.2 shows a photoluminescence spectrum characterized by a very high exciton band (E) and practically no contribution of the defect band (D). These spectra corresponded to ZnO films prepared at 200 °C with a mixture of O<sub>2</sub> (80%) and H<sub>2</sub> (20%) as plasma gas (i.e, sample A). The relatively small width of the exciton band and the position of its maximum at 381 nm indicate a

reduced contribution from phonon replicas and that, therefore, the lattice network in these films contains rather few defect sites. In principle, such a behaviour is not common for a polycrystalline materials with a large interface area in contact with the medium and very small crystallites.<sup>5,6</sup>

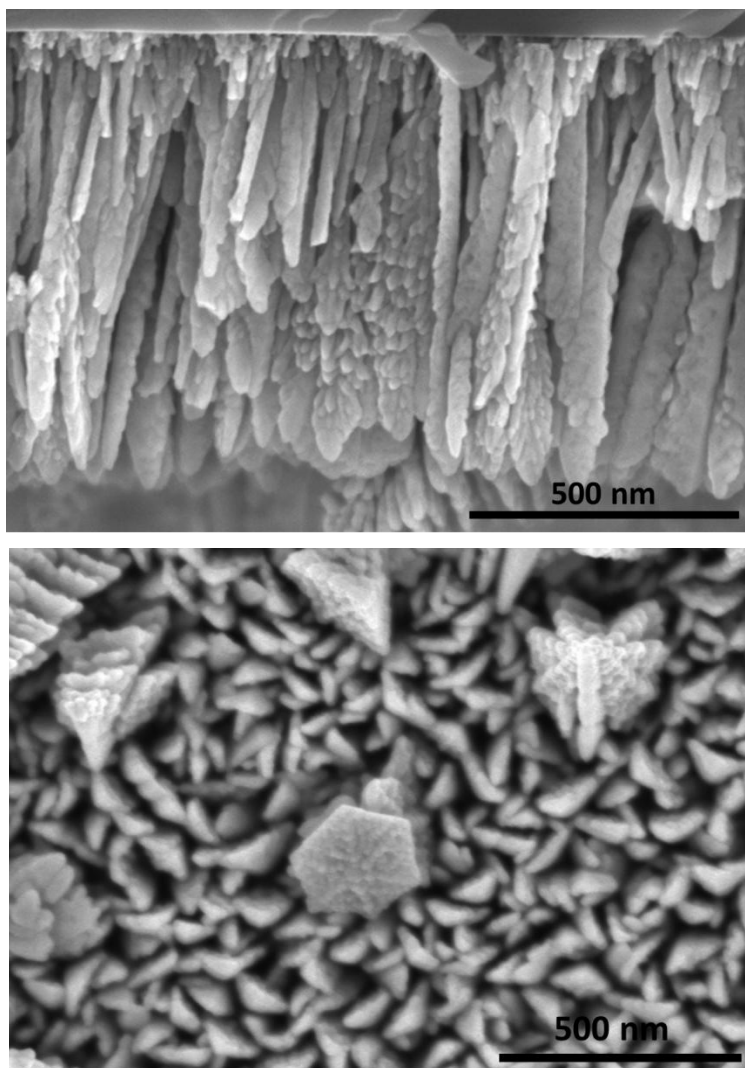


Figure A2.1. Columnar nanostructure of ZnO thin film - Cross section (left) and normal (right) SEM micrographs of a ZnO thin film prepared by PECVD with a mixture of O<sub>2</sub> and H<sub>2</sub> in the plasma gas (sample A).



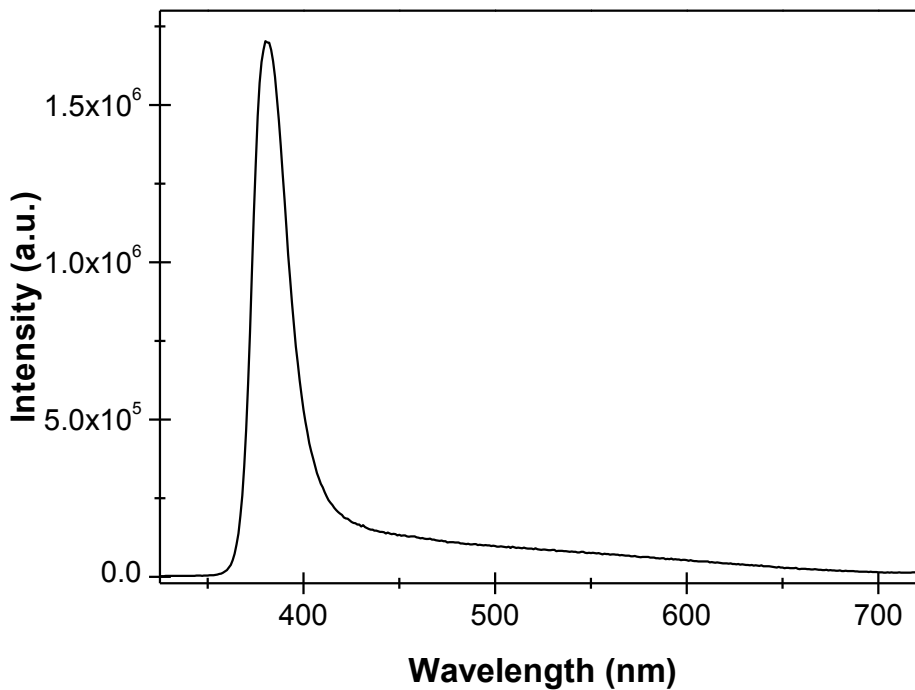


Figure A2.2. Photoluminescence spectrum of ZnO - Fluorescence emission spectrum of a ZnO thin film prepared by PECVD using a mixture of  $O_2$  and  $H_2$  as plasma gas (sample A).

However, recent works have shown that post-annealing treatments of ZnO nanostructures at increasing temperatures drastically affect the relative probabilities of the E- and D-band emissions,<sup>11</sup> while for ZnO nanorods grown by the liquid-vapour-solid method it was found that the E-band to D-band intensity ratio could be modulated by changing the transport gas during their synthesis.<sup>12</sup> Closer to our deposition conditions, Djurisic et al.<sup>9</sup> have shown that hydrogen plasma treatments at room temperature of already grown ZnO nanostructures result in a healing of the band gap defects as evidenced by an increase in the E-band and a decrease in the D-band intensities. Taking these results into account, it is reasonable to assume that during the PECVD synthesis

of ZnO thin films using mixtures of O<sub>2</sub>/H<sub>2</sub> as plasma gas electronic defects in the band gap are being suppressed by interaction with hydrogen species of the plasma.

### A2.3.2 Effect of oxygen on the intensity of exciton emission peak

Investigations were carried out to assess the dependence between the intensity of the exciton peak and the presence of oxygen in contact with the ZnO thin films. Figure A2.3 (a) shows the evolution of the E-band intensity measured in a close environment when sample A was exposed to either vacuum or oxygen at atmospheric pressure. The curve reveals a completely reversible response to the presence of oxygen, the E-band intensity decreasing when this gas was in contact with the film. This behaviour was completely reversible and reproducible and could be monitored after several hundred cycles without any significant modification of the magnitude of the change. The use of an inert gas instead of vacuum produced a similar change in the fluorescence emission (data not shown). In addition, Figure A2.3 (b) shows a comparison of the shape of the fluorescence spectra of sample A under oxygen or in vacuum after stabilizing the signal for 5 minutes as in the previous kinetic experiments. The similar shapes of the normalized spectra in the inset of this figure (i.e. they coincide when superposed) reveals that oxygen/vacuum exposures only produce a change in the intensity of the E band, while at the position of the D-band no modifications were observed. In comparison with previous reports on the use of the D-band intensity to monitor the concentration of pollutants in air,<sup>20, 21</sup> such a behaviour sustains the use of this type of ZnO thin films as a photonic sensor of oxygen by following the intensity of the E-band.

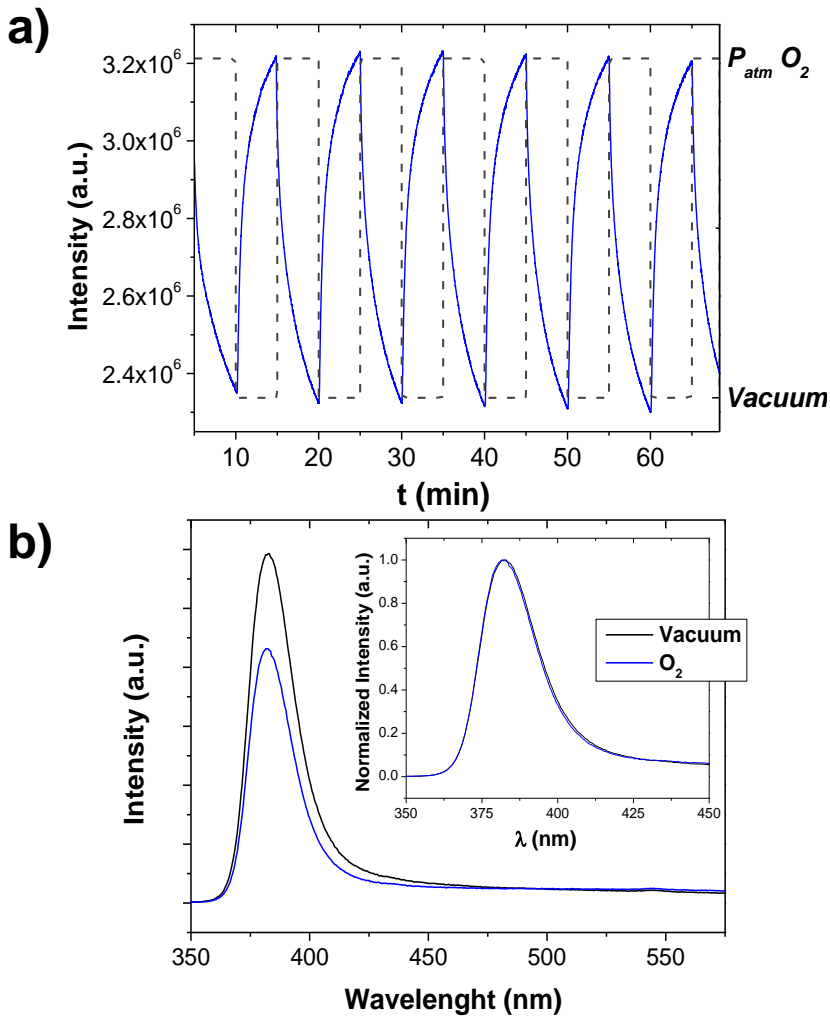


Figure A2.3. Effect of oxygen on the intensity of exciton emission peak - a) Evolution of the exciton photoluminescence intensity of a ZnO thin film (sample A) when it was successively exposed to various cycles of vacuum and oxygen at atmospheric pressure. For the sake of simplicity, the experiment has been stopped before the fluorescence signal has reached the steady state (i.e., after a 70% of the intensity change has been reached). b) Fluorescence emission spectra of the previous sample exposed for 5 min to oxygen and subsequently to vacuum. The normalized fluorescence spectra obtained under these two conditions are included in the inset of this panel.

### A2.3.3 Effect of the oxygen concentration and temperature on the E-band intensity

Since the quantification of the response and the assessment of the influence of other environmental parameters are critical issues for sensors applications, experiments were carried out to ascertain the photoluminescence of the films as a function of the concentration of oxygen at different temperatures. Figure A2.4 (a) shows a plot of the evolution of the E-band intensity in an experiment at atmospheric pressure where the concentration of oxygen was changing in steps by dilution in Ar between zero (i.e., similar behaviour than experiment under vacuum) and 100%. The experiment was conducted at 25 °C and 80 °C. It is apparent in this figure that the E-band intensity is a function of both the concentration of oxygen and the temperature. This dependence is clearly evidenced in Figure A2.4 (b) where, for the two investigated temperatures, the normalized photoluminescence intensity is directly plotted against the concentration of oxygen. This plot clearly shows two regimes. For concentrations of oxygen above 10%, the change in the E-band intensity follows a linear evolution, characterized by a reduction of approximately 15% at 25 °C and 32% at 80 °C. Besides, a sharper decrease is produced for oxygen concentrations between 0 and 10%, showing a higher sensitivity for this range of concentrations. The previous behaviour sustains the use of PECVD ZnO thin films for quantitatively sensing oxygen in gas phase, with a higher sensitivity for low concentrations of this gas.

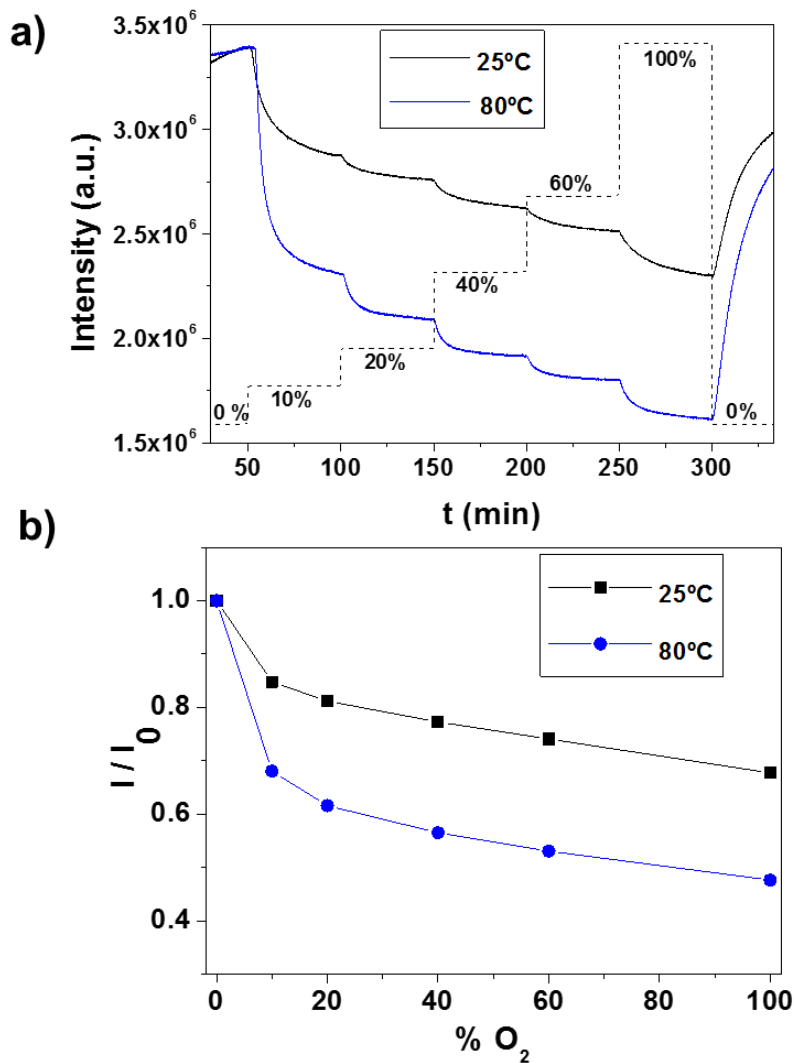


Figure A2.4. Effect of oxygen on the intensity of E-band - (a) Evolution of the intensity of the E-band as a function of time when increasing doses of oxygen are successively introduced in the analysis chamber at the two indicated temperatures. The actual concentration of oxygen in the chamber expressed in percentages is plotted as a dashed line. (b) Plot of the ratio between the actual intensity of the E-band ( $I$ ) after dosing oxygen at different concentrations and the original intensity without oxygen ( $I_0$ ) at the two indicated temperatures.

#### A2.3.4 Effect of humidity on the E-band emission response to oxygen

For a practical use of the ZnO thin films as environmental photonic gas sensor, it is important to determine the effect of water on the photoluminescence response towards oxygen. To check this point, experiments were carried out by dosing increasing amounts of water vapour in the oxygen flow (i.e., at atmospheric pressure) at the two selected working temperatures, 25 °C and 80 °C. Figure A2.5 shows the evolution of the photoluminescence signal for increasing water vapor pressures at these two temperatures. This figure clearly shows that while at 25 °C, particularly for relative humidity higher than 40%, the introduction of increasing amounts of water vapour produces a decrease in the E-band intensity, at 80°C only a very slight increase in the intensity is observed. Quantitatively, this evolution is shown in the bottom plot of the same figure.

The previous results show that the presence of water vapour at 25°C enhances the magnitude of photoluminescence changes when oxygen is incorporated or removed from the medium. An additional evidence of this increase in sensitivity towards oxygen with water vapour at 25°C is reported in Figure A2.6 showing that the fluorescence intensity decreases more when the film is exposed to oxygen saturated with water vapour and that a partial recovery occurs each time that dry oxygen is brought in contact with the film. These changes occur sequentially as many times this cycle is repeated, at least what has been tested for more of one hundred times.

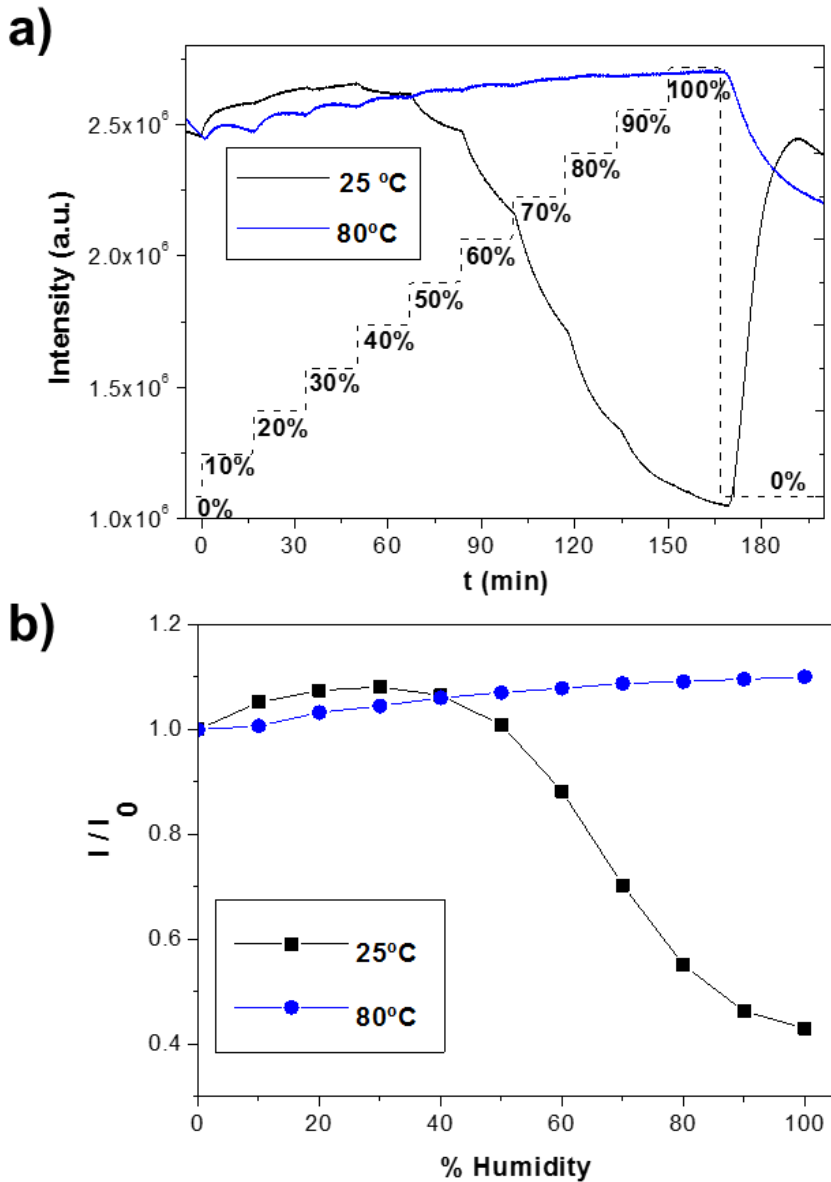


Figure A2.5. Effect of humidity on the intensity of E-band - (a) Evolution of the intensity of the photoluminescence peak at the two indicated temperatures as a function of time while increasing the vapor pressure of water. The relative partial pressure of water in the chamber with respect to the saturation conditions at 25°C is plotted with a dashed line. b) Plot of the ratio between the actual intensity of the E-band (I) after dosing oxygen the original intensity without oxygen ( $I_0$ ) as a function of relative humidity at the two indicated temperatures.

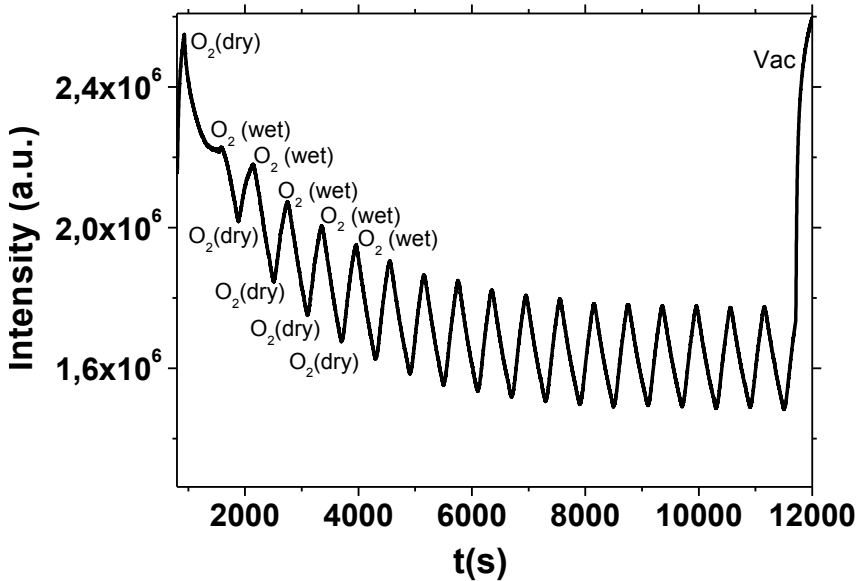


Figure A2.6. Effect of humidity on the intensity of fluorescence emission - Evolution of the intensity of the fluorescence emission of the ZnO thin film upon exposure to one oxygen atmosphere while cycling water vapour in the oxygen flow. Eventually vacuum was made in the experimental chamber.

### A2.3.5 Detection of oxygen dissolved in liquid water

The increase in the sensitivity to oxygen when water vapour is present in the medium suggests that the PECVD ZnO thin films might be used as sensors of oxygen dissolved in liquids. To check this possibility we carried out experiments where nitrogen and mixtures of nitrogen with small but increasing amounts of oxygen were bubbled through water at room temperature while measuring the intensity of the E-band photoluminescence emitted by an immersed ZnO thin film. Simultaneously the amount of dissolved oxygen was monitored with a galvanic sensor electrode.



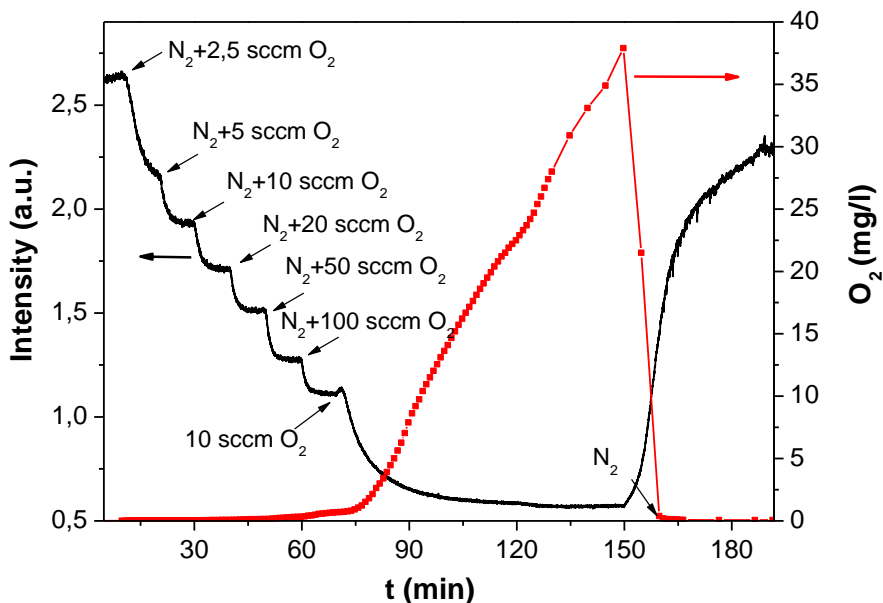


Figure A2.7. Detection of oxygen dissolved in liquid water - Evolution of the photoluminescence intensity from a ZnO thin film immersed in water when a nitrogen flow containing increasing amounts of oxygen was bubbled through the liquid. The right hand axis represents the amount of dissolved oxygen detected with a commercial detector incorporated in the analysis cell.

The experiment reported in Figure A2.7 shows that E-band photoluminescence emission was very sensitive to the presence of small concentrations of oxygen dissolved in water and that even for oxygen concentrations smaller than 1.6 mg/l the photoluminescence decreased by a factor of 2.6 with respect to the water bubbled with pure nitrogen. It is worth noting that for these small amounts of dissolved oxygen the commercial oxygen sensor is almost un-sensitive and only started to provide a clear response when the concentration of oxygen was higher than this value. At the end of the experiment, after bubbling pure nitrogen to remove all oxygen previously dissolved in the liquid, the photoluminescence intensity increased to almost recover its initial intensity. The process could be repeated several times,

although the recovery efficiency was slightly decreasing for successive cycles. It is likely that the unstable character of ZnO in water, particularly at low pHs, can be the reason of this behaviour.

### **A2.3.6 Influence of oxygen on the E- and D-bands fluorescence response of ZnO thin films prepared by PECVD**

A key feature of the PECVD ZnO prepared here is the possibility to control the E-band vs. the D-band relative intensity for a similar microstructure of the films.<sup>18, 19</sup> For the previous experiments with oxygen we have used films (i.e., sample A) where the D-band intensity was practically negligible and the sensitivity towards oxygen was maximized by following the changes in the intensity of the E-band. Possible changes in the D-band were not observed, basically because of its negligible intensity in this type of samples. Trying to get some evidences of possible variations in the intensity of the D-band, we have carried out experiments similar to those reported in Figure A2.3 with a thin film prepared by PECVD by using pure oxygen as plasma gas (i.e., sample B). The photoluminescence spectrum of this film in vacuum depicts an E-band at 382 nm that was less intense and broader than that detected for sample A and a very broad but well defined D band characterized by a moving maximum located between 480 and 520 nm. The effect of exposing this film at 25 °C to oxygen is reported in Figure A2.8. This figure shows the photoluminescence spectra of sample B in vacuum and then subsequently exposed to oxygen at one atmosphere for 50 and 200 seconds and finally exposed and kept in air for a long period of time. Taken into account the time scale utilized with sample A to follow the changes in the E-band intensity in the oxygen exposure experiments (i.e., A2.3.3), the spectra in Figure A2.8 would correspond to two successive points of the decaying curves plotted in Figure A2.4. An important result of this experiment with sample B was that the decrease in the intensity of the E-band is

accompanied by a parallel increase in the intensity of the D-band and a shift to higher wavelengths in the position of its maximum. This opposite change in the intensities of the E and D bands suggests that in parallel to the quenching of the E-band, in this sample oxygen promotes new fluorescence channels involving defect states in the valence band of ZnO. Another striking feature of this oxygen dependent fluorescence emission was its reversibility, a behaviour that entitles the use of this effect for the development of photonic sensors of oxygen and, possibly, other substances. Similar changes in the luminescent emission of the E- and D-bands were found upon exposure of single crystalline or powder ZnO to different gases,<sup>22, 23</sup> although these earlier investigations have not been pursued and no careful oxygen sensor studies have hitherto been reported.

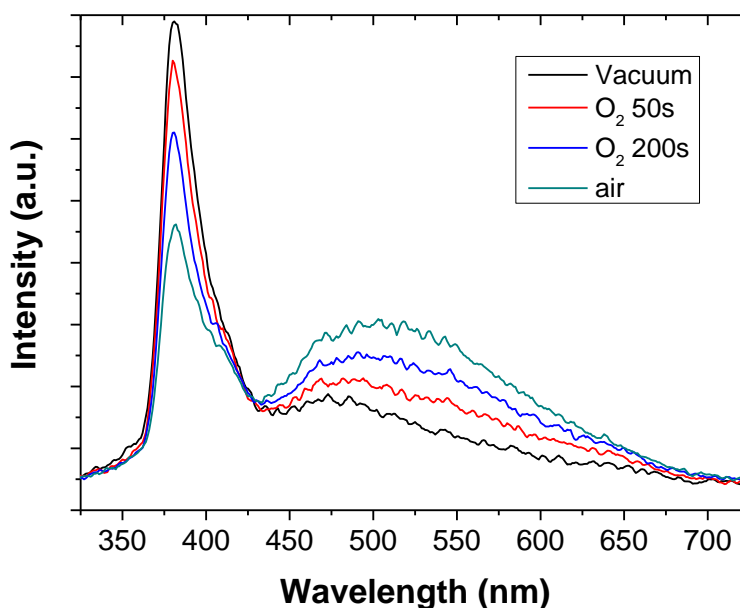


Figure A2.8. Influence of oxygen on the E- and D- bands fluorescence - Photoluminescence spectra of a ZnO thin film (sample B) recorded under vacuum conditions and after being exposed to one atmosphere of O<sub>2</sub> for 50 and 200 s and to air for a long period of time.

### A2.3.7 ZnO as photonic sensor of oxygen

Several reports in the literature dealing with ZnO supported nanowires with a relatively high intensity of the D-band emission showed a reversible decrease in its intensity when the samples were exposed to NO<sub>2</sub>.<sup>20-22, 24</sup> This dependence was accounted for by a surface static quenching process, whereby the gas molecules would suppress a fraction of the radiative transitions rather than merely reduce their probabilities. To our knowledge, since the early works of Idriss and Barteau<sup>23, 25</sup> on the influence of oxygen on the intensity of the D- or E-bands, this effect has not been systematically investigated.

The changes in the E-band intensity upon UV excitation found when the PECVD ZnO thin films were exposed to oxygen can be tentatively attributed to a competition between the emission of exciton photons and surface reactions involving the photo-generated electrons and/or holes with molecules adsorbed on the surface. Correlations between the luminescence of ZnO and its photocatalytic activity have been reported by several authors,<sup>17, 25, 26</sup> showing for example that fast photocatalytic degradation of dye molecules occurs with samples having a low concentration of nonradiative defects characterized by an intense E-band and very small D-band emissions. Similarly, recent works on ZnO used as oxygen and formaldehyde electrical sensors have shown an enhancement in sensitivity when the oxide is simultaneously illuminated with UV light.<sup>27, 28</sup> This effect has been attributed to the formation of photogenerated O<sub>2</sub>- species on its surface.<sup>28</sup> Taking these previous evidences into account we propose a mechanism to account for the interrogation behavior of ZnO as oxygen sensor based in the changes in the intensity of the E-band emission. The mechanism can be described by the following reactions:

- (1)  $(\text{ZnO}) + h\nu \rightarrow e^- + h^+$
- (2)  $e^- + h^+ \rightarrow h\nu' \text{ (E-band)}$
- (3)  $e^- + h^+ + \text{O}_2 \rightarrow \text{O}_x^{n-} \text{ (ads)} + h^+$
- (4)  $\text{O}_x^{n-} \text{ (ads)}/\text{ZnO} \rightarrow \{e^-(\text{trapped})/\text{ZnO}\} + h^+ \rightarrow h\nu'' \text{ (D-band)} + \text{ZnO}$

In this reaction scheme, when an UV photon is absorbed by the ZnO, a valence electron is promoted to the conduction band leaving a hole in the valence band (equation (1)). During the fluorescence analysis of the film, this UV photon is supplied by the excitation source of the spectrometer (i.e.,  $\lambda_{\text{exc}}$  280nm). The recombination of the electron-hole pair (i.e., exciton) produces the emission of a photon with an energy  $h\nu'$  (E-band) (equation (2)). Alternatively, when ZnO and other wide band gap semiconductors are excited by UV light a series of photo-excited surface processes can be induced on its surface by reaction of the photo-generated electrons and holes with adsorbed molecules.<sup>29-32</sup> In the classical literature on TiO<sub>2</sub> and ZnO the detection by FT-IR and electro paramagnetic resonance spectroscopes of a wide set of different surface oxygenated species (e.g., O<sub>2</sub><sup>-</sup>, O<sub>2</sub><sup>=</sup> or, in general, O<sub>x</sub><sup>n-</sup> intermediate species) was already reported as a result of their UV illumination in the presence of oxygen.<sup>33-35</sup> Equation (3) proposes that such processes are also taking place during the fluorescence interrogation experiments in the presence of oxygen (c.f. Figure A2.8). Therefore, the decrease in the E-band intensity when the partial pressure of oxygen increases would be accounted for by a competition between the reactions sketched in equations (2) and (3) the later hampering the emission of excitonic photons (i.e.  $h\nu'$  in (1)), simply because there are less photo-electrons available for recombination.

On the other hand, our results with sample B point to that the photo-generated holes might be removed from the system by reacting with the adsorbed species of oxygen formed in reaction (3) and/or with band-gap trapped

electrons of the system (equation (4)) As a result, a less energetic D photon is emitted at longer wavelengths. The evolution with the exposure time to oxygen of the D- and E-band intensities in Figure A2.8, would be in agreement with the reaction model sketched by equations (1)-(4). The fact that a similar reverse tendency is not clearly observed with sample A should be related with that the E-band intensity is much more intense and the intensity of the D-band almost negligible in this case.

From the classical literature on oxygen photo-adsorption on ZnO and TiO<sub>2</sub> it is also known that the amount of adsorbed species of oxygen and the kinetics of the adsorption process are favoured by hydroxyl groups at the surface that act as photo-hole traps and trigger a series of complex radical reactions involving photo-electrons, oxygen and water, leading to oxygen photo-adsorption.<sup>36-38</sup> Recently Guo et al<sup>39</sup> have proved the importance of the –OH groups adsorbed on the surface of ZnO in enhancing the photo-catalytic activity of this oxide. The series of reactions (1)-(4) are compatible with these classical schemes and suggest that in the presence of a high concentration of surface hydroxyl groups (e.g., at 25°C, Figure A2.5) an increasing amount of photo-holes would be removed by a surface trapping mechanism that can be described by reaction (5):



a process that, by removing a fraction of the photo-generated holes, would decrease the efficiency of reaction (2) responsible for the emission of E-band photons, in agreement with the observed behaviour of the system at 25 °C in the presence of water vapour (c.f., A2.3.6). Besides other possible temperature dependent process, at 80 °C or higher temperatures the expected decrease in the hydroxylation degree of the surface would contribute to limit the efficiency of

reaction (5), so that at this temperature the E-photon emission probability would remain unaffected by the water concentration in the environment.

It is important to stress that the reaction scheme described by equations (1)-(5) would affect in a measurable way to the E-band intensity only if the surface to bulk ratio of the examined ZnO samples is high. This is likely the reason why an oxygen sensing behaviour similar to that of samples A has not been detected previously with single crystals or very compact ZnO materials characterized by a fluorescence emission pattern where the E-band is very intense and that of the D-band negligible.

## A2.4 Conclusions

In this work we have shown that relatively porous and polycrystalline ZnO thin films prepared by PECVD following a precise deposition methodology using  $H_2/O_2$  plasmas present an unexpectedly high intensity of the E-band emission and a fluorescence spectral profile similar to that of single crystalline or compact forms of this oxide. We have also found that the intensity of this E-band emission is highly sensitive to the presence of oxygen in the environment. In another set of experiments, we have shown that the E-band fluorescence emission is also affected by oxygen dissolved in water. The high sensitivity for oxygen detection in this case is superior to that of commercial sensors to monitor oxygen in water. The found changes in the E-band intensity support the use of ZnO to develop photonic sensors of oxygen both in gas and liquid media.

Additional experiments with ZnO thin films depicting both the E-band and D-band fluorescence emissions have shown that there is an interdependence between the two emissions which is controlled by the oxygen present in the medium. To account for the behaviour of the two types of examined samples, we have proposed a model that explains the changes in fluorescence as a function of the relative amount of oxygen in the medium and the influence of water and

temperature. This model relates the spectral intensity changes with a competition between the emission of fluorescence photons and the formation of adsorbed species of oxygen resulting from the surface reactions of photo-electrons and photo-holes with oxygen and hydroxyl groups.



## REFERENCES

1. Chennupati Jagadish, S. P., *Zinc Oxide Bulk, Thin Films and Nanostructures. Processing, Properties, and Applications*. Elsevier: 2006.
2. Hadis Morkoc, U. Ö., *Zinc Oxide: Fundamentals, Materials and Device Technology*. Wiley: 2008.
3. Klingshirn, C. F., Waag, A., Hoffmann, A., Geurts, J., *Zinc Oxide. From Fundamental Properties Towards Novel Applications*. Springer: 2010.
4. Wang, Z. L., Zinc oxide nanostructures: growth, properties and applications. *Journal of Physics-Condensed Matter* **2004**, 16, (25), R829-R858.
5. Djurisić, A. B.; Leung, Y. H., Optical properties of ZnO nanostructures. *Small* **2006**, 2, (8-9), 944-961.
6. Djurić, A. B.; Ng, A. M. C.; Chen, X. Y., ZnO nanostructures for optoelectronics: Material properties and device applications. *Prog Quantum Electron* **2010**, 34, (4), 191-259.
7. Klingshirn, C., ZnO: From basics towards applications. *physica status solidi (b)* **2007**, 244, (9), 3027-3073.
8. Klingshirn, C., ZnO: Material, Physics and Applications. *Chemphyschem* **2007**, 8, (6), 782-803.
9. Leung, Y. H.; Chen, X. Y.; Ng, A. M. C.; Guo, M. Y.; Liu, F. Z.; Djurisić, A. B.; Chan, W. K.; Shi, X. Q.; Van Hove, M. A., Green emission in ZnO nanostructures-Examination of the roles of oxygen and zinc vacancies. *Applied Surface Science* **2013**, 271, 202-209.
10. Heo, Y. W.; Norton, D. P.; Tien, L. C.; Kwon, Y.; Kang, B. S.; Ren, F.; Pearton, S. J.; LaRoche, J. R., ZnO nanowire growth and devices. *Materials Science & Engineering R-Reports* **2004**, 47, (1-2), 1-47.
11. Tam, K. H.; Cheung, C. K.; Leung, Y. H.; Djurisić, A. B.; Ling, C. C.; Beling, C. D.; Fung, S.; Kwok, W. M.; Chan, W. K.; Phillips, D. L.; Ding, L.; Ge, W. K., Defects in ZnO nanorods prepared by a hydrothermal method. *Journal of Physical Chemistry B* **2006**, 110, (42), 20865-20871.
12. Alvi, N.; Farooq, B.; Nur, O.; Willander, M., Influence of different growth environments on the luminescence properties of ZnO nanorods grown by vapor-liquid-solid (VLS) method. *Materials Letters* **2013**, 106, 158-163.
13. Liao, L.; Lu, H. B.; Li, J. C.; He, H.; Wang, D. F.; Fu, D. J.; Liu, C.; Zhang, W. F., Size Dependence of Gas Sensitivity of ZnO Nanorods. *The Journal of Physical Chemistry C* **2007**, 111, (5), 1900-1903.
14. Gao, T.; Wang, T. H., Synthesis and properties of multipod-shaped ZnO nanorods for gas-sensor applications. *Appl. Phys. A* **2005**, 80, (7), 1451-1454.
15. Zhang, Y.; Xu, J.; Xiang, Q.; Li, H.; Pan, Q.; Xu, P., Brush-Like Hierarchical ZnO Nanostructures: Synthesis, Photoluminescence and Gas Sensor Properties. *The Journal of Physical Chemistry C* **2009**, 113, (9), 3430-3435.

16. Guo, M. Y.; Ng, A. M. C.; Liu, F.; Djurišić, A. B.; Chan, W. K., Photocatalytic activity of metal oxides—The role of holes and OH radicals. *Applied Catalysis B: Environmental* **2011**, 107, (1–2), 150-157.
17. Liu, F. Z.; Leung, Y. H.; Djurisić, A. B.; Ng, A. M. C.; Chan, W. K., Native Defects in ZnO: Effect on Dye Adsorption and Photocatalytic Degradation. *Journal of Physical Chemistry C* **2013**, 117, (23), 12218-12228.
18. Romero-Gómez, P.; Toudert, J.; Sánchez-Valencia, J. R.; Borrás, A.; Barranco, A.; Gonzalez-Elipe, A. n. R., Tunable Nanostructure and Photoluminescence of Columnar ZnO Films Grown by Plasma Deposition. *The Journal of Physical Chemistry C* **2010**, 114, (49), 20932-20940.
19. Macias-Montero, M.; Filippin, A. N.; Saghi, Z.; Aparicio, F. J.; Barranco, A.; Espinos, J. P.; Frutos, F.; Gonzalez-Elipe, A. R.; Borrás, A., Vertically Aligned Hybrid Core/Shell Semiconductor Nanowires for Photonics Applications. *Advanced Functional Materials* **2013**, 23, (48), 5981-5989.
20. Ahn, M.-W.; Park, K.-S.; Heo, J.-H.; Park, J.-G.; Kim, D.-W.; Choi, K. J.; Lee, J.-H.; Hong, S.-H., Gas sensing properties of defect-controlled ZnO-nanowire gas sensor. *Applied Physics Letters* **2008**, 93, (26), -.
21. Comini, E.; Baratto, C.; Faglia, G.; Ferroni, M.; Sberveglieri, G., Single crystal ZnO nanowires as optical and conductometric chemical sensor. *Journal of Physics D-Applied Physics* **2007**, 40, (23), 7255-7259.
22. Lettieri, S.; Bismuto, A.; Maddalena, P.; Baratto, C.; Comini, E.; Faglia, G.; Sberveglieri, G.; Zanotti, L., Gas sensitive light emission properties of tin oxide and zinc oxide nanobelts. *Journal of Non-Crystalline Solids* **2006**, 352, (9-20), 1457-1460.
23. Idriss, H.; Andrews, R. M.; Barteau, M. A., Application of luminescence techniques to probe surface-adsorbate interactions on oxide single-crystals. *Journal of Vacuum Science & Technology a-Vacuum Surfaces and Films* **1993**, 11, (1), 209-218.
24. Baratto, C.; Todros, S.; Faglia, G.; Comini, E.; Sberveglieri, G.; Lettieri, S.; Santamaria, L.; Maddalena, P., Luminescence response of ZnO nanowires to gas adsorption. *Sensors and Actuators B: Chemical* **2009**, 140, (2), 461-466.
25. Idriss, H.; Barteau, M. A., Photoluminescence from zinc-oxide powder to probe adsorption and reaction of O<sub>2</sub>, CO, H<sub>2</sub>, HCOOH, and CH<sub>3</sub>OH. *Journal of Physical Chemistry* **1992**, 96, (8), 3382-3388.
26. Jing, L. Q.; Qu, Y. C.; Wang, B. Q.; Li, S. D.; Jiang, B. J.; Yang, L. B.; Fu, W.; Fu, H. G.; Sun, J. Z., Review of photoluminescence performance of nano-sized semiconductor materials and its relationships with photocatalytic activity. *Solar Energy Materials and Solar Cells* **2006**, 90, (12), 1773-1787.
27. Peng, L.; Zhao, Q.; Wang, D.; Zhai, J.; Wang, P.; Pang, S.; Xie, T., Ultraviolet-assisted gas sensing: A potential formaldehyde detection approach at room temperature based on zinc oxide nanorods. *Sensors and Actuators B: Chemical* **2009**, 136, (1), 80-85.

28. Fan, S.-W.; Srivastava, A. K.; Dravid, V. P., UV-activated room-temperature gas sensing mechanism of polycrystalline ZnO. *Applied Physics Letters* **2009**, 95, (14), -.
29. Hosono, E.; Fujihara, S.; Honma, I.; Zhou, H., The Fabrication of an Upright-Standing Zinc Oxide Nanosheet for Use in Dye-Sensitized Solar Cells. *Advanced Materials* **2005**, 17, (17), 2091-2094.
30. Simon, Q.; Barreca, D.; Bekermann, D.; Gasparotto, A.; Maccato, C.; Comini, E.; Gombac, V.; Fornasiero, P.; Lebedev, O. I.; Turner, S.; Devi, A.; Fischer, R. A.; Van Tendeloo, G., Plasma-assisted synthesis of Ag/ZnO nanocomposites: First example of photo-induced H<sub>2</sub> production and sensing. *International Journal of Hydrogen Energy* **2011**, 36, (24), 15527-15537.
31. Rehman, S.; Ullah, R.; Butt, A. M.; Gohar, N. D., Strategies of making TiO<sub>2</sub> and ZnO visible light active. *Journal of Hazardous Materials* **2009**, 170, (2-3), 560-569.
32. Yoshida, H.; Shimizu, T.; Murata, C.; Hattori, T., Highly dispersed zinc oxide species on silica as active sites for photoepoxidation of propene by molecular oxygen. *Journal of Catalysis* **2003**, 220, (1), 226-232.
33. Che, M.; Tench, A. J., Characterization and reactivity of mononuclear oxygen species on oxide surfaces. *Advances in Catalysis* **1982**, 31, 77-133.
34. Che, M.; Tench, A. J., Characterization and reactivity of mononuclear oxygen species on oxide surfaces. *Advances in Catalysis* **1983**, 32, 1-148.
35. Gonzalez-Elipe, A. R.; Soria, J., An electron spin resonance study of charge-carrier stabilization in ZnO. *Journal of the Chemical Society, Faraday Transactions 1: Physical Chemistry in Condensed Phases* **1988**, 84, (11), 3961-3971.
36. Gonzalez-Elipe, A. R.; Munuera, G.; Soria, J., Photo-adsorption and photo-desorption of oxygen on highly hydroxylated TiO<sub>2</sub> surfaces. Part 2.-Study of radical intermediates by electron paramagnetic resonance. *Journal of the Chemical Society, Faraday Transactions 1: Physical Chemistry in Condensed Phases* **1979**, 75, (0), 748-761.
37. Munuera, G.; Gonzalez-Elipe, A. R.; Soria, J.; Sanz, J., Photo-adsorption and photo-desorption of oxygen on highly hydroxylated TiO<sub>2</sub> surfaces. Part 3.-Role of H<sub>2</sub>O<sub>2</sub> in photo-desorption of O<sub>2</sub>. *Journal of the Chemical Society, Faraday Transactions 1: Physical Chemistry in Condensed Phases* **1980**, 76, (0), 1535-1546.
38. Munuera, G. G. E., A.R.; Fernández, A.; Malet, P.; Espinós, J.P. , *Solid State Ion.* **1989**, 32-33, 440.
39. Guo, M. Y.; Ng, A. M. C.; Liu, F.; Djurišić, A. B.; Chan, W. K.; Su, H.; Wong, K. S., Effect of Native Defects on Photocatalytic Properties of ZnO. *The Journal of Physical Chemistry C* **2011**, 115, (22), 11095-11101.